THE GARRETT CORPORATION
AiResearch Manufacturing Division
LOS ANGELES 45, CALIFORNIA

REPORT NO. AP-69-4759

HYPERSONIC RESEARCH ENGINE PROJECT - PHASE IIA
STRUCTURES AND COOLING DEVELOPMENT
EIGHTH INTERIM TECHNICAL DATA REPORT
DATA ITEM NO. 55-7.08
3 NOVEMBER 1968 THROUGH 2 FEBRUARY 1969
NASA CONTRACT NO. NAS1-6666

AP-69-4759 27 February 1969

NO. OF PAGES 148

DATE 27 February 1969

PREPARED BY Engineering Staff

EDITED BY L. F. Jilly

APPROVED BY Henry J. Lopez
Henry J. Lopez
HRE Program Manager

REVISIONS				**ADDITIONS**			
PAGE	**DATE**	**PAGE**	**DATE**	**PAGE**	**DATE**	**PAGE**	**DATE**

FOREWORD

This Interim Technical Data Report is submitted to the NASA Langley Research Center by the AiResearch Manufacturing Company, Los Angeles, California. The document was prepared in accordance with the guidelines established by Paragraph 6.3.3.2 of NASA Statement of Work L-4947-B.

Interim Technical Data Reports are generated on a quarterly basis for major program tasks under the Hypersonic Research Engine Project. Upon completion of a given task effort, a Final Technical Data Report will be submitted.

The document in hand presents a detailed technical discussion of the structures and cooling development for the period of 3 November 1968 through 2 February 1969.

ACKNOWLEDGMENTS

Acknowledgments for completion of this document are herewith extended to the following contributors:

Design and Development: O. A. Buchmann
J. C. Gibson
L. H. King
C. M. Lee
A. I. Stern

Heat Transfer Analyses: A. A. Vuigner
F. M. Walters
C. F. Young

Stress Analyses: W. G. Flieder

CONTENTS

Section		Page
1.	SUMMARY OF STATUS	1-1
	1.1 Structural Assembled Model Design	1-1
	1.2 Full-Scale Component Design	1-1
	1.3 Full-Scale Component Manufacture	1-1
	1.4 Inlet Spike Actuation System	1-1
	1.5 Structural Elements and Models	1-2
2.	PROBLEM STATEMENT	2-1
3.	TOPICAL BACKGROUND	3-1
	3.1 General Design Guidelines	3-1
	3.2 Operational Boundaries	3-3
4.	OVERALL APPROACH	4-1
	4.1 Thermal Design	4-2
	4.2 Structural Design	4-3
	4.3 Mechanical Design	4-4
	4.4 Manufacturing	4-5
5.	ANALYTICAL DESIGN	5-1
	5.1 Aerodynamic Heating	5-1
	5.2 Strut Leading Edges	5-15
	5.3 Leading Edge Thermal Performance	5-18
	5.4 Structural Assembled Model	5-26
6.	DESIGN EFFORT	6-1
7.	MANUFACTURING	7-1
	7.1 Leading Edge Straight Section	7-1
	7.2 Strut Test Section	7-1
	7.3 Innerbody (Inner Shell)	7-4
	7.4 Innerbody (Nozzle)	7-4
	7.5 Inlet Spike	7-5

CONTENTS (Continued)

Section Page

7.6 Leading Edge 7-8

7.7 Outer Shell 7-14

7.8 Cooled-Surface Performance Test Section 7-24

8. TESTING 8-1

8.1 Leading Edge Straight Section 8-1

8.2 Full-Scale Strut 8-6

8.3 Inlet Spike Actuator and Control System (ISACS) 8-37

8.4 Cooled-Surface Performance Test 8-45

8.5 Internal Doubler Panels Creep-Rupture Tests 8-46

9. FUTURE ACTION

9.1 Structural Assembled Model Design 9-1

9.2 Full-Scale Components 9-1

9.3 Inlet Spike Actuation System 9-1

9.4 Model Testing 9-1

REFERENCES R-1

ILLUSTRATIONS

Figure		Page
3.0-1	Cooled Structures Nomenclature	3-2
3.2-1	Typical Engine Operating Cycles	3-5
5.1-1	HRE Aerodynamics Parameters	5-3
5.1-2	HRE Aerodynamic Parameters, Outer Cowl Surface	5-4
5.1-3	HRE Strut Aerodynamic Parameters	5-5
5.1-4	HRE Inlet Spike Thermal Performance	5-7
5.1-5	Spike Folded-Flow Section Thermal Performance	5-8
5.1-6	HRE Innerbody Thermal Performance	5-9
5.1-7	HRE Leading Edge Thermal Performance	5-10
5.1-8	HRE Outer Shell Thermal Performance	5-11
5.1-9	HRE Struts Thermal Performance	5-12
5.1-10	HRE Struts Thermal Performance	5-13
5.2-1	HRE Strut Leading Edge Temperatures	5-16
5.2-2	HRE Strut Leading Edge Fin Geometry	5-17
5.3-1	Nodes for Perpendicular Flow Leading Edge	5-19
5.3-2	Parallel Hydrogen Flow Leading Edge at $M_L = 8$; 88,000-ft Altitude	5-20
5.4-1	SAM Wind Tunnel Aerodynamic Flow Parameters - Spike to Sta. XX = 43.0	5-28
5.4-2	SAM Wind Tunnel Aerodynamic Flow Parameters - Outerbody, Inner Surface, Sta. XX = 37.44 to 43.00	5-29
5.4-3	SAM Wind Tunnel Aerodynamic Flow Parameters - Innerbody and Outerbody from Sta 43.0	5-30
5.4-4	SAM Wind Tunnel Aerodynamic Flow Parameters - Outerbody, Outer Surface	5-31
5.4-5	HRE Predicted Heat Flux Distribution for SAM Wind Tunnel Design Point	5-32

ILLUSTRATIONS (Continued)

Figure		Page
5.4-6	Enthalpy of Methane-Vitiated Gas (ϕ = 0.080)	5-33
5.4-7	Absolute Viscosity of Methane-Vitiated Gas (ϕ = 0.080)	5-34
5.4-8	Prandtl Number of Methane-Vitiated Gas (ϕ = 0.080)	5-35
7.2-1	Strut Leading Edge Fin Evaluation - X-Rays of Braze Joint (Dark Area) Between Fin and CRES 304 Tubing	7-2
7.2-2	Strut Leading Edge Fin Evaluation - Metallographic Examination Showing Filleting of Braze Alloy at Fin-to-Skin Joint	7-3
7.4-1	SN 5 Nozzle After StressCoat and 1050 psig Proof Pressure Test	7-6
7.5-1	Aft Spike Shell Assembly After 2200 psig StressCoat Pressure Test	7-7
7.6-1	Inner Shell Assembly	7-9
7.6-2	Outer Shell Assembly	7-11
7.6-3	Tip Assembly	7-12
7.6-4	Inlet Manifold Assembled for Brazing	7-13
7.7-1	Manifold - Typical Cross Section	7-15
7.7-2	Outer Shell Aft Support Manifold Final Assembly Ready for Installation on Structure	7-16
7.7-3	Outer Shell Forward Support Manifold Assembly Ready for Final Machining	7-17
7.7-4	Outer Shell Second Fuel Injector Manifold Final Assembly Prior to Fit-Up Machining	7-18
7.7-5	Outer Shell First Stage Fuel Injector Duct	7-19
7.7-6	Outer Shell Third Stage Fuel Injector Ducts	7-21
7.7-7	Outer Shell Forward Distribution Manifold - Tube Connection Ring	7-22

ILLUSTRATIONS (Continued)

Figure		Page
7.7-8	Outer Shell Aft Coolant Inlet Manifold	7-23
7.7-9	Outer Shell Skin/Fin Assembly Ready for Final Manifold Attachment	7-25
7.8-1	Heat Exchanger Fin Cores, Air Side	7-26
7.8-2	Heat Exchanger Fin Cores, Water Side - 20 Fins Per in., 0.075 in. High, 0.004 in. Thick	7-27
7.8-3	Cooled-Surface Performance Test Unit	7-28
8.1-1	Leading Edge Straight Section Radiant Heating Test Fixture Schematic	8-2
8.1-2	Schematic Water and Air Coolant Systems for Leading Edge Straight Section	8-3
8.1-3	Leading Edge Straight Section Test Setup with Lamp and Fixture	8-4
8.1-4	Leading Edge Straight Section in Radiant Heating Test Setup	8-5
8.2-1	Strut Flow Test Setup Schematic	8-7
8.2-2	Strut SN 6 Before Run 30	8-8
8.2-3	Combustor and Test Section Total Temperature	8-11
8.2-4	Strut SN 6 Metal-Strip Melting Results	8-13
8.2-5	K-Factor Effects on Heat Transfer Rates	8-15
8.2-6	Ratio of Measured-to-Calculated Average Heat Flux for Strut Leading Edge	8-17
8.2-7	Enthalpy of Ortho-, Normal-, and Equilibrium-Hydrogen Relative to Para-Hydrogen	8-18
8.2-8	Thermal Entry Effect for Para-Hydrogen at 110^0R (Approximately)	8-19
8.2-9	Heat Flux Distribution	8-21
8.2-10	Average Heat Flux vs K-Factor	8-23

ILLUSTRATIONS (Continued)

Figure		Page
8.2-11	Strut SN 6 Leading Edge Temperatures for Cycles 3 and 9	8-24
8.2-12	Strut SN 6, Cycle 3 Strut Temperatures	8-25
8.2-13	Strut SN 6, Cycle 3 Panel Hydrogen Temperatures	8-26
8.2-14	Strut SN 6, Cycle 3 Panel Wall and Socket Temperatures	8-27
8.2-15	Strut SN 6, Cycle 9 Strut Temperatures	8-28
8.2-16	Strut SN 6, Cycles 8 Through 11 Hydrogen Temperatures	8-29
8.2-17	Strut SN 6, Cycles 8 Through 11 Panel Wall Temperatures	8-30
8.2-18	Strut SN 6, Cycles 8 Through 11 Panel Wall and Strut Socket Temperatures	8-31
8.2-19	Strut SN 6 Leading Edge After Cycle 11	8-32
8.2-20	Strut Leading Edge Temperatures During Thermal Cycling	8-33
8.2-21	Strut Support Panels (-4) After Cycle 11	8-35
8.2-22	Strut Support Panel Failure	8-36
8.3-1	Load Profiles for PN 981190-1-1	8-38
8.3-2	Load Profiles for PN 981190-1-1	8-39
8.3-3	ISACS Positioning Accuracy	8-41
8.3-4	ISACS Displacement Variation	8-42
8.3-5	ISACS Positioning Rate vs Supply Pressure	8-43
8.4-1	Schematic of Laboratory Test Setup for Cooled-Surface Performance Test Unit	8-47
8.4-2	Cooled-Surface Performance Test Setup	8-48
8.4-3	Cooled-Surface Performance Test Setup	8-49

TABLES

Table		Page
5.3-1	Perpendicular Flow Leading Edge Temperatures with Spike Closed at M_L = 8, 88,000-ft Altitude	5-21
5.3-2	Perpendicular Flow Leading Edge Temperatures with Spike Open and No Spike Shock Impingement at M_L = 8, 88,000-ft Altitude	5-22
5.3-3	Perpendicular Flow Leading Edge Temperatures with Spike Open and Spike Shock Impingement at M_L = 8, 88,000-ft Altitude	5-23
8.2-1	Nominal Strut SN 6 Test Conditions	8-9
8.2-2	HRE Strut Test	8-10
8.2-3	Strut Flange and Socket Heating from Slot-Flow	8-16
8.3-1	Actuator Loads	8-44

NOMENCLATURE

D	diameter, ft
F_t	h/h_∞ is to account for thermal entrance effects, dimensionless
h	heat transfer coefficient, Btu/sec-ft^2-^{0}R
K	h_{ST}/h_{FR} to account for stagnation zone freestream turbulence effect, dimensionless
k	thermal conductivity
l	length, ft
Nu	Nusselt number, h D/k
Pr	Prandtl, $\frac{C_p\mu}{k}$
q/a	heat flux, Btu/sec-ft^2
Re	Reynolds number, $\frac{Dv\rho}{\mu}$
r	radius, ft
s	distance along leading edge from the stagnation line, ft
T	temperature, ^{0}R

Subscripts

b	bulk properties
FR	Fay-Riddell
ST	stagnation
th	theoretical
W	wall temperature or fluid properties at wall temperature
∞	fully-developed thermal boundary layer
1	outside leading edge
2	inside leading edge

1.0 SUMMARY OF STATUS

The major effort continues to be concentrated on fabrication of the full-scale cooled structures components (inlet spike, inner shell, nozzle, leading edge, and outer shell). Preparation of assembly drawings for the structural assembled model has been started. Tests of structural elements or models including the leading edge straight section, the full-scale strut, and cooled-surface performance test sections, have been run.

1.1 STRUCTURAL ASSEMBLED MODEL DESIGN

The structural assembled model (SAM) consists of all of the full-scale components and the actuator but does not include the control, fuel, and instrumentation subsystems. A water-cooled cowl and pylon will be used in the wind tunnel evaluation. Design activity during the reporting period has included work on assembly drawings of the spike, the inner shell/strut/outer shell, and layout design of the water-cooled cowl and pylon. Evaluation of performance of the hydrogen cooled structures at the wind tunnel operating conditions has been started.

1.2 FULL-SCALE COMPONENT DESIGN

As previously indicated, all major design efforts have been completed. During the reporting period, minor revisions to various components were made to reflect the requirements of the SAM assembly drawings.

1.3 FULL-SCALE COMPONENT MANUFACTURE

Manufacture of parts for all of the full-scale components is continuing. All basic shell assemblies have now been brazed with the exception of the outer shell trailing edge shells and the leading edge tip assemblies. All of these shells have been satisfactorily proof-pressure tested with the exception of one aft spike shell assembly. Repair operations to correct braze voids in a header of this shell are in process. A second completed inner shell assembly and a second completed nozzle assembly are in process of final machining.

1.4 INLET SPIKE ACTUATION SYSTEM

Teardown of the first prototype actuation system revealed damage to one of the two fabroid journal bearings, and galling of the bearing ring and housing. The bearings of this system are being replaced, and the housing remachined and replated prior to reassembly of the actuator. Teardown of the second prototype system showed no damage to the bearings. The first system had been exposed to approximately 150 load cycles of various kinds; the second system to approximately 80 load cycles. The cause of the bearing damage is ascribed to too coarse a surface finish on the mating structural housing. Following rework, the first prototype system will be installed in the test system for endurance testing. The second prototype system will be reassembled, after which testing will be completed. Remaining tests on this system involve only the running of frequency response tests.

1.5 STRUCTURAL ELEMENTS AND MODELS

1.5.1 Leading Edge Straight Section

Fabrication of all leading edge straight sections has been completed. Fabrication of a test setup for thermal cycling of the leading edge straight sections has also beem completed. This test setup uses a single quartz lamp focused to provide heat input to the stagnation area. Water was originally planned as the coolant for the Configuration No. 1 units and air for the Configuration No. 2 units. Calibration and evaluation of the test setup has indicated a lower than specified heat flux from the lamp, and consequently, lower than desired temperatures and temperature differences in the stagnation area of the Configuration No. 1 units. As a result, air will be used to test the Configuration No. 1 units also.

1.5.2 Full-Scale Strut

Wind tunnel testing of a second strut was performed. Testing involved further calibration for leading edge heating,and various types of edge-heating associated with the wind tunnel conditions. Following the performance tests, a series of 11 thermal cycles was run on the strut. At the conclusion of these cycles the strut was still sound,but leakage had occurred in one of the strut support panels. An additional entry is planned for this strut using a new set of support panels which incorporate the flow distribution design features used in the full-scale components.

1.5.3 Cooled-Surface Performance Test Section

Fabrication of test units and the test setup for performance of heat transfer and pressure drop tests of regeneratively cooled surfaces have been completed. Testing of the first unit (28 fins per in.) is currently in process. Preliminary evaluation of isothermal pressure drop data for this fin indicates that the measured performance closely matches the estimated performance used in design analyses.

2.0 PROBLEM STATEMENT

The objective of the structures and cooling development program is to analyze, design, and fabricate the regeneratively cooled surfaces and their associated structures and to verify the performance of these surfaces and structures at conditions that simulate the operating conditions expected in the flight test engine.

The Hypersonic Research Engine requires regenerative cooling on all surfaces that contact the engine airstream. The use of ablative coating on the engine aerodynamic surfaces is barred by the Statement of Work to minimize extraneous effects on engine performance. No such restriction is imposed on the engine cowl; therefore, ablative protection is used for this component.

The characteristic design problem in regeneratively cooled structures for this type of application is associated with the large heat fluxes encountered over major portions of the engine surfaces. These heat fluxes range from values of approximately 10 Btu/sec-ft^2 to 1800 Btu/sec-ft^2 on the stagnation line of the support strut leading edge. The conservation of fuel requires that these heat fluxes be accommodated at temperature differences across the regeneratively cooled surfaces which range up to approximately 800^{0}F in flat surfaces and 1200^{0}F in leading-edge areas. These temperature differences, in turn, result in strains that cause plastic deformation of the hot surfaces. Design therefore is governed by low-cycle fatigue conditions. Uncertainties associated with the prediction of low-cycle fatigue performance have led to heavy emphasis, in the experimental portion of the program, on the evaluation of the low-cycle fatigue performance of the engine components.

The general performance objectives set for the cooled structures are as follows:

Design life - 10 hr of hot operation, of which 3 hr are to be taken at Mach 7 to 8 flight conditions

Cycle life - 100 cycles, at conditions which produce the highest plastic strain

3.0 TOPICAL BACKGROUND

The cooled structures, which are being designed, fabricated, and tested as part of this task, and the associated connecting structures constitute the basic structural elements of the engine. The cooled surfaces of these structures form the aerodynamic surfaces of the engine, as shown in Figure 3.0-1.

3.1 GENERAL DESIGN GUIDELINES

The regeneratively cooled surfaces must be designed and fabricated to minimize engine performance losses. In addition to providing the basic contours, the cooled surfaces must be fabricated and assembled in a way that avoids discontinuities; leading edges must use the minimum radius compatible with reliable structural design.

Because of the research nature of the HRE program, temperatures and pressures will be measured throughout the engine. Consequently, the engine structures must accommodate static pressure taps and metal temperature thermocouples.

The total amount of fuel available to the engine and for cooling of the structure is severely limited by X-15A-2 storage capabilities. Consequently, in cooling the structure, fuel usage in excess of combustion requirements must be minimized. To accomplish this goal, the cooled surfaces must function at maximum metal temperatures and temperature differences compatible with sound structural design.

Engine internal structures and plumbing must be designed to allow space for installing fuel system components, engine controls, instrumentation transducers, and signal conditioning equipment. Because of operating limitations, electronic equipment must be installed in locations having the least severe environment.

To permit the engine to operate over the flight Mach number range from 3 to 8, the inlet spike must be translated to various positions. To conserve coolant prior to and after engine operation, the inlet spike must be translated to a position nearly in contact with the outerbody leading edge. Consequently, it is necessary to have a spike actuation system capable of the desired positioning accuracy, with control provided by the control system computer.

Engine fuel pressurization is provided by a hydrogen turbopump. Therefore, the total pressure drop in the regeneratively cooled surfaces, manifolds, and associated plumbing must be compatible with the pressure output of the turbopump.

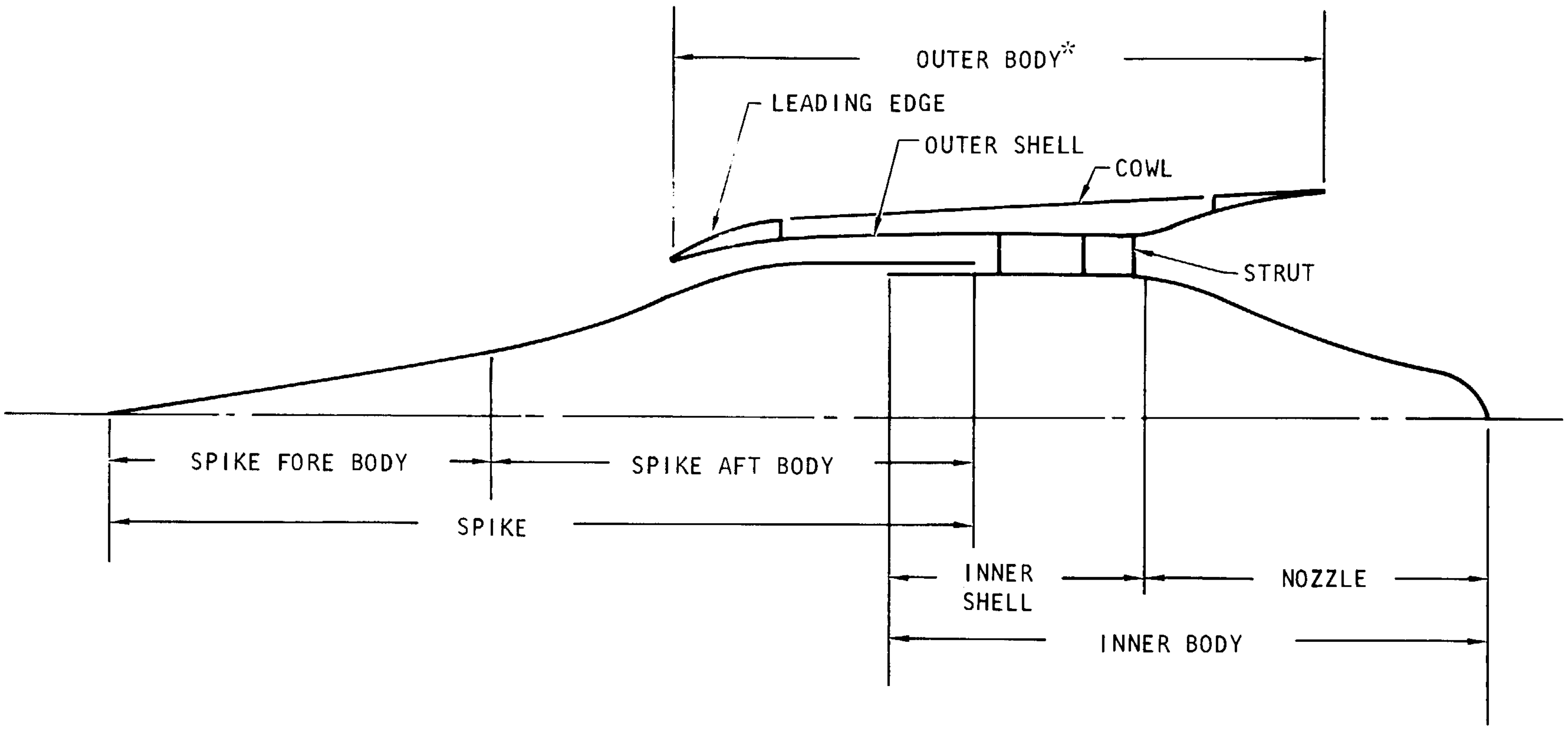
OUTER BODY*
LEADING EDGE
OUTER SHELL
COWL
STRUT
SPIKE FORE BODY
SPIKE AFT BODY
SPIKE
INNER SHELL
NOZZLE
INNER BODY

*OUTER BODY = LEADING EDGE + OUTER SHELL

A-30504

Figure 3.0-1. Cooled Structures Nomenclature

In addition to control of temperatures and temperature differences, the integrity of the coolant structures requires that the flow routes within the engine be matched in such a way as to minimize temperature differences at axial stations for innerbody and outerbody surfaces. This will minimize distortion of the engine internal passages. Axial temperature discontinuities as produced, for example, by the termination of two flow routes that differ greatly in temperature at the same station, are objectionable because of the severe thermal strains that result.

Measurement of engine internal thrust during flight is required. Consequently, external loads (drag and lift) that are transmitted directly to the thrust measuring device must be minimized. Specifically, the engine cowl has drag loads that are of the same order of magnitude as the engine thrust. Mounting of the cowl in such as way as to minimize this external drag load, and thus the uncertainties in calculation of thrust, is therefore required.

A basic engine design requirement is that malfunction of the engine will not endanger the safety of the aircraft or the life of the pilot. Therefore, provision must be made to jettison the engine. Because of probable hydrogen leakage to the engine cavities, the innerbody engine cavity must either be inerted or must be capable of containing an explosive mixture of hot hydrogen and air. To accomplish this, the engine cavity will be vented to near nozzle base pressure and provisions will be made for explosion containment. During ground checkout, the engine cavity will be inerted with nitrogen.

The weight of cooled structures, inlet spike actuation system, internal supporting structures, and plumbing is most of the total engine weight. Although optimization of the structures and structural components for minimum weight is not an objective, the specified weight limitation requires careful consideration of structural weight.

The instrumentation, controls, and fuel subsystems contained in the engine cavity will require servicing prior to and after each test. Consequently, the mechanical assembly of the engine cooled structure components must provide easy access to subsystem components for replacement in the field.

3.2 OPERATIONAL BOUNDARIES

3.2.1 General Design Ground Rules

The maximum dynamic pressure specified for the current phase of the program is 2000 psfa. This compares with the specified dynamic pressure of 2500 psfa, specified for the HRE Phase I program. Consequently, the minimum altitude at Mach 8, during which cooling must be provided, is 85,000 ft, as compared to the Phase I minimum altitude of 81,000 ft. The minimum design altitude for the current program is 88,000 ft. The increased altitude results in a reduction of heat flux throughout the engine, but this reduction is offset in part by an increase in engine contraction ratio from 10 in Phase I to 14.6 in Phase IIA. In summary, the operating envelope for the engine is as follows:

Engine Structural Design - With engine either lit or not lit, dynamic pressure (q) = 2000 psfa

Engine Cooling Design

Normal design, engine lit: q = 1750 psfa, h = 88,000 ft minimum

Emergency design, engine lit: q = 2000 psfa, h = 85,000 ft minimum

For the emergency design, engine lit conditions, all of the pump output pressure is available for coolant pressure drop. The dump valve opens and fuel injection valves close as the aircraft approaches these conditions from the normal operating line.

3.2.2 Engine Operating Cycles

A qualitative definition of the engine operating cycles has been formed for the purpose of providing a basis for analyzing heat transfer transients, evaluating the structural effect of transient temperature differences, establishing general control requirements and typical environmental conditions, and for defining acceptable operating cycles. The types of missions or conditions the engine must survive are as follows:

Case I - Constant M, with aircraft power on, at a constant high q

Case II - Constant M, with aircraft power off, aircraft diving

Case III - Variable M, expected to involve a change in M of 0.5 during 20-sec engine operating cycle

Case IV - Subsonic-supersonic combustion transition at M = 6

Case V - Inlet unstart, with shock expelled

Figure 3.2-1 is a qualitative representation of the critical cases. The common features, typical for all missions, are numbered on the figure and are as follows:

1. Launch to $M = 3+$, during which the engine structure is assumed to go from a soak at -65^0F to a soak at 1140^0F. No cooling is required. At the end of this period, the helium purge is performed and coolant flow started through all portions of the cooled structure.

2. Approach to test Mach number, inlet closed (leakage flow only), during which coolant flow is increased to maintain maximum structure temperature (cold surface) at 1140^0F.

3. Time for retraction of inlet spike to desired position. The solid lines assume programmed cooling flow; the dashed line assumes controlled cooling flow based on temperature sensing. The approach selected will be a function of control system response and actuating system response. Controlled cooling is preferred.

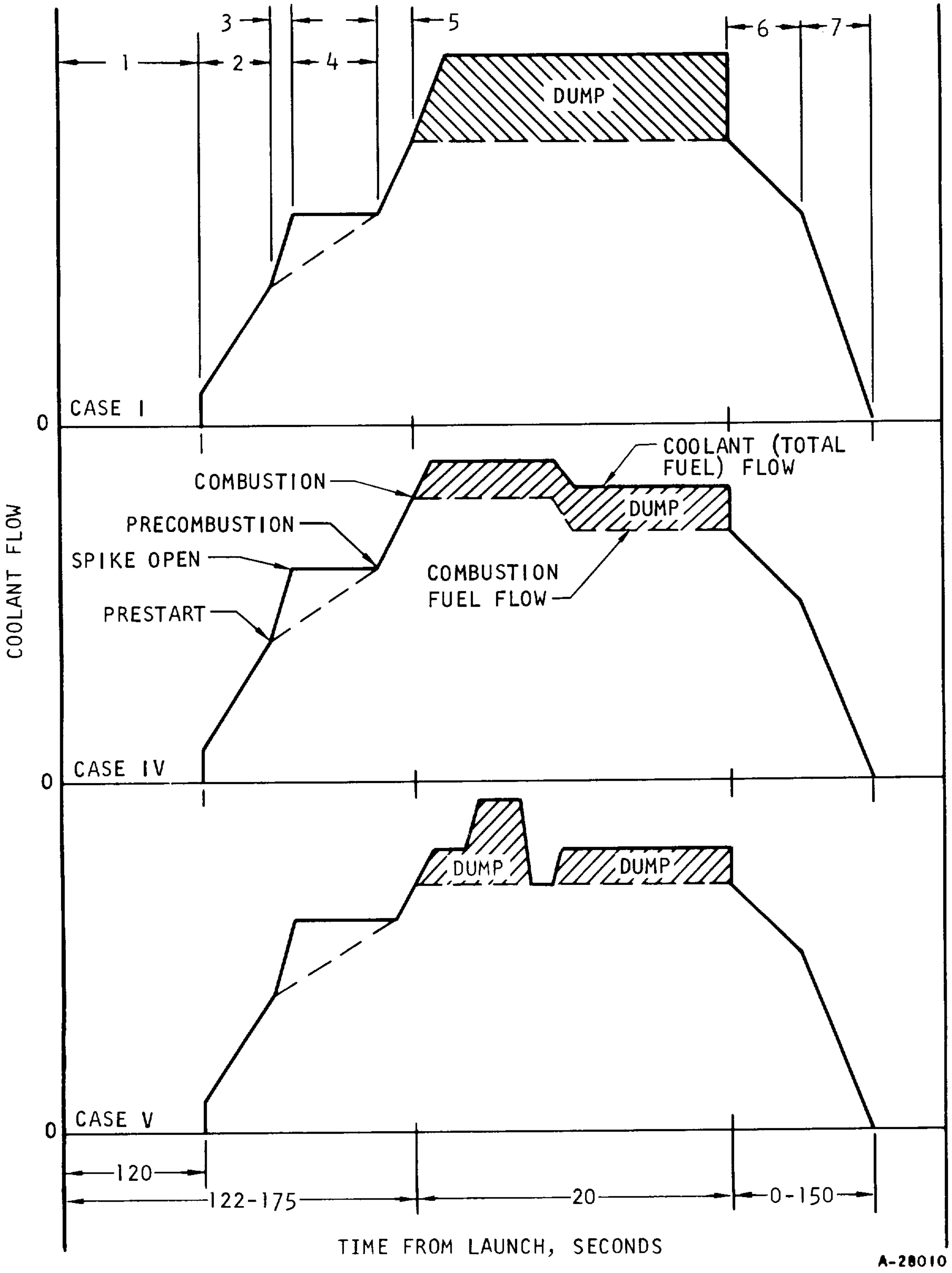

Figure 3.2-1. **Typical Engine Operating Cycles**

4. Inlet spike in starting position, full airflow through the engine, no combustion.

5. Programmed increase in cooling flow to starting combustion equivalence ratio (ϕ). This ϕ will be less than the test ϕ. Combustion ϕ will ramp to test ϕ (not shown).

6. Combustion terminated and inlet spike being extended to closed position.

7. Inlet closed (leakage flow only), deceleration to $M = 4 +$, with coolant flow decreased to maintain maximum structure temperature at 1140°F. Helium purge.

As combustion starts, the cooling ϕ must be controlled to accommodate increasing heat fluxes. The variations among missions occurring during the combustion phase are as follows:

Case I - Shown in Figure 3.2-1. Cooling ϕ is in excess of combustion ϕ. Combustion ϕ will ramp at beginning and end of test. Ramps of 5-sec duration to and from $\phi = 1$ may be assumed at beginning and end of test.

Case II - Not shown. Represents a gradual change in conditions shown for Case I and will involve less severe transients. Not considered a design point.

Case III - Same comments as Case II, but may become a design point at lower Mach numbers because of potential for increased test time and wider Mach number range.

Case IV - Shown in Figure 3.2-1. Involves a near-step change in gas-side engine conditions during test run.

Case V - Shown in Figure 3.2-1. The general rise in pressure would be expected to cause a step-change type increase in heat flux. Spike will extend and close, then retract to operating position for second attempt at starting. At this point, either normal operation or a second unstart is possible.

4.0 OVERALL APPROACH

The diverse requirements imposed on the cooled structures require iteration of the cooled structural design with (1) the engine aerodynamic design; (2) the instrumentation, control, and fuel subsystems designs; and (3) the airplane interface design. Internal contraints on cooled structural design are imposed by the close coordination required in thermal design, structural design, mechanical design, and manufacturing. It is generally not possible to treat any one of these areas independently of the others. During Phase I of the program, the basic design concepts for the engine were defined and are basically feasible in terms of the constraints imposed on the design. These concepts and the design data generated during Phase I are being used as the starting point for design of the Phase IIA cooled structures. Component layout drawings of acceptable mechanical design and with acceptable manufacturing features form the initial step in the iteration. These layout drawings have been evaluated to establish the required thermal and structural design features. Based on these inputs, layout drawings are revised to incorporate the required features, followed by substantiation of thermal and structural performance of the revised design.

Although the Phase I design is being used as the starting point of Phase IIA cooled structure design, each of the components is being reviewed with the objective of simplification in terms of mechanical design and manufacturing features. The interfaces between two or more components, in particular, will be reevaluated . The interfaces include engine-to-airplane mounting, outer-shell-to-innerbody mounting by means of the support struts, nozzle-to-inner-shell assembly, inlet spike-to-innerbody assembly, inlet spike actuator-to-inlet spike and innerbody mounting, leading edge-to-outer shell mounting, and cowl-to-outer shell support.

The general approach to cooled structures development places heavy emphasis on fabrication and testing of the full-scale components. A limited number of types of cooled structural elements and models is being fabricated and tested to evaluate the problems which are basic to the overall engine design, or which are sufficiently localized in nature to permit use of subscale evaluation. All significant manufacturing development and evaluation is being accomplished using the full-scale components. The nature of the required manufacturing operations for the components is such that use of subscale components would be expected to lead to only limited information on the adequacy of manufacturing techniques and processes.

4.1 THERMAL DESIGN

The overall thermal design approach is by analyses based on experimental data obtained from tests on similar geometric configurations and heat transfer situations. These experiment-based analyses, in turn, will be verified by experiments where the geometry or fluid conditions, or both, will be like those existing for the flight engine.

Where the discrepancy between calculated and experimental heat flux values is large, steps are being taken to improve the analytical techniques so that the correlation between calculated and experimental results can be improved.

The basic goals of all thermal analyses and designs are (1) limiting temperature and temperature differences to structurally acceptable values, while keeping hydrogen cooling flow equal to or less than hydrogen flow required for combustion, and (2) at the same time maintaining hydrogen pressure drop compatible with cooling jacket pressure containment and pump outlet pressure capabilities. The limiting values being used at present are (1) a maximum gas side metal temperature of 1700°F (2160°R), (2) a maximum primary structure temperature of 1140°F (1600°R), and (3) a hydrogen pump outlet pressure of 1100 psia.

The thermal design procedure involves separate calculation of aerodynamic heating and cooling jacket performance. The aerodynamic heating conditions are calculated (as during Phase I) primarily by use of the computer program H1940. Special aerodynamic heating conditions, such as shock wave/boundary layer interaction, are computed separately. Cooling jacket fin performance is calculated (as in Phase I) by use of computer program H1930. Special conditions, such as pressure and flow distributions for inlet, outlets, and bolted flange/manifolds, require separate calculations. Verification of aerodynamic and cooling jacket heat transfer and pressure drop calculations will be accomplished by actual tests. Specifically, aerodynamic heat transfer calculations will be verified by tests of engine component models, such as the combustor, and with the boilerplate engines. Calculated performance of cooled structures will be verified by full-scale component and some subscale component testing at heat flux levels and distributions comparable to those calculated for the flight engine components. The primary areas requiring verification in the cooled structures performance are flow distribution and associated temperature distribution and its effects on structural performance in terms of life and contour.

4.2 STRUCTURAL DESIGN

The structural design approach utilizes a combination of analytical and experimental methods. Experimental verification of detailed parts, such as short-term burst, creep-rupture, and thermal fatigue tests on sandwich plate-fin elements, will be employed wherever necessary. Generally, the structural tests will be performed on composite structural elements, such as the inlet spike and the innerbody assembly.

The bulk of the HRE structures consists of ring-stiffened orthotropic shell structures of variable thicknesses and contours. The ring stiffeners are also used for coolant flow manifolding and fuel injection rings for the engine combustor section. The structural loadings will produce axisymmetric and asymmetric forces and moments due to static normal pressures, acceleration, vibrational inputs, and aerodynamic flutter and buffeting effects.

Fully operational computer solutions are available to analyze axisymmetric isotropic thin shells of variable thicknesses and contours for stresses due to axisymmetric loads and temperature profiles. In addition, the isotropic shell analysis had been extended to treat orthotropic cylindrical shells with axisymmetric loads. Two MIT finite difference nodal circle solutions (SABOR III and DASHER I), which have been adapted for use on the AiResearch computer system (IBM-360/50), are available for use.

The SABOR III program is applicable for axisymmetric isotropic shells (local departures from ideal isotropy can be treated) that may be subjected to nonsymmetrical static forces. The SABOR III program may also be used to obtain the stiffness and mass matrixes for direct input into the DASHER I program to obtain dynamic response.

It would have required an extensive programming effort to modify the SABOR III and DASHER I programs to treat accurately many of the problems that will be encountered in the HRE. Rather than attempt this approach, a further survey of existing shell programs was carried out, and it was determined that an extremely applicable program had been developed under the auspices of the Analysis Group of the Theoretical Mechanics Branch, Structures Division of the Wright Patterson Air Force Base, Dayton, Ohio. This program is based upon the very recent improvement in matrix shell solutions generated by A. Kalnins (Department of Mechanics, Lehigh University). It solves the general axisymmetric orthotropic thin shell problem for symmetric and nonsymmetric loads due to static as well as dynamic inputs. The program has been successfully adapted for use on the AiResearch computer system. Although the program has been debugged, the final report describing the usability limitations, and methods of data input has not been completed, and will not be releasea oy the Wright Patterson Air Force Base for at least twelve months. Until a program of this magnitude has been completely checked out by trying numerous test cases, a note of caution must be exercised regarding its capabilities. Another important point is the fact that the problem inputs and the data reduction of the outputs require considerable effort on the part of the user. The existence of the program also does not eliminate or substantially reduce the work needed to generate a sound design; however, it is the objective of careful analysis to discover design inadequacies that would otherwise not be recognized.

The eventual objective of the test program is to verify the actual performance capabilities of the structures as fabricated. Although it will not be possible to predict analytically the influence of realistic fabrication restrictions and limitations on the end product, the initial analysis will identify the serious design problem areas. Results of the test program will be used to assess the extent of the changes required to achieve the structural integrity goals.

4.3 MECHANICAL DESIGN

The guidelines used in mechanical design of the cooled structures components and assembly of the components into the engine require the use of known materials and joining techniques. Standard fasteners and seals are used to the greatest extent possible. Design for brazing is aimed at minimizing the total number of braze cycles to which a given part must be subjected. In some cases, this is done by redesigning the parts to allow use of prebrazed subassemblies, substitution of machined or welded subassemblies, or substitution of bolted interfaces for brazed or welded interfaces. Also, as a general rule, all welding into or close to braze joints is being avoided, although in certain cases, such a procedure may be acceptable.

The mechanical design effort will be supported by experimental verification in selected areas. In particular, selected configurations that present analytical problems and raise questions as to manufacturing feasibility will be fabricated and tested on a subscale basis. The purpose of such tests will be to provide design data and guidance for possible design revision. Currently planned tests, which are in support of mechanical design rather than thermal or structural design, include the following:

Test specimen to evaluate feasibility of bolting the nozzle flange manifold to the inner shell through the removable nozzle cap

Fabrication of a section of the inlet spike near the spike tip to help resolve questions regarding the best manufacturing approach and hence the best design for this portion of the inlet spike

Fabrication of the spike-to-innerbody seal to evaluate the adequacy of the design solution

Fabrication of a straight section of the bolted nozzle manifold to verify both the manufacturing aspects and structural integrity of the design solution

Fabrication and evaluation of the various mechanical seals used in the components to verify the adequacy of the design solution

Fabrication of flat panels using the various instrumentation and fuel injector fittings that penetrate the regeneratively cooled surfaces to verify manufacturing feasibility and structural integrity of the design. Tests results will be used to select the final configuration used in the engine.

4.4 MANUFACTURING

The manufacturing approach being used on this program has two aspects: (1) that dealing with the approach to development of manufacturing techniques and processes, and (2) that dealing with the specific manufacturing processes planned for use.

4.4.1 Development Approach

The development of the manufacturing techniques and processes will rely primarily on full-scale components. Except where isolated problems or basic data must be obtained, the use of subscale components represents a duplication of development effort. The compound forming of the shell-face sheets in half-scale, for example, results in working with radii of curvature which are half those encountered in the full-scale part. Use of lighter gauge material to facilitate forming, on the other hand, is impractical. In addition, the size of the full-scale tooling, the machines required to use this tooling, and the unique problems associated with the forming of large thin wall shells cannot be duplicated in half-scale. As a result, a half-scale compound-curved model of the isentropic surface of the inlet spike is the only subscale component on which fabrication development work is being done. This part is being used to establish forming characteristics, evaluate electrohydraulic forming parameters, and investigate brazing problems.

4.4.2 Fabrication Approach

The most critical area of cooled structures fabircation is in the cooled surface shell face sheets. The starting point for these shells can either be rolled and welded cone sections or flat sheets. The rolled and welded cones are bulge-formed, then final-sized, using electrohydraulic forming. Using flat sheets as a starting point, the shells must be deep drawn in about three stages. Final sizing of the shells occurs as for the welded cones. Of the two approaches, the one using the seam-welded cone has been selected. The weld seam is not considered structurally objectionable and the approach involves fewer steps than are required for deep drawing.

To ensure adequate braze fitup, forming accuracy for the shells must be high. Specifically, it is expected that the clearance between shells must be maintained within a tolerance of approximately ±0.001 in. Given this accuracy, the brazing of the fins between the face shape still requires special attention. To ensure sound braze joints, pressure must be exerted on the shells in such a way as to provide a crushing load on the fins. The methods available for providing this braze fixturing load include the following, as a function of the component being brazed:

> Graphite fixtures, with an external piece containing the assembly and an internal piece using expanding segments to exert pressure.
>
> Steel bags placed inside the shell and pressurized to a level sufficient to deform the shell with which the bag is in contact. Containment on the external face sheet may or may not be required with this approach.
>
> Evacuation and backfilling of the space between the two shell face sheets, using atmospheric pressure to provide the load.

Integrity of the shell joining will be experimentally evaluated and adjustments in shell forming tools and brazing procedures and fixtures made to correct problems that appear.

4.4.3 Nondestructive Testing

The critical area in fabrication of the full-scale components involves the shells themselves, as discussed in the two previous paragraphs. For structural integrity of the shells, only very limited areas of unbrazed joint areas are tolerable. These joints are detectable by proof pressure testing at sufficiently high pressure levels. Only in exceptional cases, however, will a defect that is revealed by proof pressure test be repairable. In general, a nondestructive test capable of revealing braze voids is preferable and offers better opportunity for subsequent repair. The two techniques available are radiographic inspection of the entire shell surface and the use of temperature-sensitive paint on one of the face sheets with a heating transient imposed on the other face sheet. These methods will show a braze void; that is, an unbonded joint. Weak joints are not discernable as such. In general, however, the existence of a brazed joint is reasonable assurance that adequate joint strength can be achieved. Verification of the result of radiographic or thermal inspection of the shells will be done by proof pressure testing.

The repair techniques available for unbonded joints in the shells would generally be the following:

> Recycling of the complete shell to a slightly higher temperature than used during the first braze cycle. In this way, remelt and flow of the braze alloy is obtained with the objective of filling the void. Orientation of the shell in the brazing furnace can be used to assist the process.
>
> Removal of a portion of the face sheet in the unbrazed area, addition of filler alloy and closeout using a patch, with the entire shell recycled in the brazing furnace. The applicability of this repair procedure will be a function of the location of the affected shell area in the engine gas stream.

5.0 ANALYTICAL DESIGN

Efforts in the analytical design have been concerned with evaluation of operating points not previously analyzed, and review of leading edge areas. Specifically, HRE operation at M = 8 freestream, (88,000-ft altitude) was analyzed, and evaluation of operation of the HRE in a wind tunnel environment (NASA Langley 8-ft hot-structures tunnel) was started. The cowl leading edge and strut leading edge heating and cooling problems were reviewed using experimental data and revised analytical methods.

5.1 AERODYNAMIC HEATING

Heat transfer analysis has been completed for the HRE (ARJ-IC) hydrogen cooled surfaces at Mach 8 freestream (Mach 8 local), 88,000-ft altitude (B-B line) flight conditions with a fuel ϕ of 1. This flight condition has been selected as a reference condition for HRE wind tunnel testing. The objective of the aerodynamic heating analysis was to select hydrogen flow rates in the cooled passages to fulfill the following engine structural design goals.

(a) Maintain hot-gas-side metal temperatures at, or below, 2060°R (1600°F)

(b) Maintain primary structural temperatures at, or below, 1600°R (1140°F)

(c) Maintain cross sectional temperature differences to values at, or compatible with, the desired fatigue life of the structure

(d) Minimize the coolant hydrogen usage in excess of combustion requirements

(e) Maintain hydrogen pressure drop compatible with plate-fin panel pressure containment, pump outlet pressure capabilities (1100 psia) and fuel plenum pressure requirements (525 psia)

(f) Minimize structural temperature differences from innerbody to outerbody at the same axial station in order to minimize distortion and thermal strain of the hot gas annular passage

The general results and conclusions of the thermal analysis are discussed below.

(a) The total engine hydrogen coolant flow rate required to fulfill goals (a) through (f) above, is 2.19 lb/sec at pump outlet conditions of 100^0R and 965 psia. The hydrogen fuel required at this flight condition (fuel ϕ = 1.00) is 0.762 lb/sec which gives a cooling ϕ of 2.88. A total coolant flow rate of 3.0 lb/sec at 100^0R and 1100 psia pump outlet conditions was reported for Mach 6.5 local conditions at a fuel ϕ of about 0.76.

(b) Plate-fin panel cross-section temperature differences can be maintained below 800^0R except on the leading edge and forward outer shell where ΔT's up to 950^0R are predicted. In addition, localized ΔT's of up to 1200^0R due to shock impingement have been calculated. These localized cross section ΔT's occur on the outer shell fuel injector (ΔT = 1200^0R at Station XX = 47), and on the inner and outer shells (ΔT = 900^0R at Station 59.6).

(c) By use of a 30-mil-thick nickel fin brazed to the stagnation line in the coolant hydrogen passage of the strut leading edge, the maximum metal temperature at the stagnation point can be reduced to 1600^0R, and the ΔT (maximum metal temperature to coolant) to 1500^0R. These results are discussed in Section 5.2.

(d) The spike tip can be adequately cooled to a maximum tip metal temperature of 770^0R with spike open, and 1260^0R with spike closed.

(e) The best cowl leading edge flow configuration appears to be with perpendicular flow and a 150-deg turn. The maximum leading edge temperature of 1506^0R and ΔT of 1206^0R occurs with spike closed and a flow of 0.18 lb/sec rather than 0.076 lb/sec--the flow required to give a 1600^0R forward outer shell outlet temperature. The temperatures are expected to be lower for other conditions, including spike-open with spike shock impinging on the leading edge.

5.1.1 Aerodynamic Parameters

The aerodynamic data (static pressure, velocity, fuel-fraction burned) of air and combustion products of hydrogen fuel and air flowing adjacent to engine surfaces are presented in Figure 5.1-1. The aerodynamic data for the outer surface of the outerbody are presented in Figure 5.1-2, and for the strut sides in Figure 5.1-3.

The aerodynamic parameters presented in Figures 5.1-1 and 5.1-2 were used with Eckert's reference enthalpy in flat plate aerodynamic heat transfer calculations, as outlined in Reference 1 to determine hot gas convective heat transfer coefficients and adiabatic wall temperatures along the cooled panel surfaces of the engine. Hot gas heat transfer coefficients on the spike surface were multiplied by the cone-rule factor ($3^{0.5}$ for laminar flow and $2^{0.2}$ for turbulent flow) from spike tip to the axial location of the cowl leading edge (XX = 39.2056). The cone-rule factor was not used on other engine surfaces. Laminar to turbulent flow transition was considered to occur at XX = 20.0

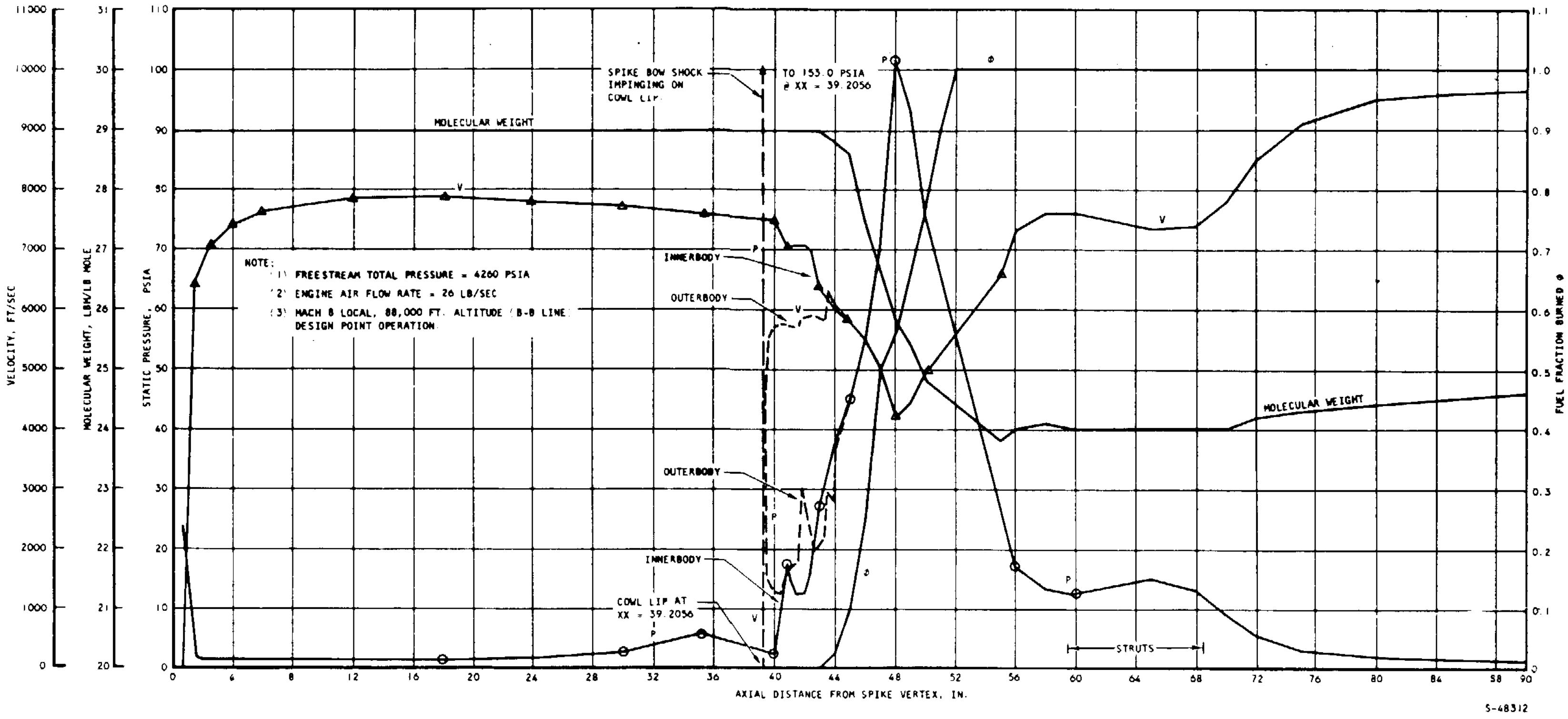

NOTE:
(1) FREESTREAM TOTAL PRESSURE = 4260 PSIA
(2) ENGINE AIR FLOW RATE = 26 LB/SEC
(3) MACH 8 LOCAL, 88,000 FT. ALTITUDE (B-B LINE) DESIGN POINT OPERATION

Figure 5.1-1 HRE Aerodynamics Parameters

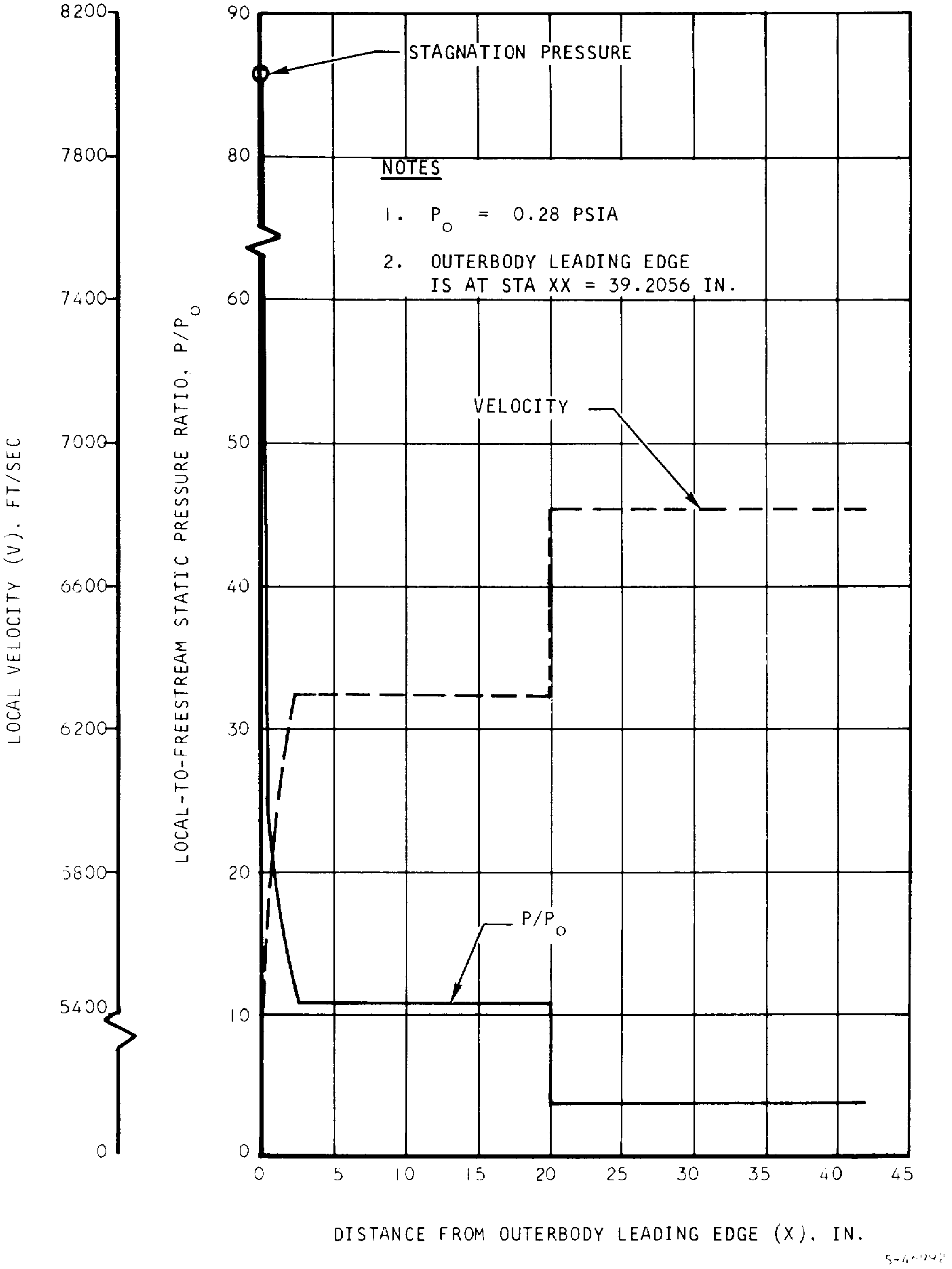

Figure 5.1-2 HRE Aerodynamic Parameters, Outer Cowl Surface

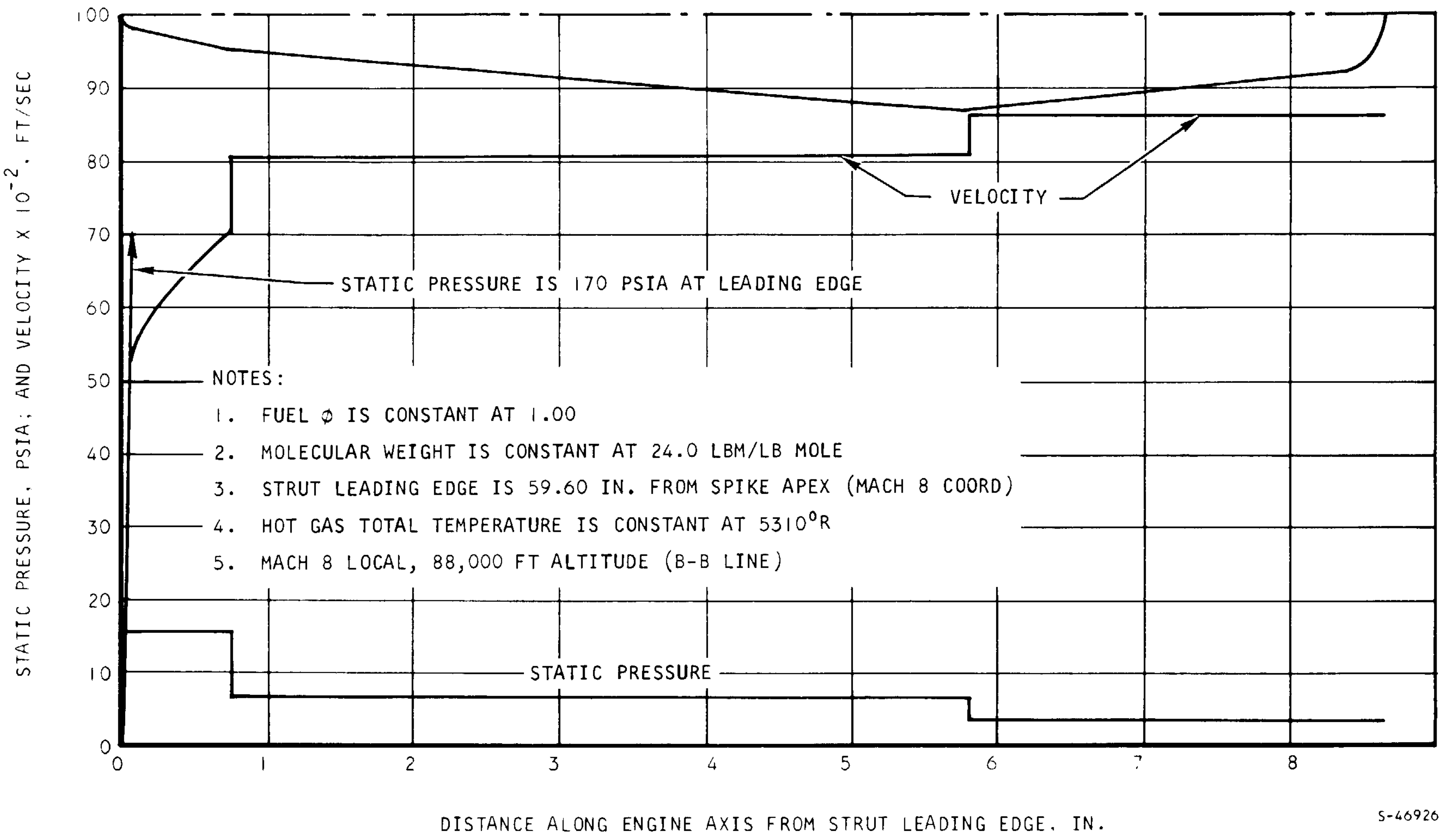

NOTES:

1. FUEL ϕ IS CONSTANT AT 1.00
2. MOLECULAR WEIGHT IS CONSTANT AT 24.0 LBM/LB MOLE
3. STRUT LEADING EDGE IS 59.60 IN. FROM SPIKE APEX (MACH 8 COORD)
4. HOT GAS TOTAL TEMPERATURE IS CONSTANT AT 5310°R
5. MACH 8 LOCAL, 88,000 FT ALTITUDE (B-B LINE)

Figure 5.1-3 HRE Strut Aerodynamic Parameters

($Re = 1 \times 10^7$) on the spike, and XX = 39.60 ($Re = 1 \times 10^5$) on the inside surface of the cowl leading edge. The aerodynamic flow as considered laminar on the outside surface of the leading edge and turbulent on the outside surface of the trailing edge.

Shock impingement which occurs on the inner shell surface at XX = 57.5 is caused by the rearward facing step at the end of the spike, XX = 55.76. A heat flux increase of twice the local flat plate calculation was estimated from Reference 2 for this shock impingement.

The local aerodynamic velocities and static pressures adjacent to the strut sides shown in Figure 5.1-3 were calculated based on equilibrium properties for oblique shock and expansion waves with the aerodynamic velocity and static pressure from Figure 5.1-1 just upstream of the struts. The aerodynamic heat transfer coefficients along the strut sides were calculated with Eckert's reference enthalpy and flat plate equations of Reference 1.

5.1.2 Heat Flux and Temperature Distributions

Net heat flux and the resulting metal temperatures and temperature differences along the cooled plate-fin panels are presented in Figures 5.1-4 through 5.1-10. Thermal results for the spike folded-flow section (XX = 46.00 to XX = 55.76) are presented in Figures 5.1-4 and 5.1-5.

Plate-fin panel cross-section temperature differences can be maintained below 800°R except on the leading edge (Figure 5.1-7) and forward outer shell (Figure 5.1-8). A cross section ΔT of 950°R is predicted across the 20R - .050 - .100(0) - .006 offset fins and 0.015-in.-thick hot sheet on the leading edge at the leading edge/forward outer shell interface (XX = 46.745). On the forward outer shell, a ΔT of 930°R is predicted across the 28R - .050 - .100(0) - .006 offset fins and hot sheet at XX = 48.00.

Localized cross section ΔT's due to high shock impingement heat fluxes have been calculated but are not shown in the figures. The localized areas are as follows:

(a) Hydrogen fuel entering the hot gas stream through the injectors at Station XX = 43 on the spike and at Satation XX = 47 on the outer shell will cause a shock system with reattachment of separated flow on surfaces just upstream of the injectors. The local heat flux is increased from 255 Btu/sec-ft^2 shown in Figure 5.1-4 for the spike to 280 Btu/sec-ft^2. The resulting cross-section ΔT increases from 470° to 520°R (outer wall temperature = 915°R).

(b) The local heat flux at Station XX = 47 on the outer shell increases from 600 (Figure 5.1-8) to 865 Btu/sec-ft and the corresponding ΔT increases from 900° to 1200°R (outer wall temperature = 2060°R).

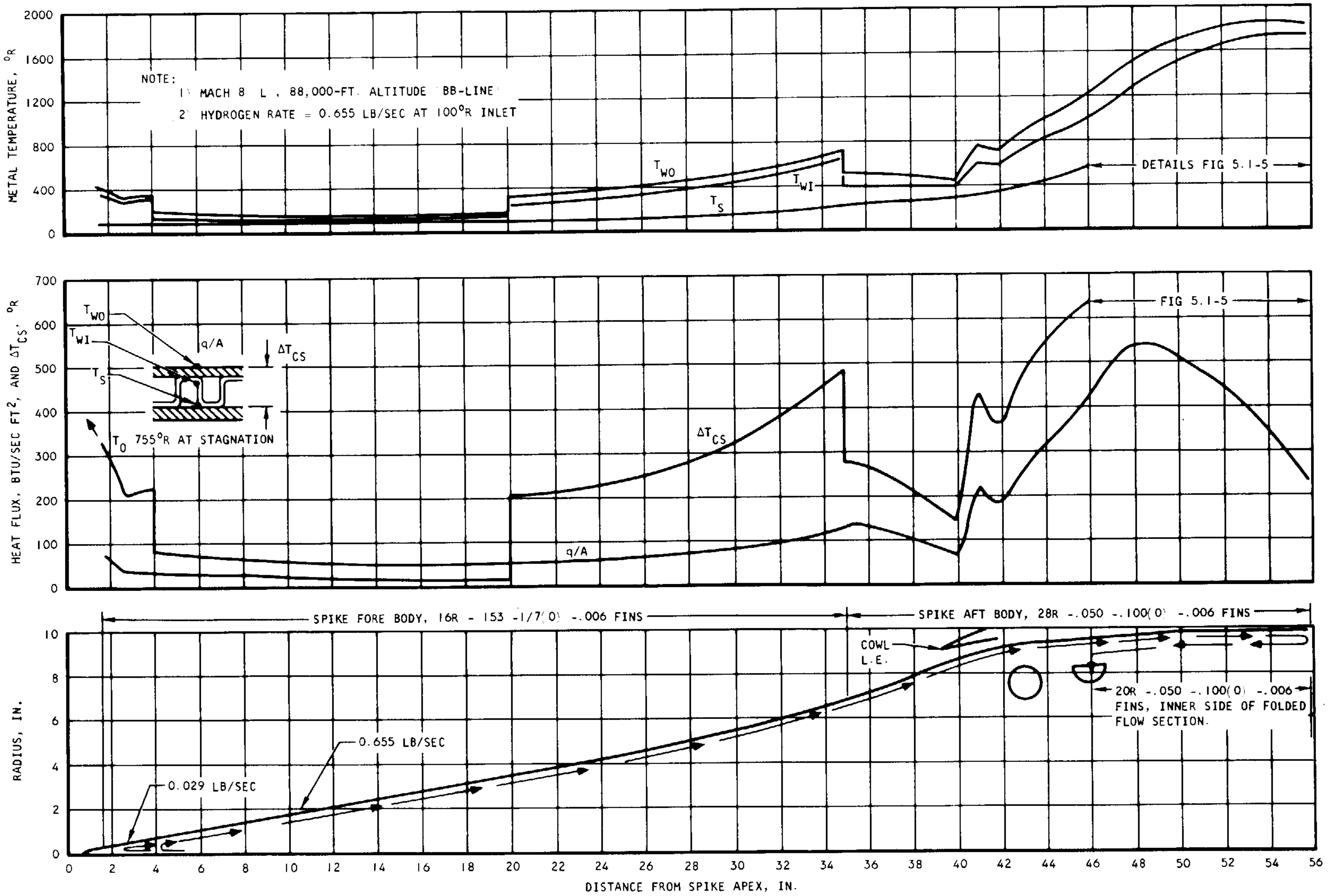

Figure 5.1-4 HRE Inlet Spike Thermal Performance

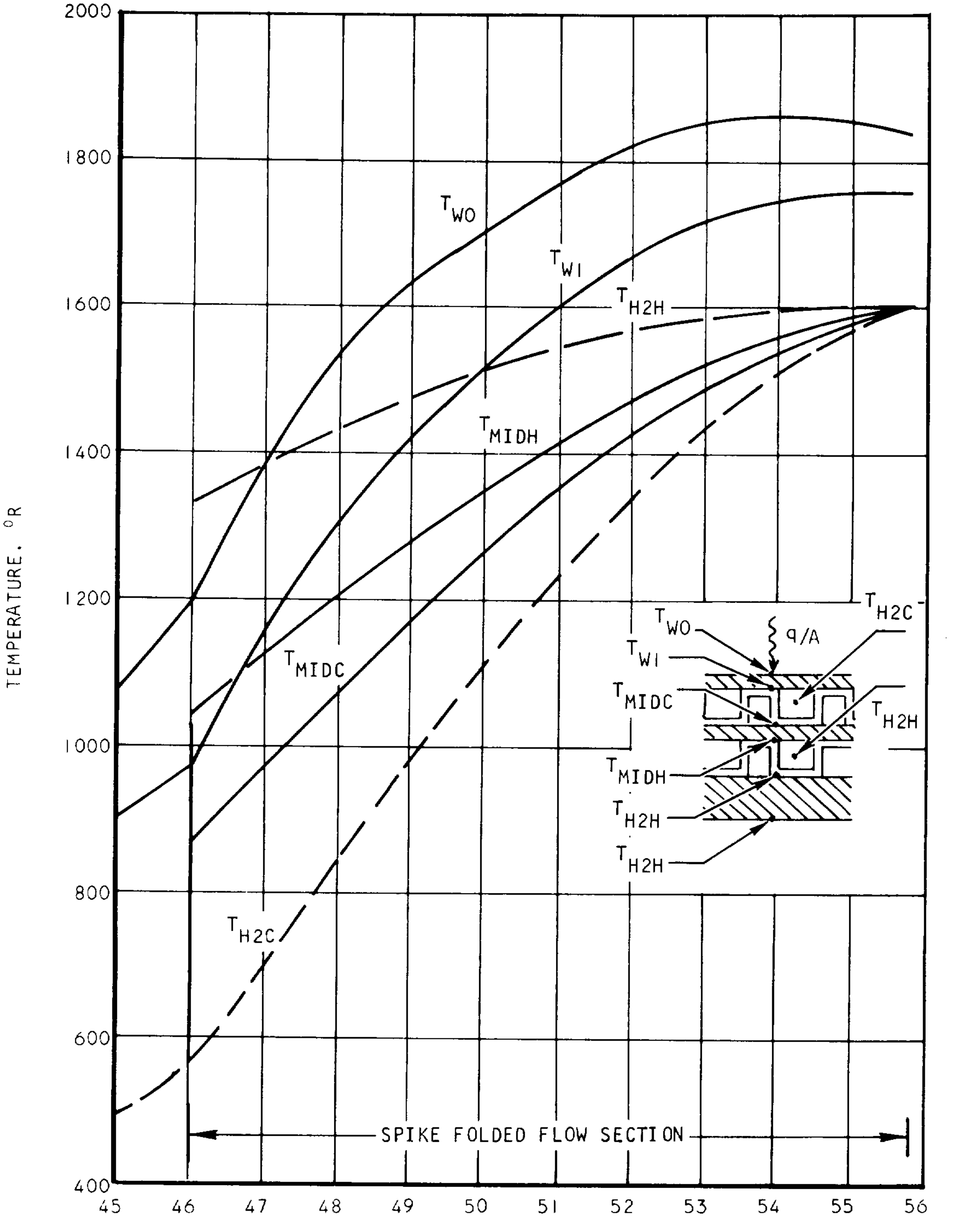

Figure 5.1-5 Spike Folded-Flow Section Thermal Performance

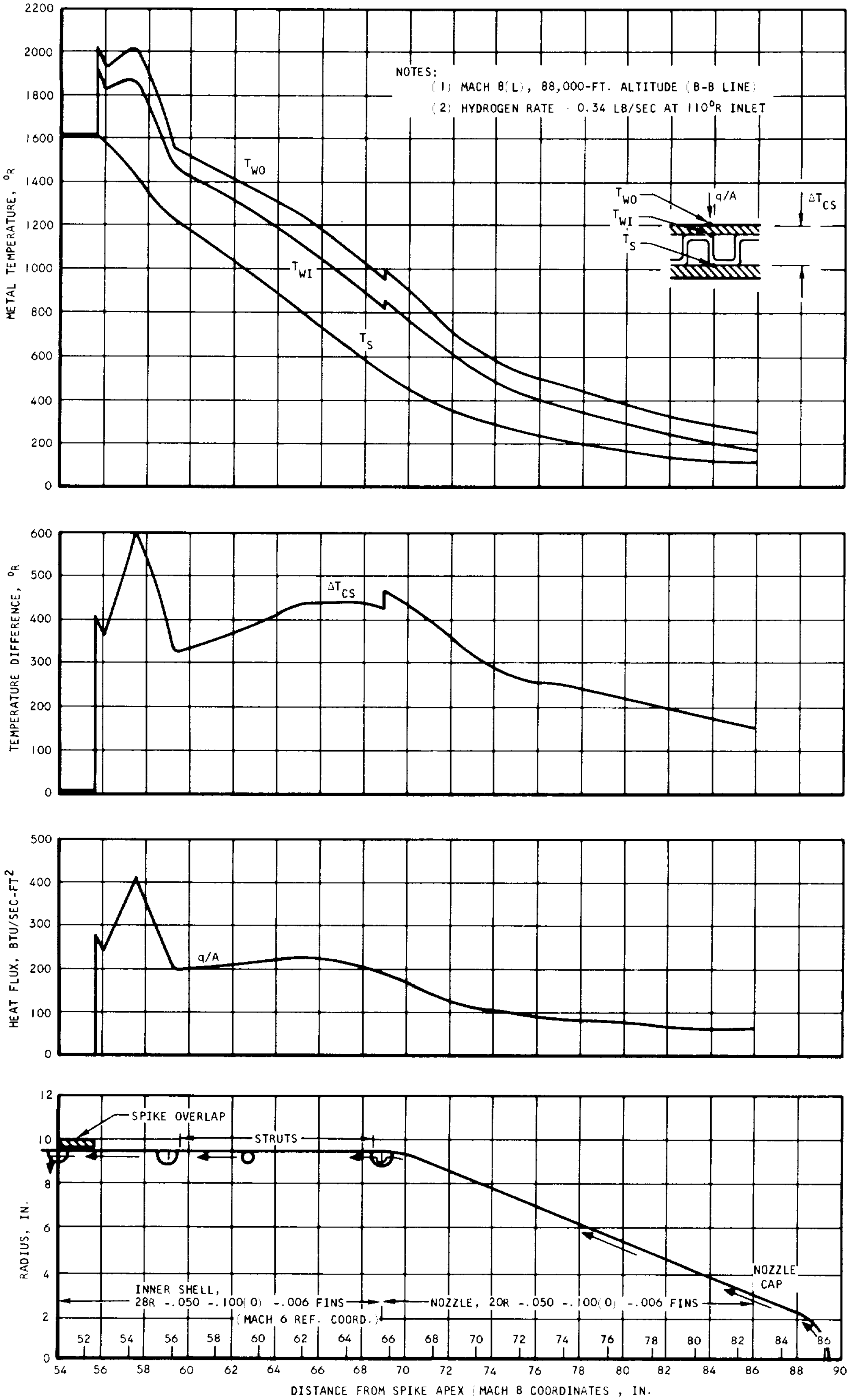

Figure 5.1-6 HRE Innerbody Thermal Performance

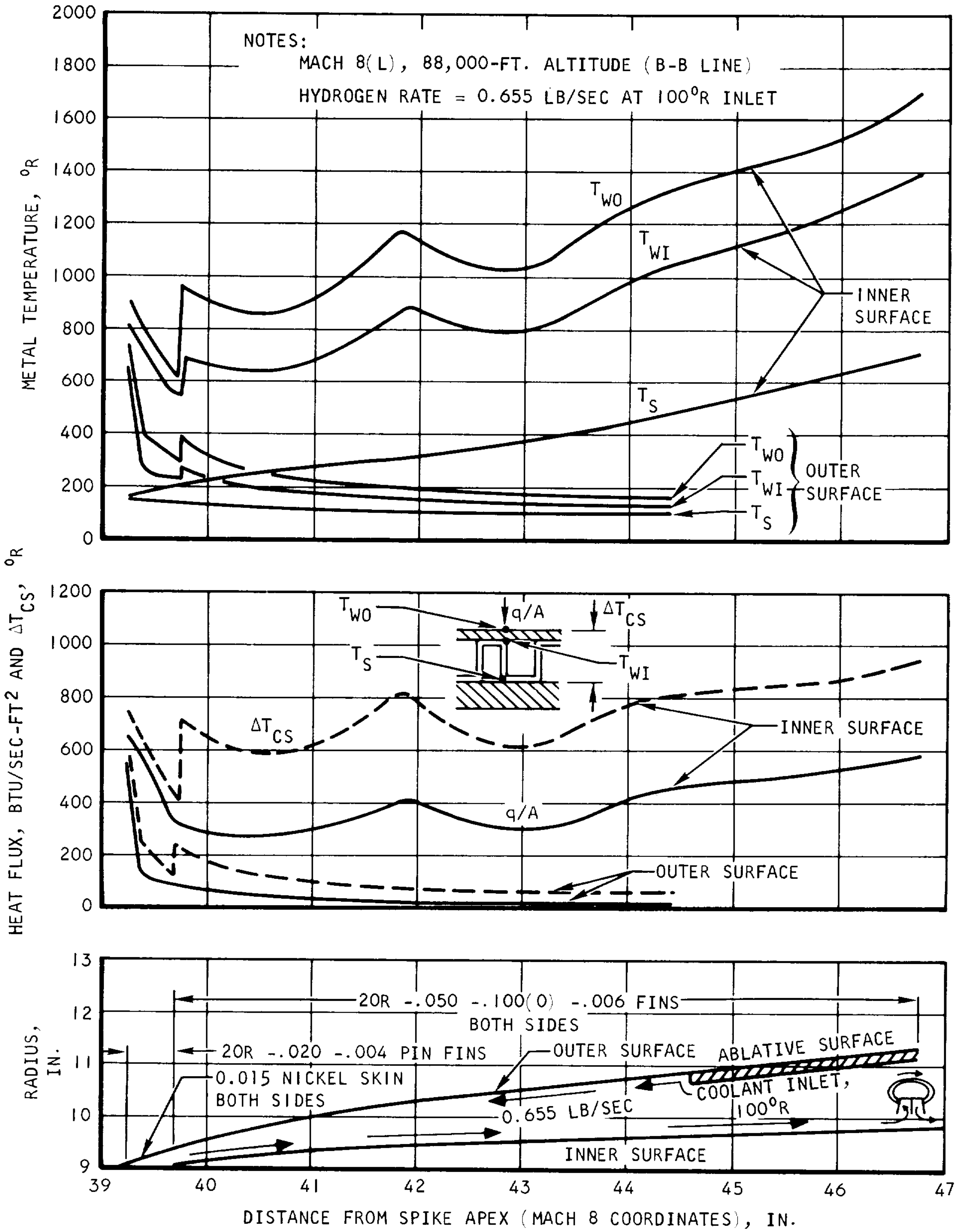

S-48309

Figure 5.1-7 HRE Leading Edge Thermal Performance

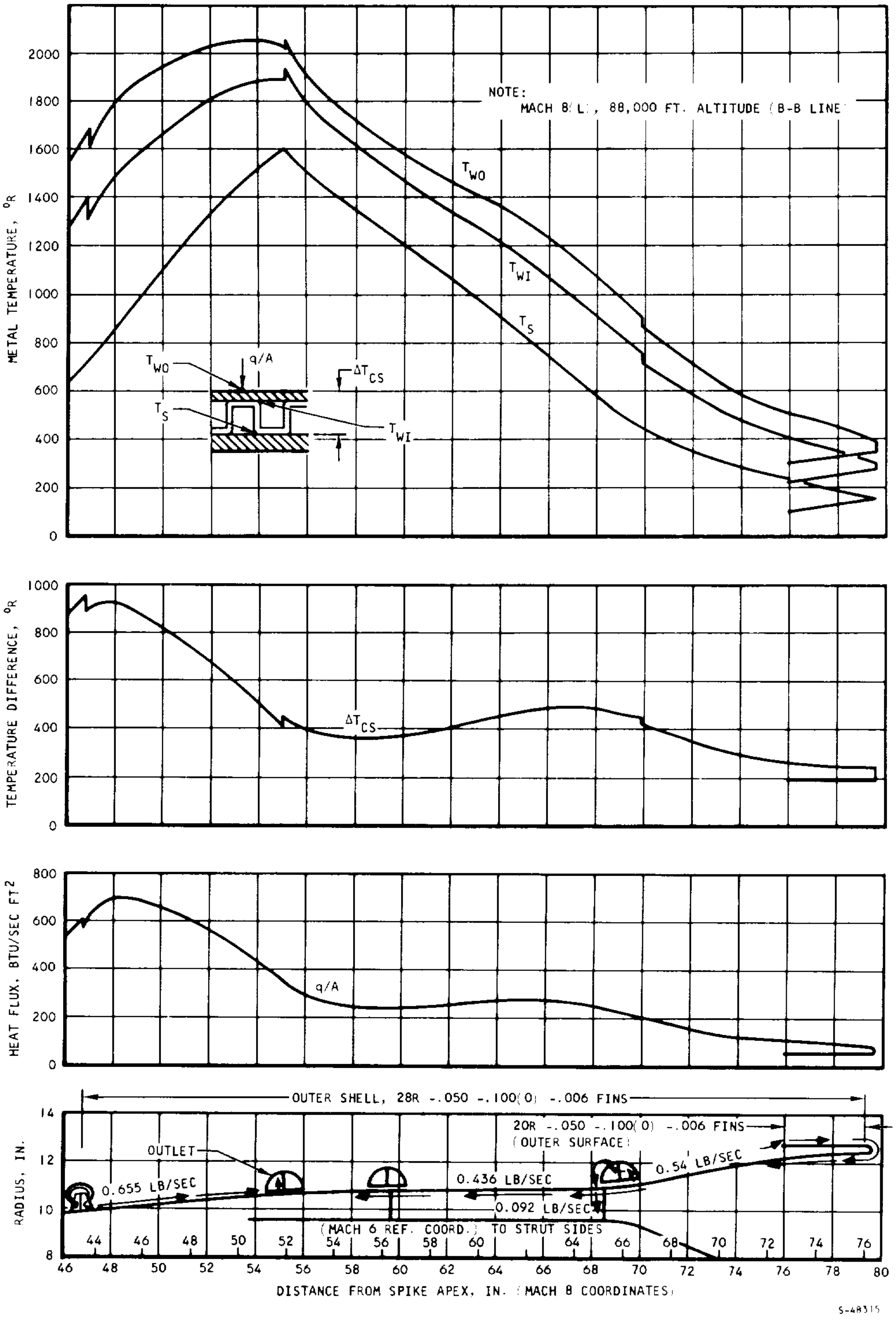

NOTE:
MACH 8 (L), 88,000 FT. ALTITUDE (B-B LINE)

Figure 5.1-8 HRE Outer Shell Thermal Performance

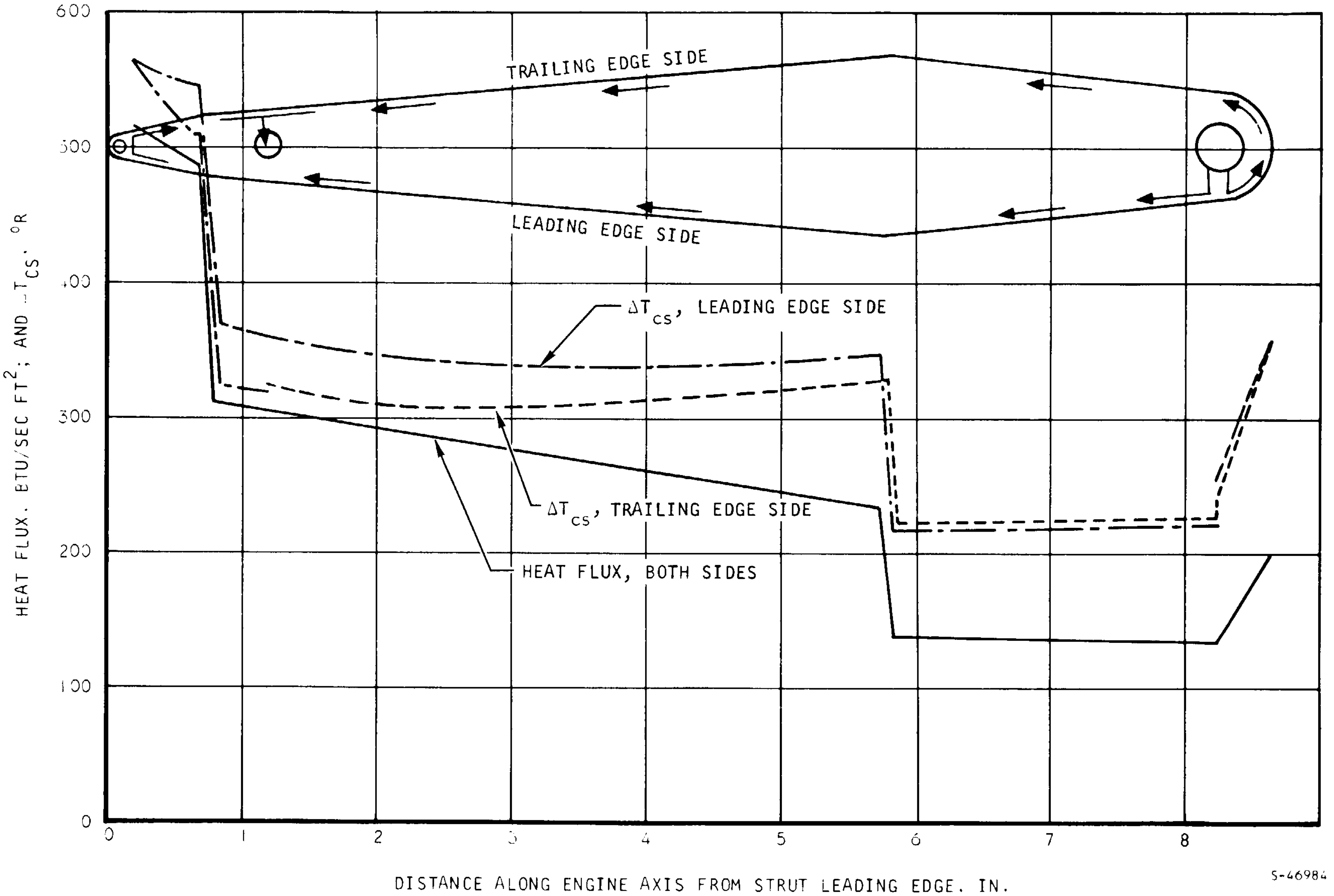

Figure 5.1-9 HRE Struts Thermal Performance

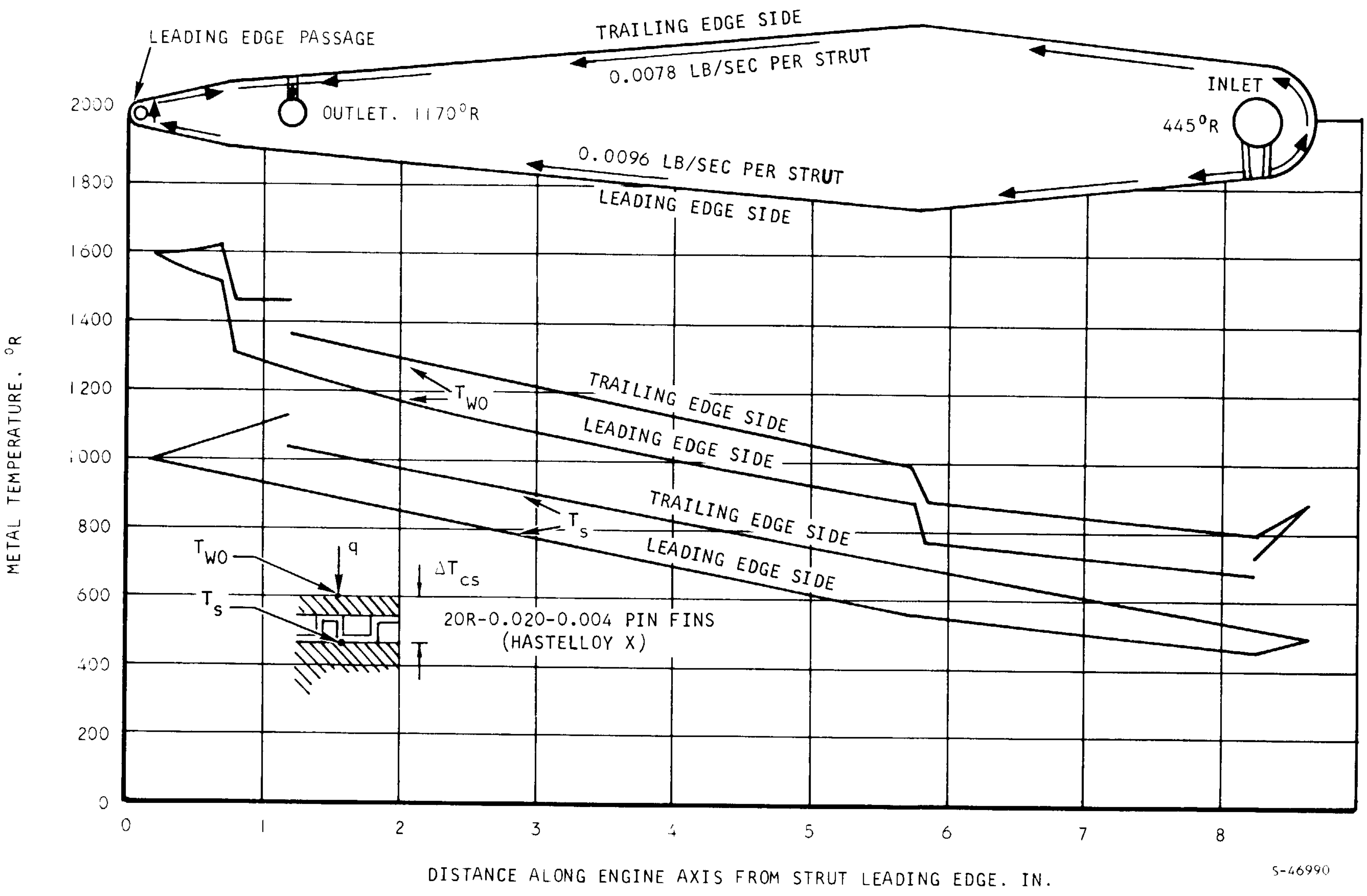

Figure 5.1-10 HRE Struts Thermal Performance

(c) **Localized** high heat fluxes occur on the inner and outer shells just upstream of the strut leading edge (Station XX = 59.6). These heat fluxes are caused by reattachement of separated flow associated with the strut bow shock waves. The hot gas heat flux is locally increased from 200 Btu/sec-ft^2 to 600 Btu/sec-ft^2 and the cross section ΔT is is locally increased from 325^0 to 900^{0}R (outer wall temperature = 2100^{0}R).

(d) The effect of cowl leading edge shock impingement on the spike at Station XX = 40 was investigated. The pressure rise created by shock impingement takes place over a 1-in. length (Figure 5.1-1), and results in an increase in ΔT from 430^0 to 680^{0}R at Station XX = 41.

Localized ΔT's were calculated on a one-dimensional basis, but modified to account for two-dimensional heat transfer by multiplying the hot gas heat transfer coefficient by 0.7.

The spike tip will be cooled with 100^{0}R hydrogen impinging on the inner surface of the tip. The impinging hydrogen is a fixed 4.5 percent of the total spike coolant rate and is routed in parallel with the remainder of the spike flow in the region of the tip (Figure 5.1-4). At Mach 8 local, 88,000-ft altitude, the aerodynamic heat flux at the tip stagnation point is 560 Btu/sec-ft^2 as calculated by the method of Fay and Riddell (Reference 3). With an impinging hydrogen rate of 0.0295 lb/sec (4.5 percent of total spike coolant rate of 0.655 lb/sec) a tip outer surface temperature of 755^{0}R was calculated. The corresponding inner surface temperature of the tip is 325^{0}R. The convective heat transfer coefficient for coolant hydrogen impinging on the inner surface was calculated at 2.6 Btu/sec-ft^2 from a correlation presented in Reference 4.

When the inlet is closed at Mach 8, 88,000-ft altitude, the spike coolant demand is 25 percent of that required during design point operation, 0.655 lb/sec. The spike tip flow rate will be 25 percent of 0.0295 lb/sec or 0.0076 lb/sec but the aerodynamic heating rate at the tip will be the same as with inlet open and with combustion. At this condition, the predicted outer surface temperature is 1250^{0}R and the inner surface temperature is 1010^{0}R.

5.1.3 Coolant Requirements

The hydrogen flows and outlet temperatures required for each component are summarized below. The inlet temperature is 100^{0}R.

	Flow Rate, lb/sec	T_{out}, ^{0}R
Spike	0.655	1300
Strut L.E. (each of six)	0.057	110
Innerbody (from strut L.E.)	0.340	1600

Continued...	Flow Rate, lb/sec	T_{out}, °R
Leading edge/forward outer shell	0.655	1600
Aft outer shell (to XX = 69.6)	0.540	445
Aft outer shell (from XX = 62.6 to XX = 55.0)	0.448	1600
Strut sides (from aft outer shell)	0.092	1060
Total	2.19	
Average		1470

5.2 STRUT LEADING EDGES

As discussed in more detail below, a plain round passage in the strut leading edge is not able to provide adequate cooling with 100°R hydrogen when the wall-to-bulk temperature ratio effect is included in evaluation of the hydrogen heat transfer coefficient. A nickel fin brazed into the leading edge passage should provide acceptable metal temperatures.

5.2.1 Aerodyanamic Heating

The aerodynamic conditions reported in Section 5.1.1 were used with the Fay-Riddell theory (Reference 3) to obtain the stagnation heat transfer coefficient noted in Figure 5.2-1. Recent strut wind tunnel tests reported in Reference 5 and updated in this report have indicated that hot gas stagnation heat fluxes could be about 1.8 times heat flux values predicted from Reference 3 at the unit Reynolds number behind the shock of 0.94×10^6 per ft expected in the flight engine. This increase is thought to be due to a high freestream turbulence level and leading edge surface roughness, both of which may be present in an operating engine.

5.2.2 Cooling

The leading edges of the six struts (Figure 5.2-2) will be cooled with nominal 100°R hydrogen. After flowing through the strut leading edges, the hydrogen cools the innerbody. The strut leading edges/innerbody coolant rate of 0.34 lb/sec (or 0.057 lb/sec per strut leading edge) was selected to provide adequate cooling to the innerbody.

A two-dimensional thermal analysis was performed on the leading edge for a coolant rate of 0.057 lb/sec. Coolant heat transfer coefficients were predicated from a correlation presented in Reference 6. Results presented in Figure 5.2-1 for a round passage without a fin indicate a maximum outer wall temperature of 2600°R and an inner wall temperature of 2270°R. These high

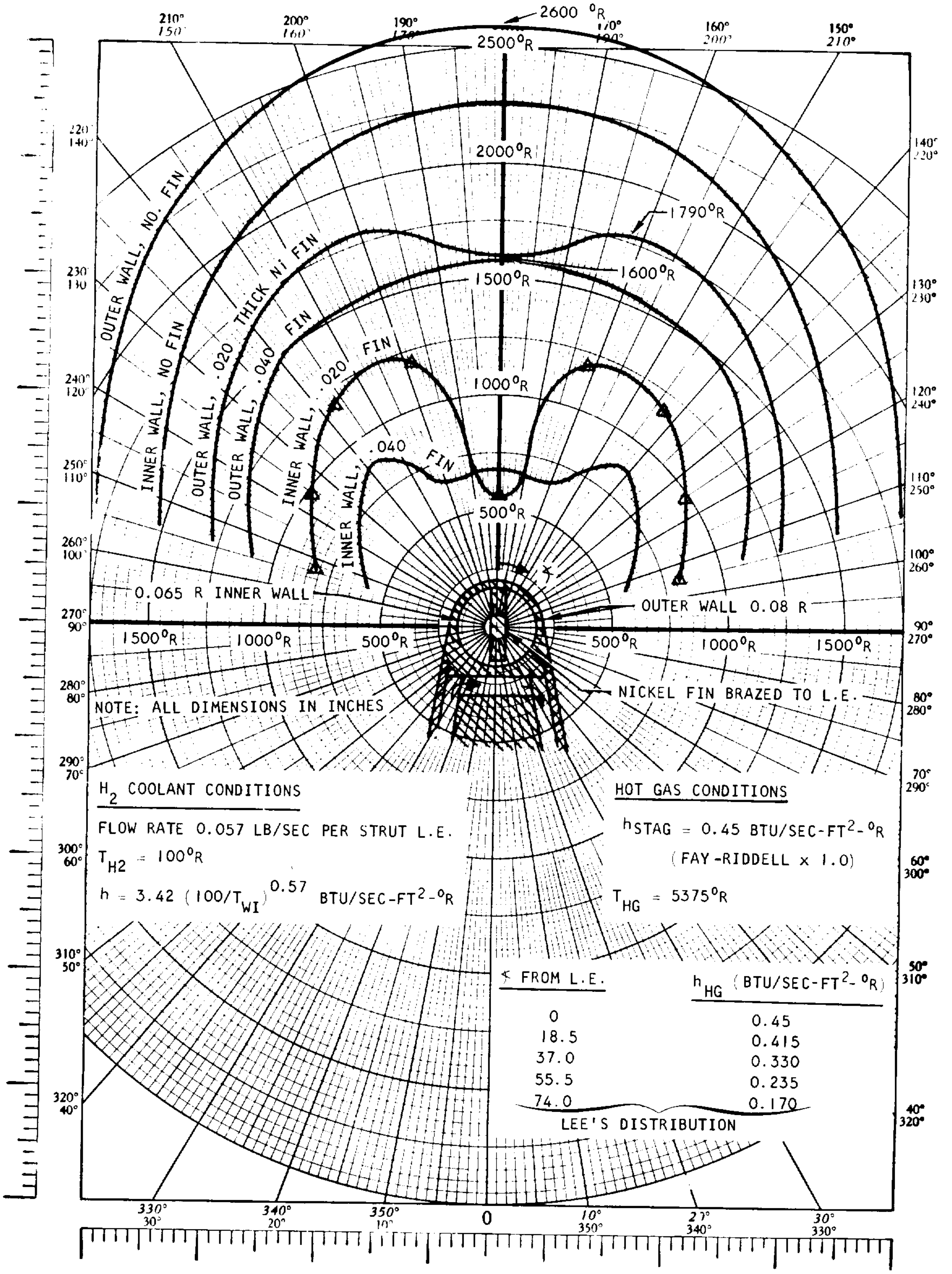

H$_2$ COOLANT CONDITIONS

FLOW RATE 0.057 LB/SEC PER STRUT L.E.

$T_{H2} = 100°R$

$h = 3.42\ (100/T_{WI})^{0.57}$ BTU/SEC-FT^2-°R

HOT GAS CONDITIONS

$h_{STAG} = 0.45$ BTU/SEC-FT^2-°R

(FAY-RIDDELL x 1.0)

$T_{HG} = 5375°R$

∢ FROM L.E.	h_{HG} (BTU/SEC-FT^2-°R)
0	0.45
18.5	0.415
37.0	0.330
55.5	0.235
74.0	0.170

LEE'S DISTRIBUTION

Figure 5.2-1 HRE Strut Leading Edge Temperatures

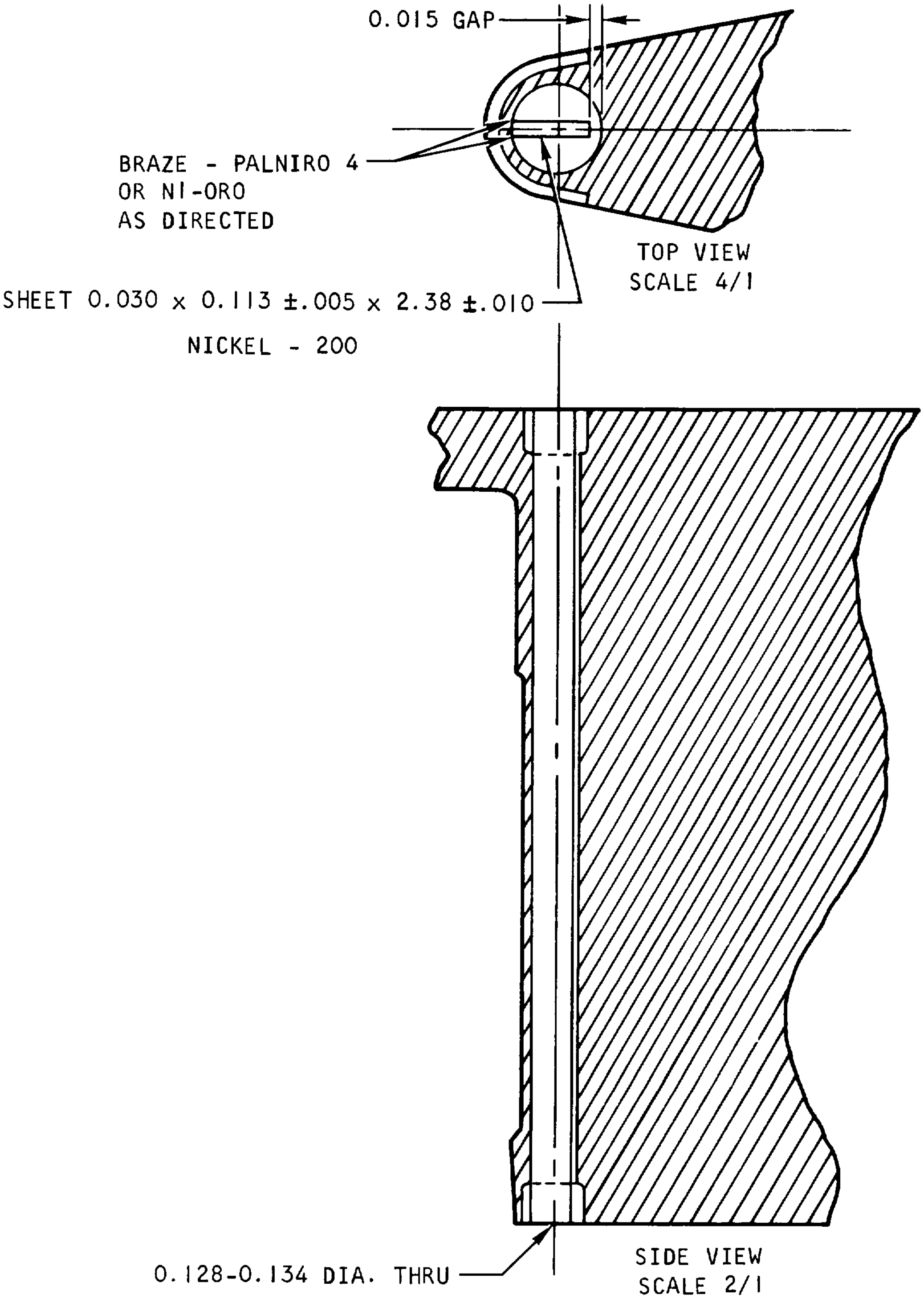
0.015 GAP
BRAZE - PALNIRO 4
OR NI-ORO
AS DIRECTED
TOP VIEW
SCALE 4/1
SHEET 0.030 x 0.113 ±.005 x 2.38 ±.010
NICKEL - 200
0.128-0.134 DIA. THRU
SIDE VIEW
SCALE 2/1

S-48304

Figure 5.2-2 HRE Strut Leading Edge Fin Geometry

wall temperatures result from the low hydrogen heat transfer coefficient (0.58 Btu/sec-ft^2 -^{0}R) predicted from Reference 6. Reference 6 indicates that for heating of hydrogen in plain passages, the heat transfer coefficient evaluated at bulk fluid properties should be divided by the wall-to-coolant temperature ratio raised to the power of 0.57. The hydrogen heat transfer coefficient of 2.5 Btu/sec-ft^2-^{0}R reported in Reference 7 was evaluated at bulk temperature.

To reduce strut leading edge temperature, a nickel fin will be brazed in the coolant passage as shown in Figure 5.2-2. Two dimensional thermal analyses have been performed with 0.020- and 0.040-in.-thick nickel fins. Resulting temperatures for these two cases are shown in Figure 5.2-1. Maximum metal temperatures are reduced to 1790^{0}R for the 0.020-in. fin and 1600^{0}R for the 0.040-in. fin.

Two-dimensional thermal analyses performed on the 0.020- and 0.040-in.-thick fins, using a hot gas stagnation heat transfer coefficient of 0.81 Btu/sec-ft^2-^{0}R (1.8 x 0.45), indicate maximum surface temperatures of 2580^0 and 2260^{0}R respectively. The finned leading edge design offers high local cooling capability at the stagnation line with little increase in coolant pressure drop. In addition, the coolant heat transfer coefficient is increased because free-flow area is reduced, the coolant side wall temperatures are lower and the hydraulic diameter is smaller. A 0.030-in.-thick nickel fin will be used to yield temperature distributions between those for the 0.020- and 0.040-in.-thick fins. The pressure drop for the leading edge with a 0.030-in.-thick fin will be double that for a plain round passage. A pressure drop of 67 psi and outlet Mach number of 0.29 will result for Mach 8 esign point conditions. Both of these values are acceptable.

5.3 LEADING EDGE THERMAL PERFORMANCE

Temperatures in the 15-mil-thick nickel leading edge have been reevaluated. New factors include (1) the coolant hydrogen heat transfer test data reported in Reference 8 for the leading edge straight section with perpendicular flow, and (2) consideration of the wall-to-coolant temperature ratio in the leading edge with parallel flow. The geometry definition for the parallel-flow leading edge straight section was assumed for the full-scale leading edge. Generally, the perpendicular-flow leading edge configuration now appears more attractive than the parallel-flow configuration, contrary to the previous estimate included in Reference 1. The geometries considered in the current work are shown in Figures 5.3-1 and 5.3-2.

5.3.1 Aerodynamic Heating

The aerodynamic heating conditions were previously reported in Reference 1 and are repeated in more detail in Tables 5.3-1, 5.3-2, and 5.3-3. Maximum heat flux at the stagnation line is noted in Figure 5.3-2 and Tables 5.3-1 through 5.3-3. The conditions for the three tables are spike open with and without impingement of the spike shock, and spike closed. All the conditions are associated with the engine in the freestream so that $M_\infty = M_L = 8$ at

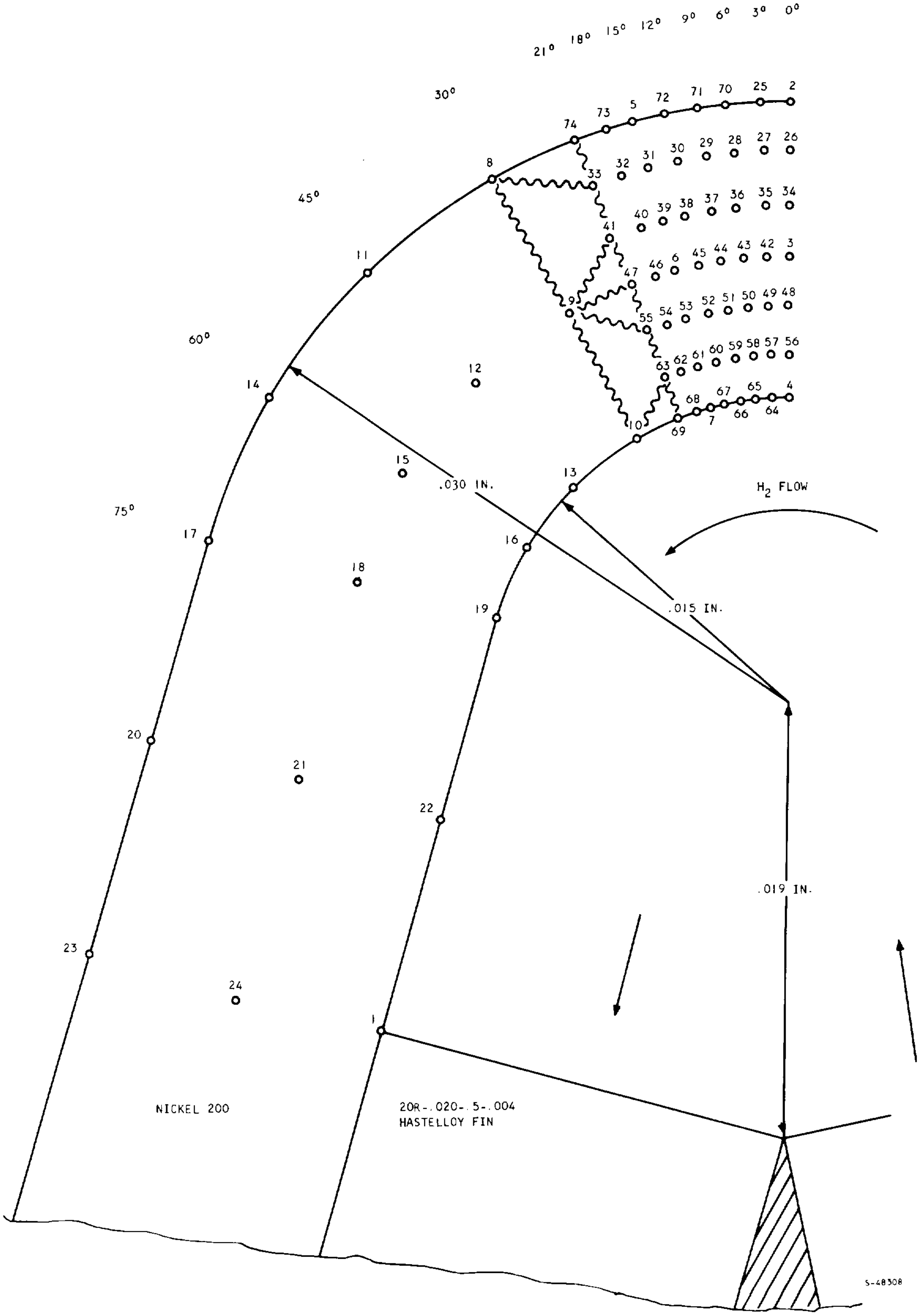

21°
18°
15°
12°
9°
6°
3°
0°
30°
45°
60°
75°
2
25
70
71
72
5
73
74
8
26
27
28
29
30
31
32
33
34
35
36
37
38
39
40
41
3
42
43
44
45
6
46
47
48
49
50
51
52
53
54
55
9
56
57
58
59
60
61
62
63
4
64
65
66
67
7
68
69
10
11
12
13
14
15
16
17
18
19
20
21
22
23
24
1
.030 IN.
.015 IN.
.019 IN.
H_2 FLOW
NICKEL 200
20R-.020-.5-.004
HASTELLOY FIN
S-48308

Figure 5.3-1 Nodes for Perpendicular Flow Leading Edge

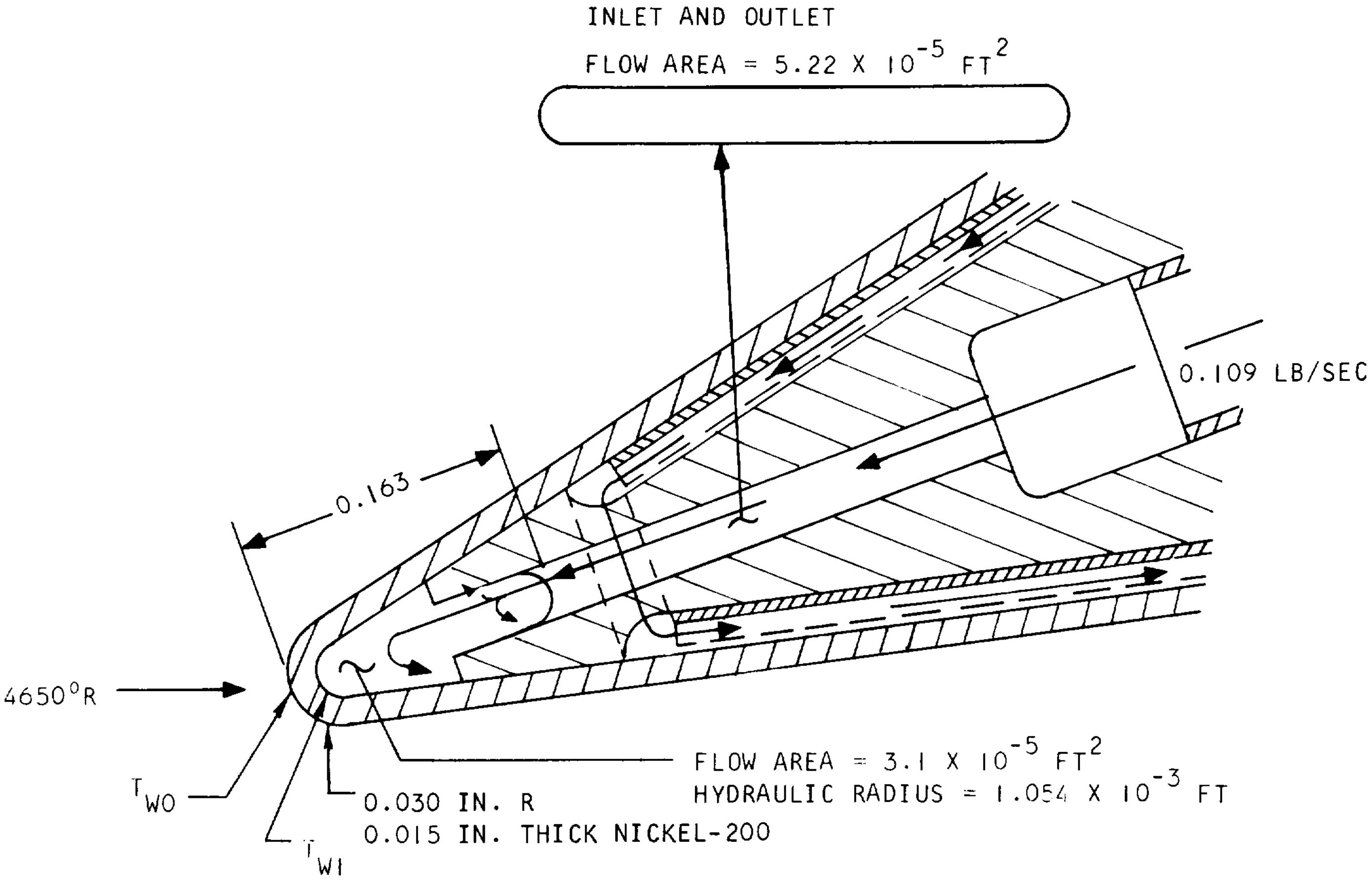
INLET AND OUTLET
FLOW AREA = 5.22 X 10^{-5} FT^2
0.109 LB/SEC
0.163
4650°R
T$_{WO}$
T$_{WI}$
0.030 IN. R
0.015 IN. THICK NICKEL-200
FLOW AREA = 3.1 X 10^{-5} FT^2
HYDRAULIC RADIUS = 1.054 X 10^{-3} FT
S-48179

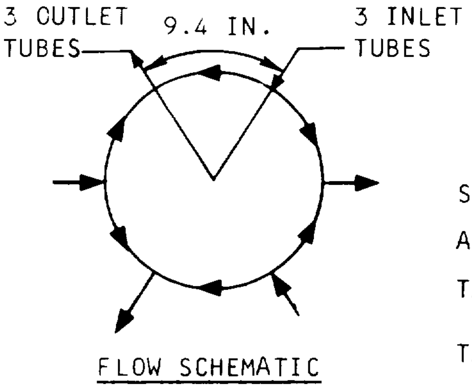
3 OUTLET TUBES
9.4 IN.
3 INLET TUBES
(0.109 LB/SEC, EACH)
FLOW SCHEMATIC

	INLET	OUTLET
STAGNATION q/A, BTU/SEC-FT^2	1750	1900
AVERAGE q/A, BTU/SEC-FT^2	550	560
T_{WO}, °R	1620	1420
T_{WI}, °R	1300	1050
HYDROGEN TEMPERATURE, °R	100	164
HYDROGEN (H), BTU/SEC-°R-FT^2	2.3	3.4

Figure 5.3-2 Parallel Hydrogen Flow Leading Edge at M_L = 8, 88,000-ft Altitude

TABLE 5.3-1

PERPENDICULAR FLOW LEADING EDGE TEMPERATURES WITH SPIKE CLOSED AT M_L = 8, 88,000-FT ALTITUDE

q/A, $\frac{\text{Btu}}{\text{sec ft}^2}$	Node	Temp, ^{0}R	h, $\frac{\text{Btu}}{\text{sec }^0\text{R ft}^2}$	Node	Temp, ^{0}R	h, $\frac{\text{Btu}}{\text{sec }^0\text{R ft}^2}$
	1=	1214.76	0.460	38=	1438.12	
1203	2=	1505.99	0.455	39=	1435.85	
	3=	1407.68		40=	1432.52	
2000	4=	1290.97	2.01	41=	1426.77	
	5=	1499.95	0.432	42=	1407.34	
	6=	1402.53		43=	1406.34	
	7=	1292.79	1.84	44=	1404.78	
	8=	1477.60	0.405	45=	1403.19	
	9=	1394.10		46=	1401.69	
	10=	1297.08	1.63	47=	1400.29	
	11=	1456.81	0.274	48=	1371.86	
	12=	1375.35		49=	1371.34	
	13=	1276.64	1.58	50=	1369.61	
	14=	1420.56	0.330	51=	1366.05	
	15=	1347.07		52=	1359.12	
	16=	1255.43	1.44	53=	1365.52	
	17=	1370.99	0.245	54=	1369.47	
	18=	1311.46		55=	1373.51	
	19=	1231.30	1.31	56=	1337.15	
	20=	1307.86	0.130	57=	1337.51	
	21=	1264.40		58=	1338.68	
	22=	1198.42	1.08	59=	1341.15	
	23=	1292.73	0.115	60=	1345.94	
	24=	1257.60		61=	1338.13	
	25=	1505.71	0.455	62=	1331.96	
	26=	1474.89		63=	1325.34	
	27=	1474.64		64=	1291.25	2.01
	28=	1473.90		65=	1292.05	2.01
	29=	1472.73		66=	1293.30	1.84
	30=	1471.30		67=	1293.86	1.84
	31=	1469.74		68=	1291.97	1.84
	32=	1468.35		69=	1291.25	1.84
	33=	1467.96		70=	1504.84	0.455
	34=	1442.13		71=	1503.27	0.432
	35=	1441.87		72=	1501.69	0.432
	36=	1441.08		73=	1497.88	0.432
	37=	1439.82		74=	1494.95	0.432

Air total temperature = 4200^{0}R
Hydrogen temperature = 300^{0}R
Hydrogen flow = 0.183 lb/sec

TABLE 5.3-2

PERPENDICULAR FLOW LEADING EDGE TEMPERATURES WITH SPIKE OPEN AND NO SPIKE SHOCK IMPINGEMENT AT M_L = 8, 88,000-FT ALTITUDE

q/A, $\frac{Btu}{sec\ ft^2}$	Node	Temp, °R	h, $\frac{Btu}{sec\ {}^{o}R\ ft^2}$	Node	Temp, °R	h, $\frac{Btu}{sec\ {}^{o}R\ ft^2}$
	1=	686.78	1.3	38=	1016.02	
2050	2=	1141.86	0.585	39=	1012.17	
	3=	962.30		40=	1006.35	
3435	4=	774.55	5.3	41=	996.39	
	5=	1131.00	0.562	42=	961.72	
	6=	953.72		43=	960.02	
	7=	775.13	5.1	44=	957.37	
	8=	1089.58	0.518	45=	954.73	
	9=	940.68		46=	952.48	
	10=	781.55	4.7	47=	950.33	
	11=	1054.43	0.475	48=	901.76	
	12=	912.84		49=	900.90	
	13=	756.26	4.4	50=	898.00	
	14=	994.10	0.418	51=	892.09	
	15=	871.15		52=	880.68	
	16=	731.39	4.0	53=	891.32	
	17=	913.55	0.317	54=	897.98	
	18=	819.19		55=	904.91	
	19=	703.36	3.6	56=	845.53	
	20=	817.53	0.173	57=	846.05	
	21=	753.96		58=	847.82	
	22=	666.16	3.0	59=	851.63	
	23=	795.53	0.144	60=	859.19	
	24=	744.82		61=	846.50	
	25=	1141.35	0.585	62=	836.54	
	26=	1083.11		63=	825.95	
	27=	1082.65		64=	774.82	5.3
	28=	1081.31		65=	775.60	5.3
	29=	1079.19		66=	776.71	5.1
	30=	1076.62		67=	777.04	5.1
	31=	1073.86		68=	773.12	5.1
	32=	1071.42		69=	772.58	5.1
	33=	1070.92		70=	1139.79	0.585
	34=	1023.00		71=	1136.94	0.562
	35=	1022.53		72=	1134.11	0.562
	36=	1021.16		73=	1127.29	0.562
	37=	1018.95		74=	1121.91	0.562

Air total temperature = 4650°R
Hydrogen temperature = 156°R
Hydrogen flow = 0.655 lb/sec

TABLE 5.3-3

PERPENDICULAR FLOW LEADING EDGE TEMPERATURES WITH SPIKE OPEN AND SPIKE SHOCK IMPINGEMENT AT M_L = 8, 88,000-FT ALTITUDE

q/A, $\frac{\text{Btu}}{\text{sec ft}^2}$	Node	Temp, °R	h, $\frac{\text{Btu}}{\text{sec °R ft}^2}$	Node	Temp, °R	h, $\frac{\text{Btu}}{\text{sec °R ft}^2}$
4370	1=	657.90	1.3	38=	1076.21	
4370	2=	1287.25	2.19	39=	1068.26	
	3=	1020.92		40=	1058.57	
3470	4=	809.73	5.3	41=	1044.90	
	5=	1192.45	0.562	42=	1019.75	
	6=	1003.21		43=	1016.57	
	7=	808.24	5.1	44=	1011.75	
	8=	1131.68	0.518	45=	1000.63	
	9=	978.15		46=	999.55	
	10=	810.16	4.7	47=	994.98	
	11=	1084.80	0.475	48=	950.22	
	12=	941.41		49=	949.04	
	13=	778.84	4.4	50=	945.15	
	14=	1017.11	0.418	51=	937.65	
	15=	893.34		52=	923.80	
	16=	749.45	4.0	53=	934.00	
	17=	931.76	0.317	54=	939.65	
	18=	837.04		55=	945.41	
	19=	718.03	3.6	56=	887.01	
	20=	832.56	0.173	57=	887.40	
	21=	767.68		58=	889.03	
	22=	677.45	3.0	59=	892.62	
	23=	808.05	0.144	60=	900.16	
	24=	757.27		61=	885.32	
	25=	1250.23	0.585	62=	873.44	
	26=	1178.52		63=	866.32	
	27=	1172.17		64=	809.94	5.3
	28=	1162.72		65=	810.52	5.3
	29=	1152.98		66=	811.29	5.1
	30=	1143.83		67=	811.06	5.1
	31=	1135.49		68=	805.18	5.1
	32=	1128.27		69=	803.03	5.1
	33=	1123.63		70=	1228.74	0.585
	34=	1096.30		71=	1213.44	0.562
	35=	1094.37		72=	1202.01	0.562
	36=	1089.70		73=	1183.65	0.562
	37=	1083.40		74=	1174.12	0.562

Air total temperature = 4650°R
Hydrogen temperature = 156°R
Hydrogen flow = 0.655 lb/sec

88,000 ft (B-B line). The conditions for spike open are with the spike shock outside the leading edge. The conditions for spike shock inside the leading edge are somewhat less severe and were not considered here except to provide the base heat transfer coefficient for the spike shock impinging on the leading edge. The shock impingement heat transfer coefficient is 10 times the value of 0.219 Btu/sec-^{0}R-ft^{2}, as derived from Table 5.5-1 of Reference 1 where heat flux was indicated as 580 Btu/sec-ft^{2} for a 4650^{0}R total temperature and a 2000^{0}R wall temperature. The width of this shock impingement is assumed to be 10 percent of the radius (3 mil). These values are based on the use of the correlating equation suggested in Reference 9.

Experimental results on the effects of shock impingement on a leading edge differing by as much as 500 percent are found in the literature. Edney (Reference 9) and Hiers et al (Reference 10) reported a peak heat transfer coefficient 8 to 10 times higher than the stagnation value when shock impingement occurred. Their tests were conducted at Mach numbers of 4.5 to 14 and for impinging shocks generated by a wedge at angle of attack from zero to 15 deg. Similar effects were reported in Reference 11. However, Bushnell (Reference 12) reports the peak heating due to the leading edge shock impingement was twice the stagnation value without the impinging shock. His tests were conducted at a Mach number of 8 and the impinging shock was generated by a flat plate at an angle of attack of 12 deg. Bushnell explains the flow separation at the root of the leading edge which was attached to the shock generator as the reason for the higher heating reported by Hiers et al. In the test of Reference 12 the leading edge was detached from the shock generator, and there was no boundary layer separation to interfere with the leading edge shock impingement. This explanation, however, cannot clarify Edney's or Teterin's results which show a peak heating of 6 to 8 times higher than the stagnation value in the absence of interference from boundary layer separation. Edney mounted his hemispherical model on a sting while Teterin installed his cylindrical model and the shock generator separately. Until sufficient experimental evidence becomes available to resolve the above discrepancy, Edney's method (Reference 9) is being used for conservatism because higher wall temperatures will be predicted than by use of Reference 12.

Aerodynamic heating with spike closed was calculated as described in Reference 1. Since the leading edge is in the boundary layer at these conditions, boundary layer turbulence may increase the heat flux above the level used by as much as a factor of 2.

5.3.2 Cooling

Hydrogen cooling of the leading edge has been evaluated for the perpendicular-flow configuration of Figure 5.3-1 and the parallel-flow configuration of Figure 5.3-2. The perpendicular-flow configuration is superior on the basis of assumptions currently being made. The major assumptions are:

(a) A wall-to-bulk temperature ratio correction factor is not required for the perpendicular-flow configuration

(b) A wall-to-bulk temperature ratio correction factor is required for the parallel-flow configuration.

In the perpendicular-flow configuration data reported in Section 8.1 of Reference 1, wall-to-bulk coolant temperature ratios varied from 1.26 to 1.91. On the basis of assumption (a) above, and the nickel thermal conductivity evaluated at local temperature, steady-state temperature distribution analysis of the network in Figure 5.3-1 produced the acceptable temperatures in Tables 5.3-1 through 5.3-3. The wall-to-bulk temperature ratio is between 4 and 5 for these analytical results. A wall-to-bulk temperature ratio correction factor is probably not required since the boundary layer profile is not established at the 150-deg turn. The maximum overall difference between Node 2 and the hydrogen temperature is 1206°R, and occurs with the spike closed and the minimum 15-mil wall ΔT of 215°R (Table 5.3-1). The maximum wall ΔT of 478°R occurs for the spike shock impingement conditions (Table 5.3-3). If assumption (a) is not correct, the metal temperatures could rise to values above the acceptable limits.

The spike-closed condition is at a hydrogen flow of 0.183 lb/sec, a forward outer shell outlet temperature of 720°R, and a heat load of 409 Btu/sec. If the stagnation area heat flux is increased above the value used here, due to boundary layer turbulence, the hydrogen flow rate would increase further. The hydrogen flow rate for a 1600°R outlet would be 0.076 lb/sec. The heat load of 277 Btu/sec on the inner surface of the leading edge and forward outer shell was obtained from mission profile analyses reported in Reference 1. The 132 Btu/sec heat load on the outer aerodynamic surface of the leading edge is obtained from Section 5.1 of this report. The hydrogen temperature mismatch at the outer shell outlet manifold and the increased hydrogen demand on the coolant tankage are problems resulting from leading edge flow in excess of that required for an outer shell outlet temperature of 1600°R.

The parallel-flow configuration of Figure 5.3-2 is expected to have a developed boundary layer profile at some distance downstream of each of the three inlet points, and therefore, the wall-to-bulk temperature ratio technique is applicable. Near the inlet where the hydrogen temperature is 100°R and the maximum inner surface temperature is about 1300°R, the wall-to-bulk ratio of 13 reduces the heat transfer coefficient of 2.3 Btu/sec-ft^2-°R evaluated at bulk temperature by a factor of 4.3. Lower hydrogen temperatures will produce larger reductions. The flow rate must be increased by $4.3^{1.25}$ or 6.2 times to 0.0546 lb/sec in each of 6 arcs for a total leading edge flow of 0.327 lb/sec. The total flow for the 6 sections of the parallel leading edge was previously calculated as 0.051 lb/sec. This was only about 19 percent of the total HRE spike closed flow of 0.27 lb/sec and 1.5 percent of the 3 lb/sec maximum pump flow. A flow of 0.327 lb/sec to the leading edge implies more than double the previous total spike-closed flow. Large increases in hydrogen tankage would be required for cooling during ascent and descent unless the leading edge flow were returned to the pump inlet or routed through plate fin surfaces. The heat added is nearly the same for all leading edge flow rates, but the pump power required increases with flow.

The major limit on increasing leading edge flow is choking in the outlet of the tee where the flows from each pair of leading edge segments are combined. The outlet leg of the tee cannot be enlarged enough to avoid choking and stay below an 1100 psia inlet pressure because of space limitations and and the poorly cooled zone expected at the center of the outlet. Using more inlets and outlets alone offers no help because each segment must have the same flow. Decreasing flow and leading edge flow area while maintaining a high hydrogen mass flux transfers the choked location to the leading edge tube. The inlet pressure for acceptable cooling must increase above 1100 psia.

5.4 STRUCTURAL ASSEMBLED MODEL

5.4.1 Aerodynamic Parameters

This section presents the wind tunnel flow path properties for the structural assembled model (SAM). The calculations are based on wind tunnel conditions corresponding to equilibrium expansion to Mach 7.34 of methane vitiated gas ($\phi = 0.8$) having the following stagnation conditions:

Stagnation pressure = 3300 psia

Stagnation temperature = 3600^0R

Stagnation enthalpy = 1095.3 Btu/lb

Stated test section properties include:

$$\text{Mach No.} = 7.34,\ T_o = 376^0\text{R},\ P_o = 0.22\ \text{psia},\ \gamma_o = 1.3818,$$

$$V_o = 7060\ \text{ft/sec},\ \left(\frac{W}{A}\right)_o = 10.835\ \frac{\text{lb}}{\text{sec-ft}^2},\quad W = 28.7\ \text{lb/sec.}$$

Gas (methane combustion products) composition in mole fractions is:

$$A = 0.00839,\ CO_2 = 0.07634,\ H_2O = 0.16538,\ N_2 = 0.71171,$$

$$O_2 = 0.03817,\ \text{mol-wt} = 27.835,\ \phi = 0.8$$

Distribution of the gas properties along the engine surfaces are presented for steady flow. Aft of Station 43, the data presented pertain to both surfaces. Cowl position estimated for shock on lip operation is $X_{CL} = 37.44$ in., yielding an inlet contraction ratio of 9.3. Inlet pressure recovery is estimated to be 0.314.

Figures 5.4-1 and 5.4-2 present gas properties on the spike and outerbody inner surfaces, respectively, to Station 43.0. The data are based on 1/3-scale-model inlet tests. Static and total pressure, static temperature, velocity and and flow area distributions are presented in Figure 5.4-3 for axial stations greater than 43.0 in. on both the outerbody and innerbody to the nozzle end. Figure 5.4-4 presents flow properties along the outerbody external surface where the presence of the pylon has no effect.

5.4.2 Heat Flux Distribution

Heat flux distributions on SAM hydrogen cooled plate-fin surfaces are presented in Figure 5.4-5 for methane combustion products. The aerodynamic data presented in Section 5.4.1 of this report were used. A wall temperature distribution obtained from previous HRE heat transfer analyses was used to obtain heat fluxes in Figure 5.4-5. When wall temperatures for SAM wind tunnel conditions are determined from a hydrogen coolant-side heat transfer analysis, heat fluxes in Figure 5.4-5. When wall temperatures for SAM wind tunnel conditions are determined from a hydrogen coolant-side heat transfer analysis, heat fluxes in Figure 5.4-5 will be modified by less than 10 percent. Eckert's reference enthalpy was used in flat plate aerodynamic heat transfer calculations as outlined on page 5-44 of Reference 1. Hot-gas properties are shown in Figures 5.4-6 through 5.4-8.

The cone-rule modification factor ($3^{0.5}$ for laminar flow and $2^{0.2}$ for turbulent flow) was used on the spike from just aft of the tip to Station XX = 39.4 in. The cone rule was not used on other engine surfaces. A transition Reynolds number (based on surface length from leading edges) of 1×10^7 was used on the spike and 1×10^5 on the inner surface of the outerbody. The resultant transition locations are shown in Figure 5.4-5.

Combustion products gas radiation to cooled surfaces was not considered. A review of hot-gas heating at Mach 8, 88,000-ft flight conditions (Section 5.1) indicated that gas radiation contributed less than 1 percent of the hot-gas heat flux. The average hot-gas static temperature (thermal potential for gas radiation) of hydrogen combustion products for Mach 8 flight was 4300°R. The average hot-gas static temperature of methane combustion products for SAM wind tunnel conditions is 1200°R. In addition, the radiation emissivity for methane combustion products (CO_2 and H_2O) is less than that for hydrogen combustion products of Mach 8 flight (H_2O). First, the static pressure for SAM wind tunnel conditions is less than Mach 8 flight, and second, when carbon dioxide and water vapor are present together the total radiation due to both is somewhat less than the sum of the separate effects because each gas is somewhat opaque to the other.

The aerodynamic heat transfer analyses were performed with a constant hot-gas total enthalpy (1095.3 Btu/lbm) corresponding to a total temperature of 3600°R. Based on a net heat transfer rate to the centerbody and to the inner surface of the outerbody of 2550 Btu/sec and an estimated hot-gas rate through the annular section of the engine of 28.7 $\frac{\text{lb}}{\text{sec}}$, the hot gas total temperature

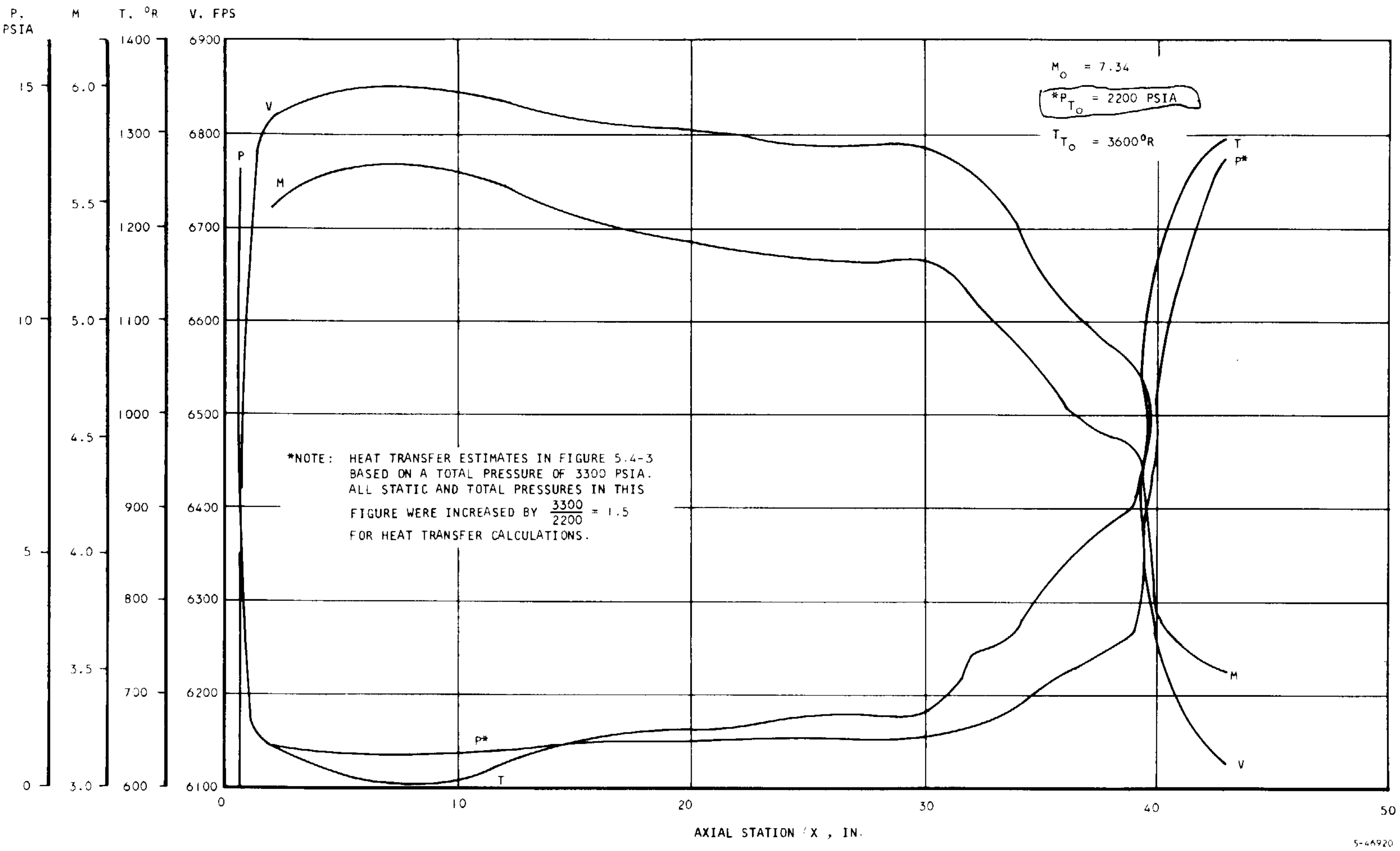

$M_o = 7.34$
$*P_{T_o} = 2200$ PSIA
$T_{T_o} = 3600°R$

*NOTE: HEAT TRANSFER ESTIMATES IN FIGURE 5.4-3 BASED ON A TOTAL PRESSURE OF 3300 PSIA. ALL STATIC AND TOTAL PRESSURES IN THIS FIGURE WERE INCREASED BY $\frac{3300}{2200} = 1.5$ FOR HEAT TRANSFER CALCULATIONS.

Figure 5.4-1 SAM Wind Tunnel Aerodynamic Flow Parameters - Spike to Sta. XX = 43.0

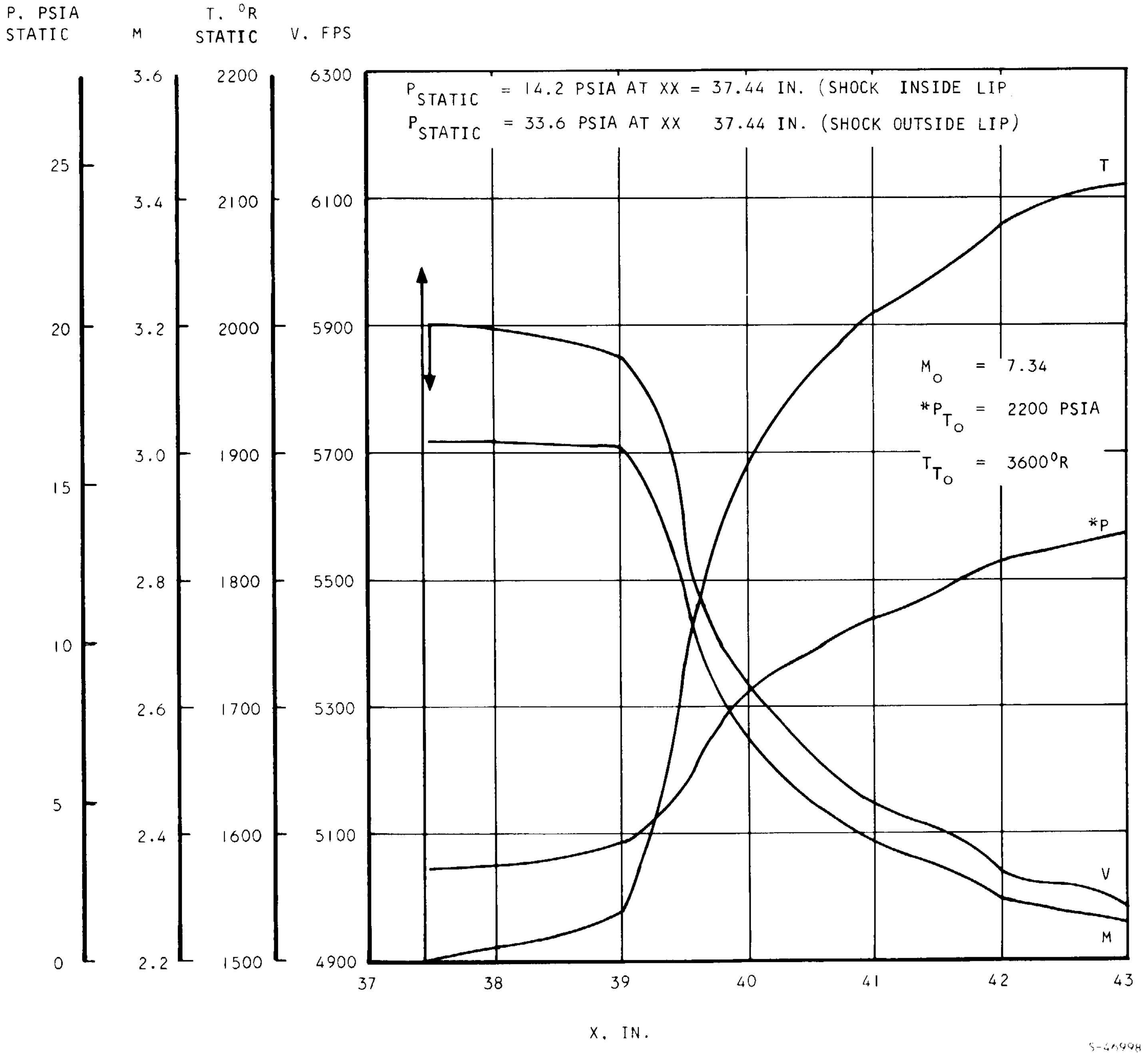

S-46998

Figure 5.4-2 SAM Wind Tunnel Aerodynamic Flow Parameters - Outerbody, Inner Surface, Sta. XX = 37.44 to 43.00

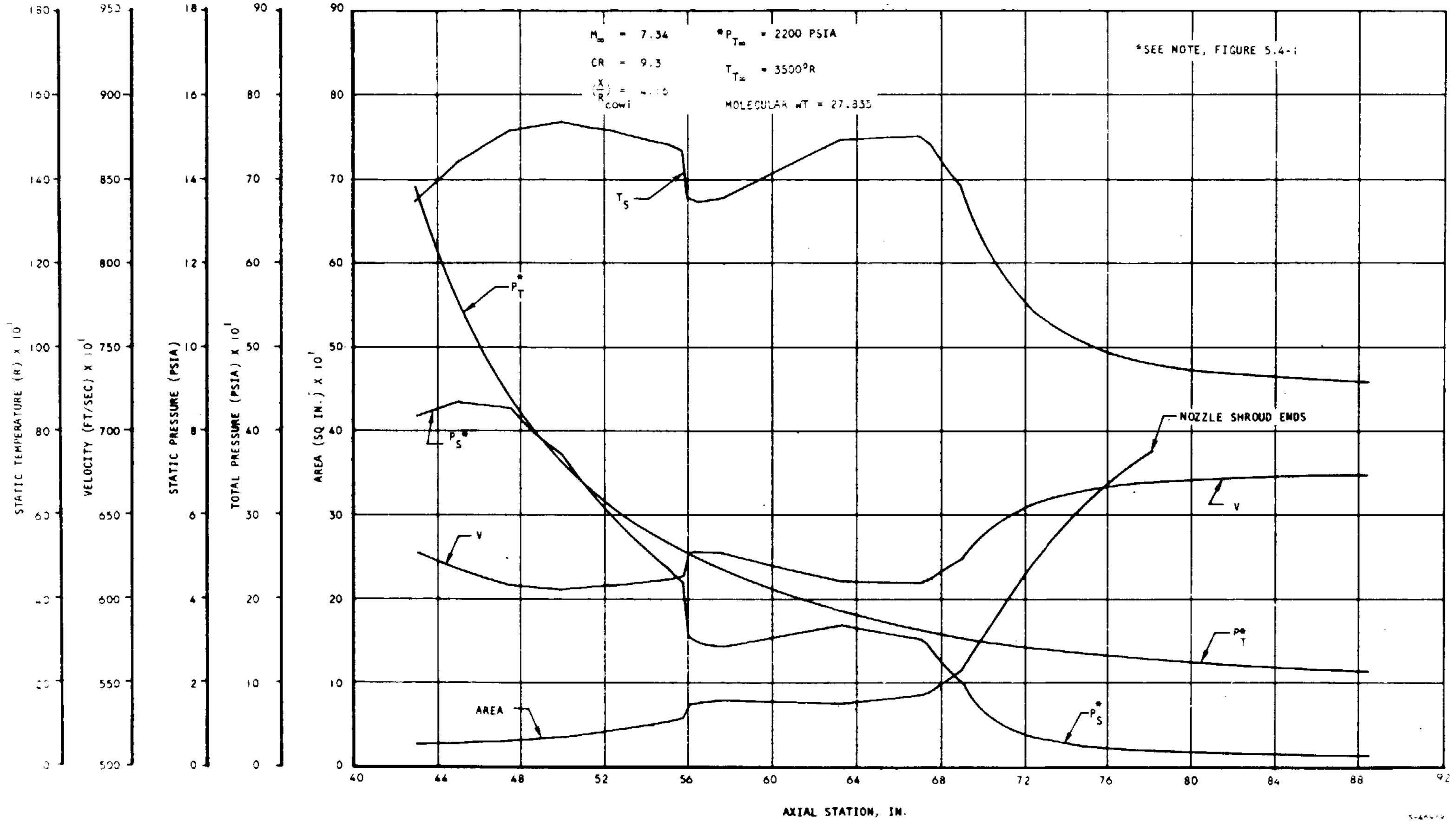

Figure 5.4-3 SAM Wind Tunnel Aerodynamic Flow Parameters - Innerbody and Outerbody from Sta. 43.0

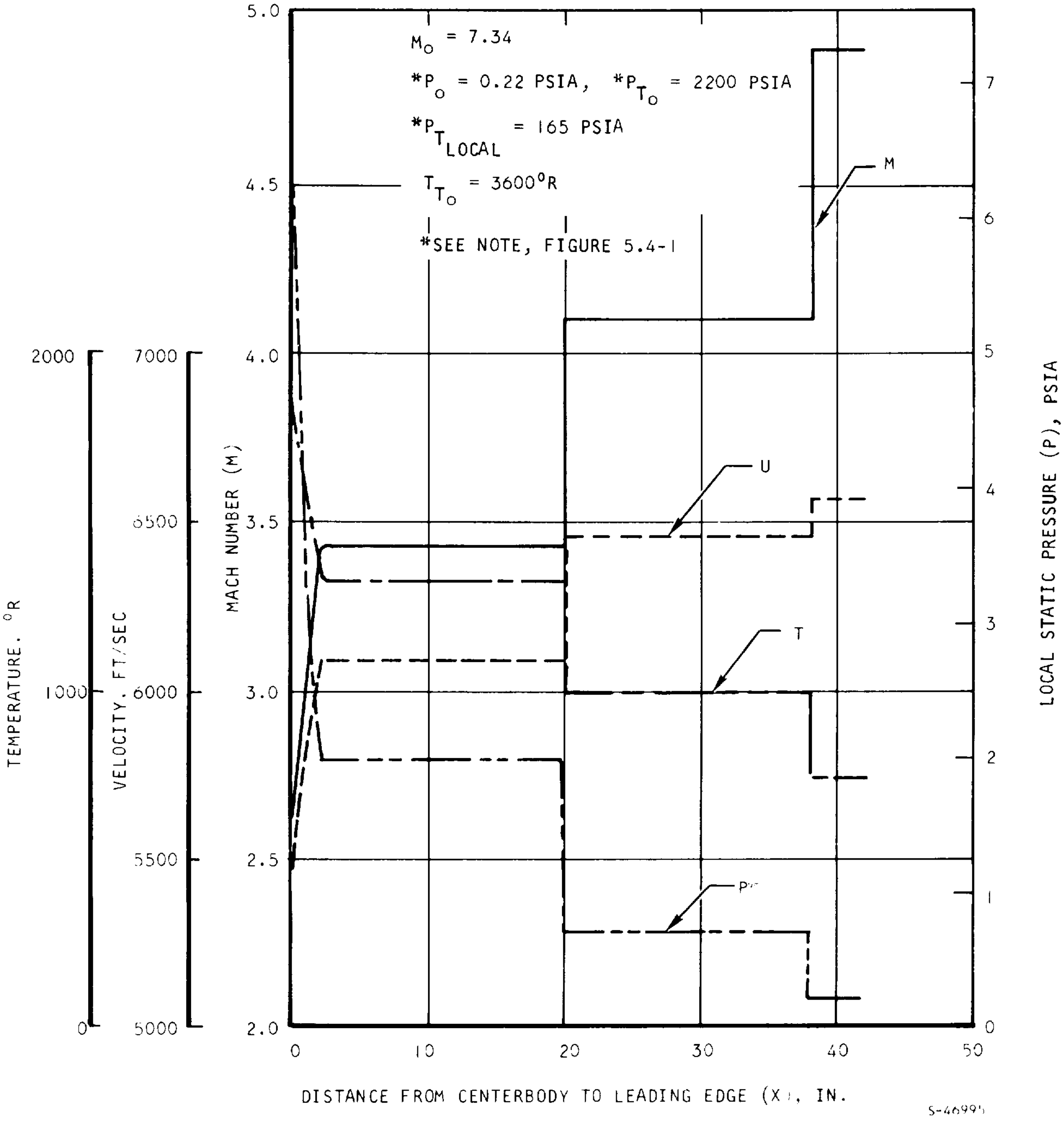

Figure 5.4-4 SAM Wind Tunnel Aerodynamic Flow Parameters - Outerbody, Outer Surface

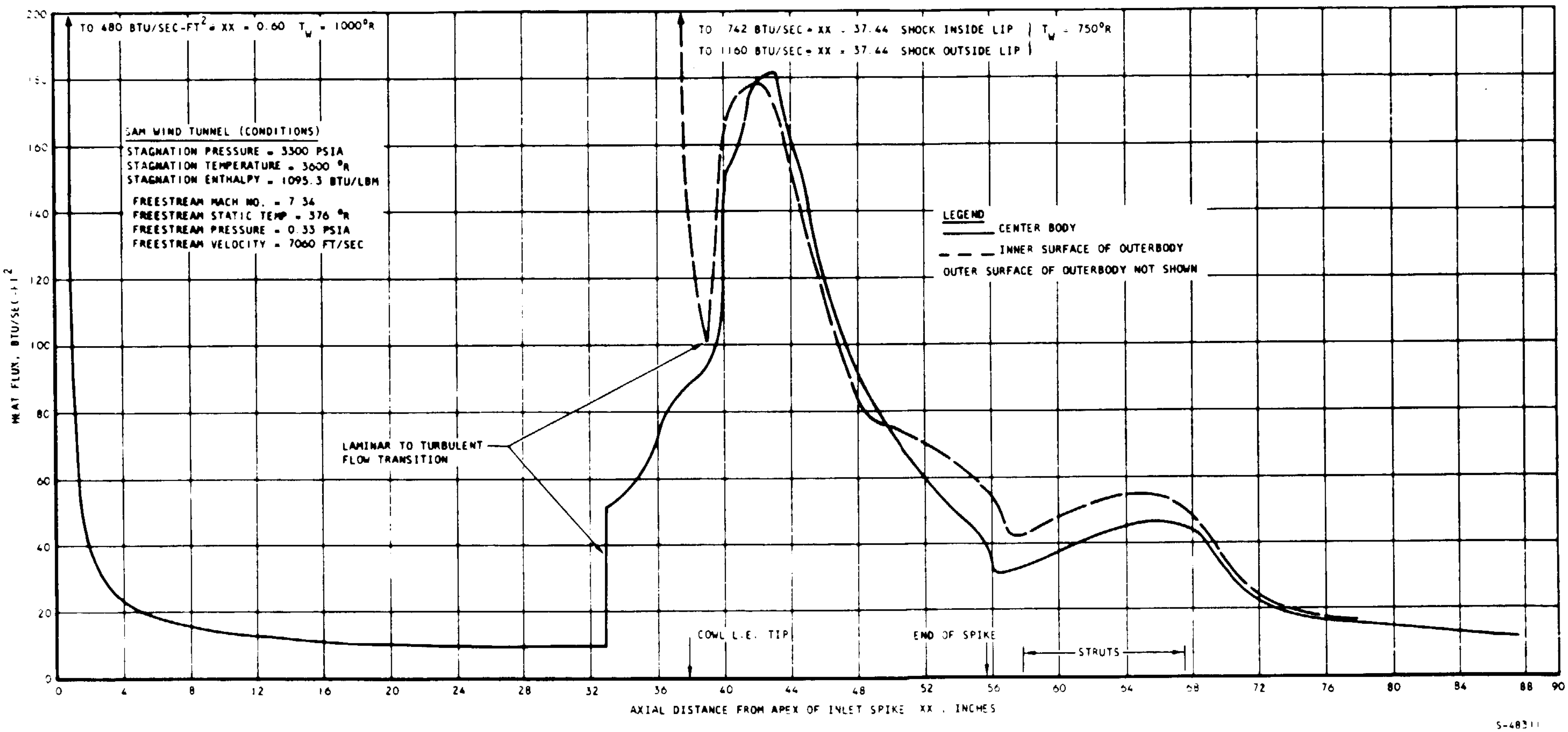

Figure 5.4-5 HRE Predicted Heat Flux Distribution for SAM Wind Tunnel Design Point

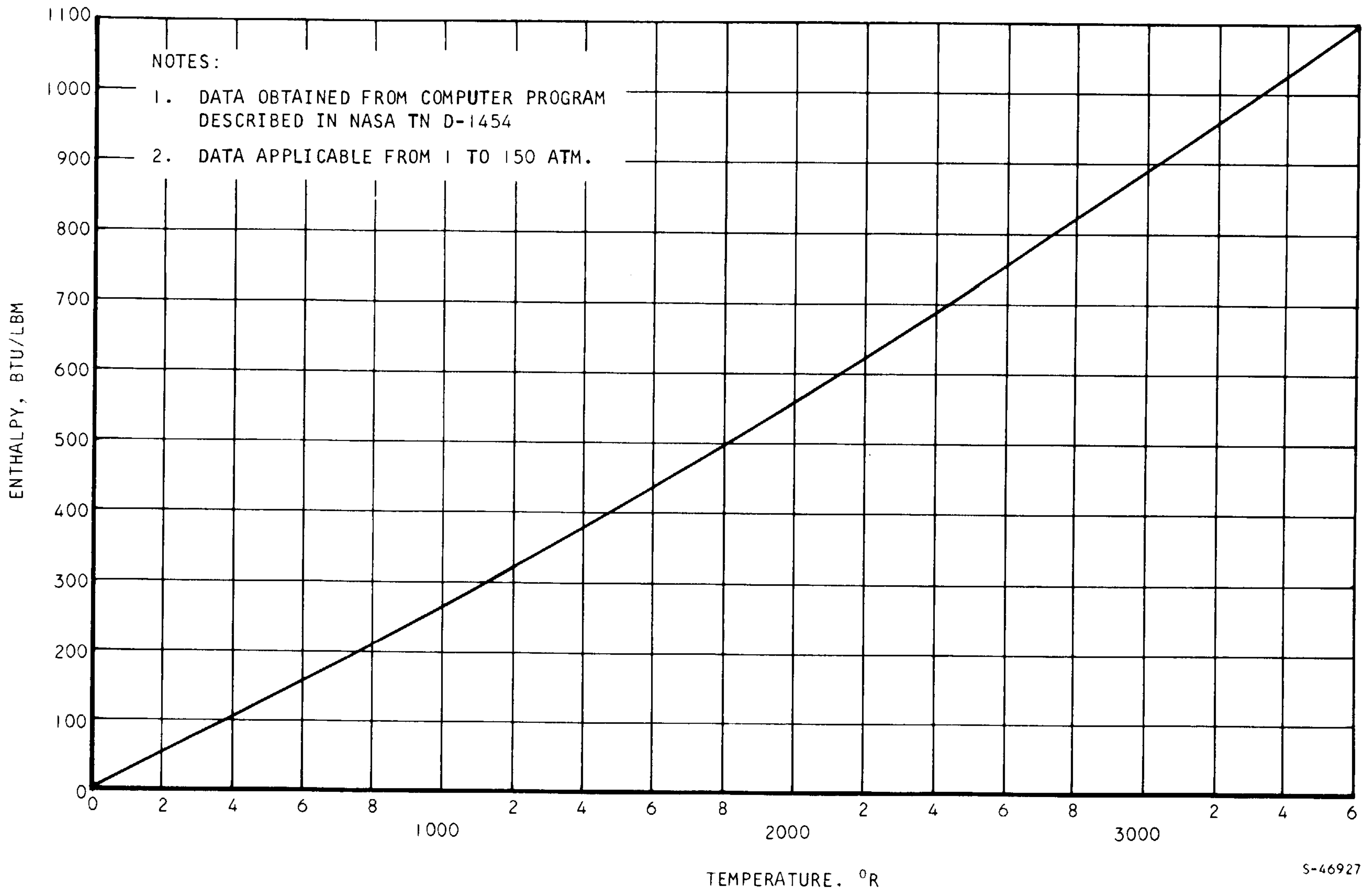

NOTES:

1. DATA OBTAINED FROM COMPUTER PROGRAM DESCRIBED IN NASA TN D-1454
2. DATA APPLICABLE FROM 1 TO 150 ATM.

Figure 5.4-6 Enthalpy of Methane-Vitiated Gas (ϕ = 0.080)

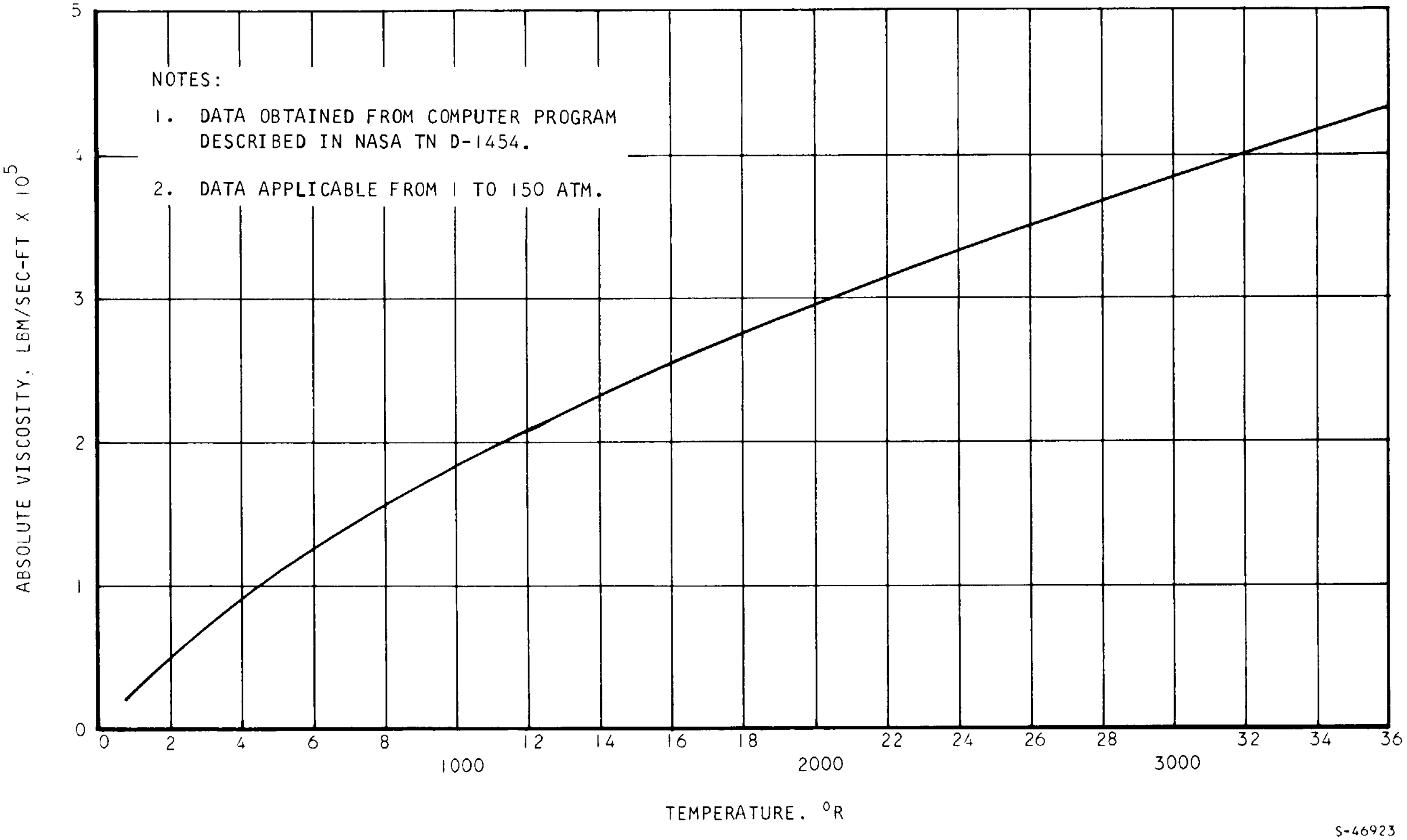

NOTES:

1. DATA OBTAINED FROM COMPUTER PROGRAM DESCRIBED IN NASA TN D-1454.
2. DATA APPLICABLE FROM 1 TO 150 ATM.

S-46923

Figure 5.4-7 Absolute Viscosity of Methane-Vitiated Gas (ϕ = 0.080)

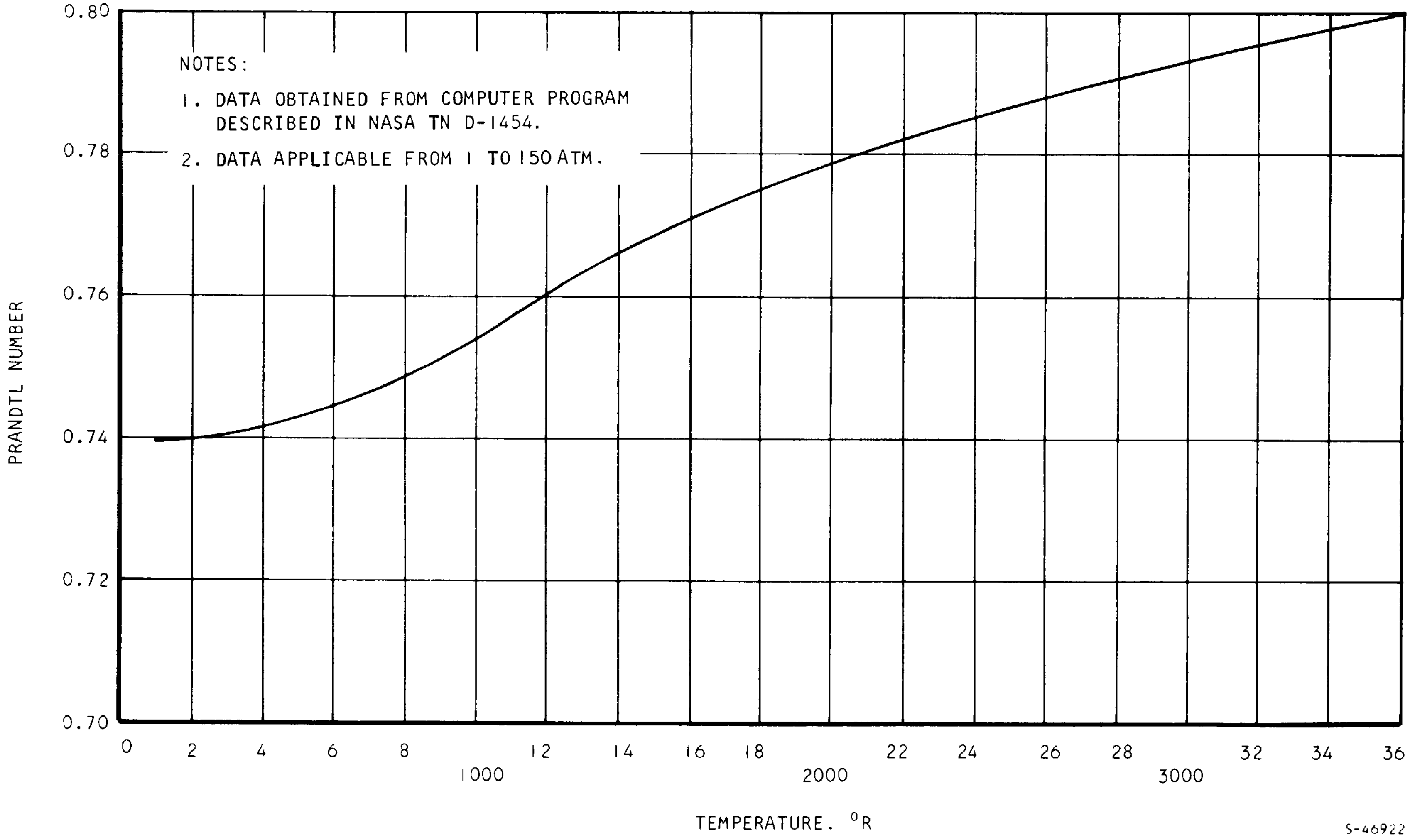

NOTES:

1. DATA OBTAINED FROM COMPUTER PROGRAM DESCRIBED IN NASA TN D-1454.
2. DATA APPLICABLE FROM 1 TO 150 ATM.

Figure 5.4-8 Prandtl Number of Methane-Vitiated Gas (ϕ = 0.080)

6.0 DESIGN EFFORT

All new design activity during the reporting period has been associated with the structural assembled model (SAM). This work has included the following:

(a) Inlet Spike -- A preliminary assembly drawing of the inlet spike, including the necessary equipment and plumbing for installation in the SAM, has been completed. Additional features added to the basic spike include the plumbing and bellows connections for the coolant inlet to the spike tip, the coolant outlet, and the fuel manifold supply. Electrical termination boards for the thermocouples and transducers are provided, as is a heat-sink mounting for the pressure transducers located in the spike. Completion of the drawing is pending final definition of precise transducer envelope specifications.

(b) Inner Shell/Strut/Outer Shell -- Additional features added to the components of this assembly include all of the plumbing required to complete the coolant and fuel circuits as used in the SAM. Completion of work on this assembly is pending definition of instrumentation installations.

(c) Water-Cooled Cowl and Pylon -- Layout and analytical design of this component has been started. This layout will include the cowl itself and approximately one foot of pylon structure. The specifics of adaptation to the wind tunnel will not be part of the layout drawing pending pilot tunnel tests of various configurations.

7.0 MANUFACTURING

7.1 LEADING EDGE STRAIGHT SECTION

7.1.1 Development Effort

Following completion of the three units required on Configuration No. 2 for thermal test program, work was stopped on the SN 6 and SN 7 assemblies. Details and completed assemblies for these units were placed in storage. Processing of the final assemblies was routine, with no special problems and was primarily concerned with attachment of instrumentation.

7.1.2 Status

The assemblies required for the thermal tests (Reference Section 8.1) of the leading edge straight section have all been completed. SN 2 assembly of Configuration No. 1 has been installed in the thermal test facility and is being used for checkout of the test facility.

7.2 STRUT TEST SECTION

Hot gas test results and the analysis based on these results indicate more severe heating at the strut leading edge than originally predicted. Means for limiting the associated increases in metal temperature were evaluated; specifically, an analysis of the effect of a fin brazed to the 0.015-in. hot skin was performed and the results indicated this to be an effective solution. (See Section 5.2.2).

7.2.1 Development Effort

Two thicknesses of Hastelloy X fins were brazed with Palniro 4 and Nioro filler alloys into CRES 304 tubing of the same ID as the strut leading edge to establish the feasibility of brazing a fin into the strut. X-rays were then taken of the braze joint, Figure 7.2-1, showing successful brazing. Metallographic examination also showed good brazing and filleting (Figure 7.2-2).

Tensile specimens with and without braze alloy (Palniro 4 and Nioro) were placed in the furnace during the brazing cycle. The tensile properties of these samples were compared with the "as received" Hastelloy X material. The reduction in tensile properties was similar to that previously reported.

A Nickel-200 fin was successfully brazed into the leading edge coolant circuit of the SK 51303-1, SN 4 strut assembly (previously scrapped). This brazing cycle was run to define the brazing techniques prior to any rework on a strut assembly scheduled for hot gas testing.

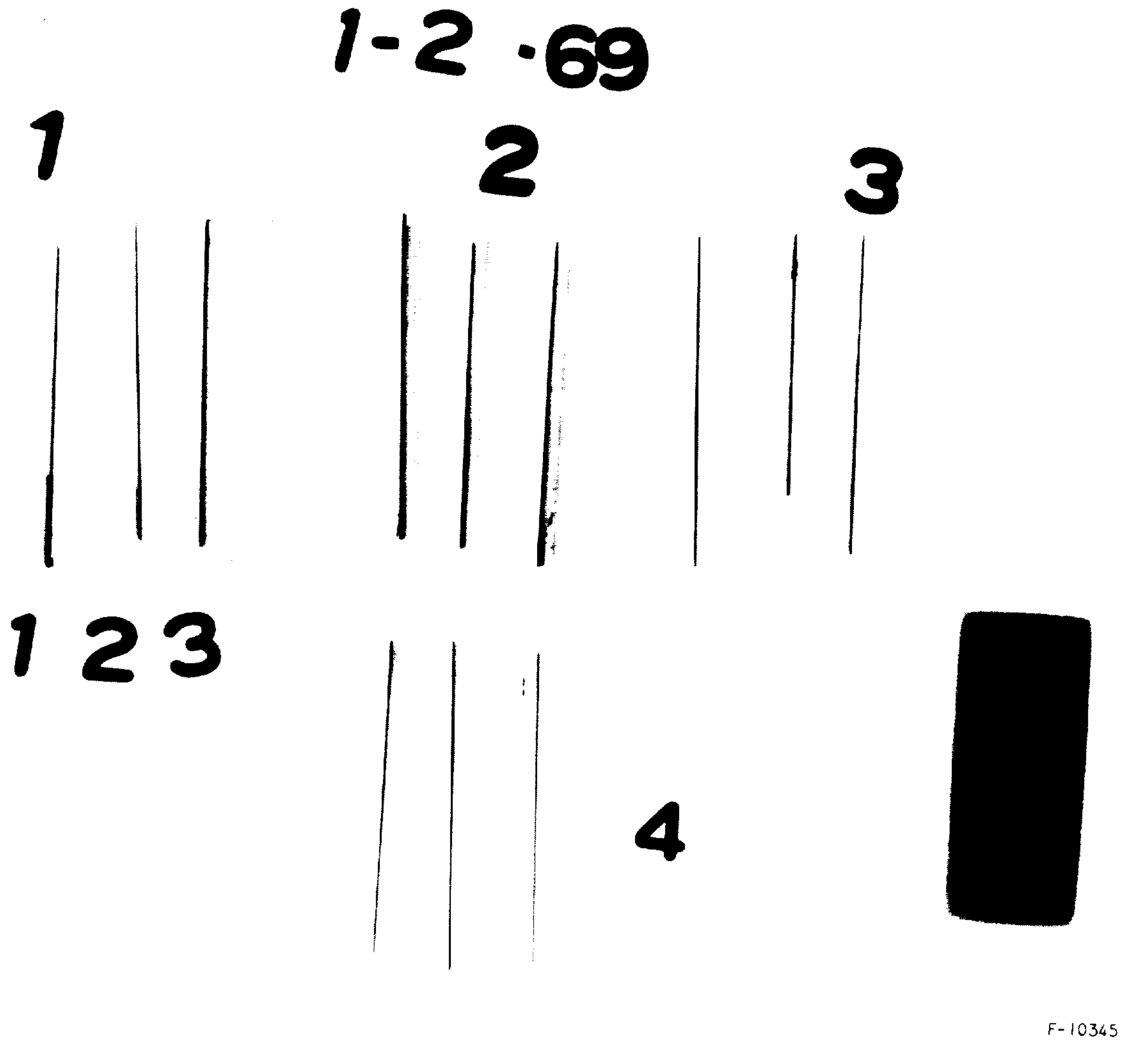

Figure 7.2-1 Strut Leading Edge Fin Evaluation - X-Rays of Braze Joint (Dark Area) Between Fin and CRES 304 Tubing

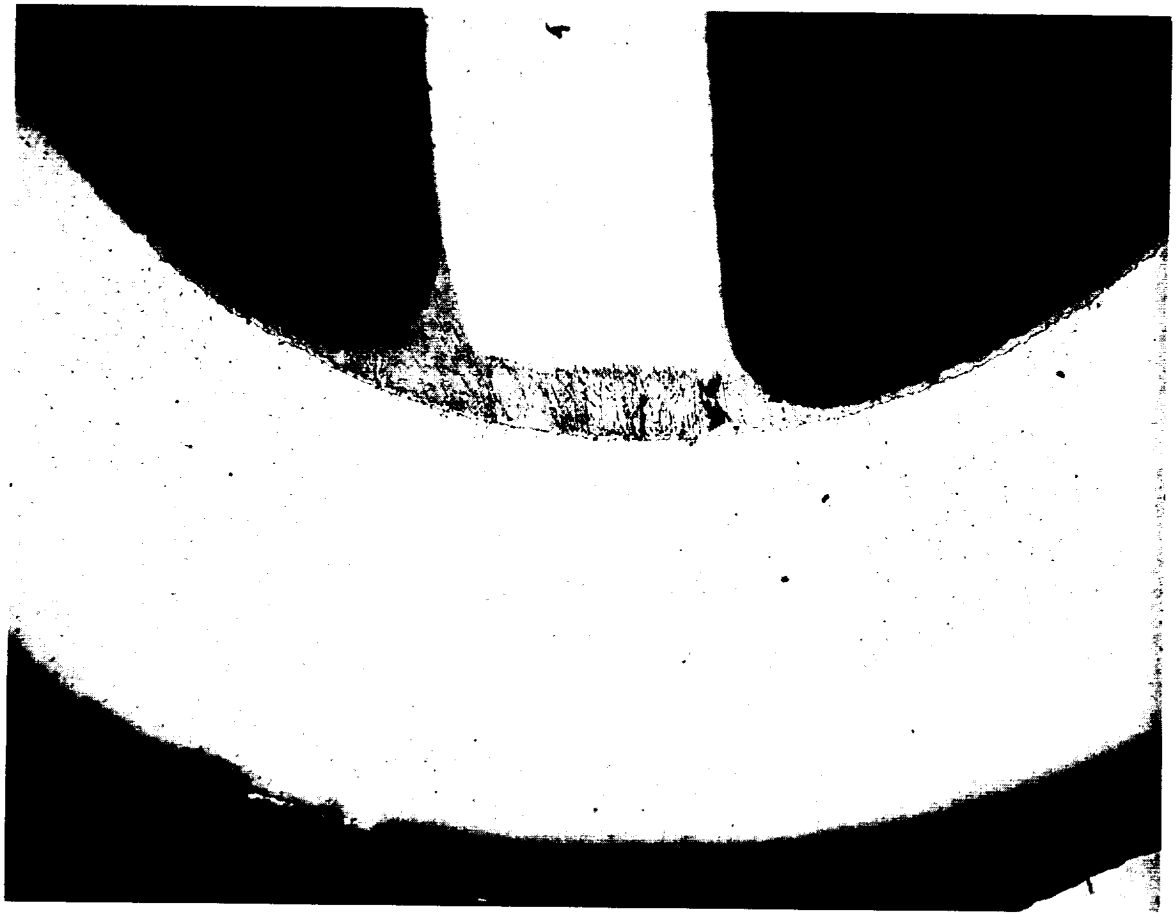

F-10347

Figure 7.2-2 Strut Leading Edge Fin Evaluation - Metallographic Examination Showing Filleting of Braze Alloy at Fin-to-Skin Joint

7.3 INNERBODY (INNER SHELL)

7.3.1 Development Effort

Difficulty was experienced in sealing the forward end of the strut mounting flange to the shelf assembly on the first static test unit. This problem occurred because a new cooling slot was added around the strut housing to improve flow distribution. This reduced the amount of surface area for braze-sealing. A design change, in which a shim was brazed in the regions where the leaks occurred, was released for the SAM unit.

Leakage was also experienced during pressure test of this unit at one end of the actuator pad gussets where they were brazed into the strut housing. To alleviate this leakage problem, a design change was released for the SAM unit which tightened the lengthwise tolerance between the gusset and the strut housing so a braze-seal can be attained. Originally, no braze-seal was required at this point, but because this unit has the new cooling slot, the gusset fitting is required to seal.

The aforementioned leakages on the first static unit have been repaired with an additional furnace braze cycle using Nioro 82-18 alloy and TIG brazing as required, using this alloy.

7.3.2 Status

The first static test unit is in process of final machining of the seal surfaces at the aft (nozzle) end.

The SAM assembly, which had its initial skin/fin braze cycle, showed excellent braze quality, as evidenced by the pressure test with StressCoat. The pressure test after the inserts were installed was also satisfactory. The unit is now having these inserts ground flush to the skin surface, prior to manifold installation.

7.4 INNERBODY (NOZZLE)

7.4.1 Development Effort

The experimental nozzle assembly was pressure tested with air at 950 psig using the metallic seals selected for the application. Leaks occurred at three of the four Harrison K-seal joints at the aft end of the nozzle; four of the seven K-seals used at the forward end of the nozzle leaked. Two pocket seals at the forward end used the alternate seal design, the Omniseal, and sealed satisfactorily. The reason the K-seals did not seal is believed to be due to the difficulty of attaining the high degree of surface finish required in the machining operations that characterize the design of these seals. Because of this difficulty, a design change has been made to use Omniseals on all nozzle seal joints. Detail thermal analyses have shown that maximum seal surface temperatures will be 200°F at design conditions; i.e., compatible with the Teflon materials of the seals.

The skin/fin assembly assigned to the first static test unit passed the proof-pressure test at 1050 psig. The test pressure was not carried beyond 1050 psig because of StressCoat flaking at the large diameter end (see Figure 7.4-1). This area of StressCoat flaking is trimmed off prior to final assembly. Since no other indication of StressCoat cracking was noted anywhere else on the surfaces, this unit is considered satisfactory for all testing.

The skin/fin assembly designated for the structural assembled model (SAM), satisfactorily passed the proof-pressure test at 1300 psig. The pressure test was stopped at 1300 psig because of StressCoat cracking noted at the large diameter end and at the small diameter end where the test fixture attaches. This condition is similar to that observed on the assembly for the static test unit and the same comments apply.

7.4.2 Status

(a) The experimental test unit will have new seals installed and then receive its final pressure test.

(b) The static test unit is presently undergoing final machining of the seal surfaces at the two ends.

(c) The manifold for the SAM unit is being final-machined for assembly prior to brazing.

(d) A skin/fin shell assembly without manifolds has been completed and is being creep-rupture tested.

7.5 INLET SPIKE

7.5.1 Development Effort

The SN 1 aft spike shell assembly, which was unusable for use in a spike assembly because of carbon contamination of the hot shell in brazing, was repaired by the use of patches and doublers. Palniro 7 and Nioro braze alloys were used to accomplish the repair. Induction brazing, as a repair technique, was evaluated as part of this effort.

The sealed unit was subjected to a 2200 psig StressCoat test, followed by a hydrostatic burst test. Rupture during the burst test occurred at 3160 psig at the doubler location (Figure 7.5-1) as predicted during the StressCoat test. This result is satisfactory, in light of the extensiveness of the repair operations and the contamination in the repaired areas, and would be acceptable in surface areas operating at low temperature. The test also showed StressCoat to give a meaningful indication of the quality of the repair.

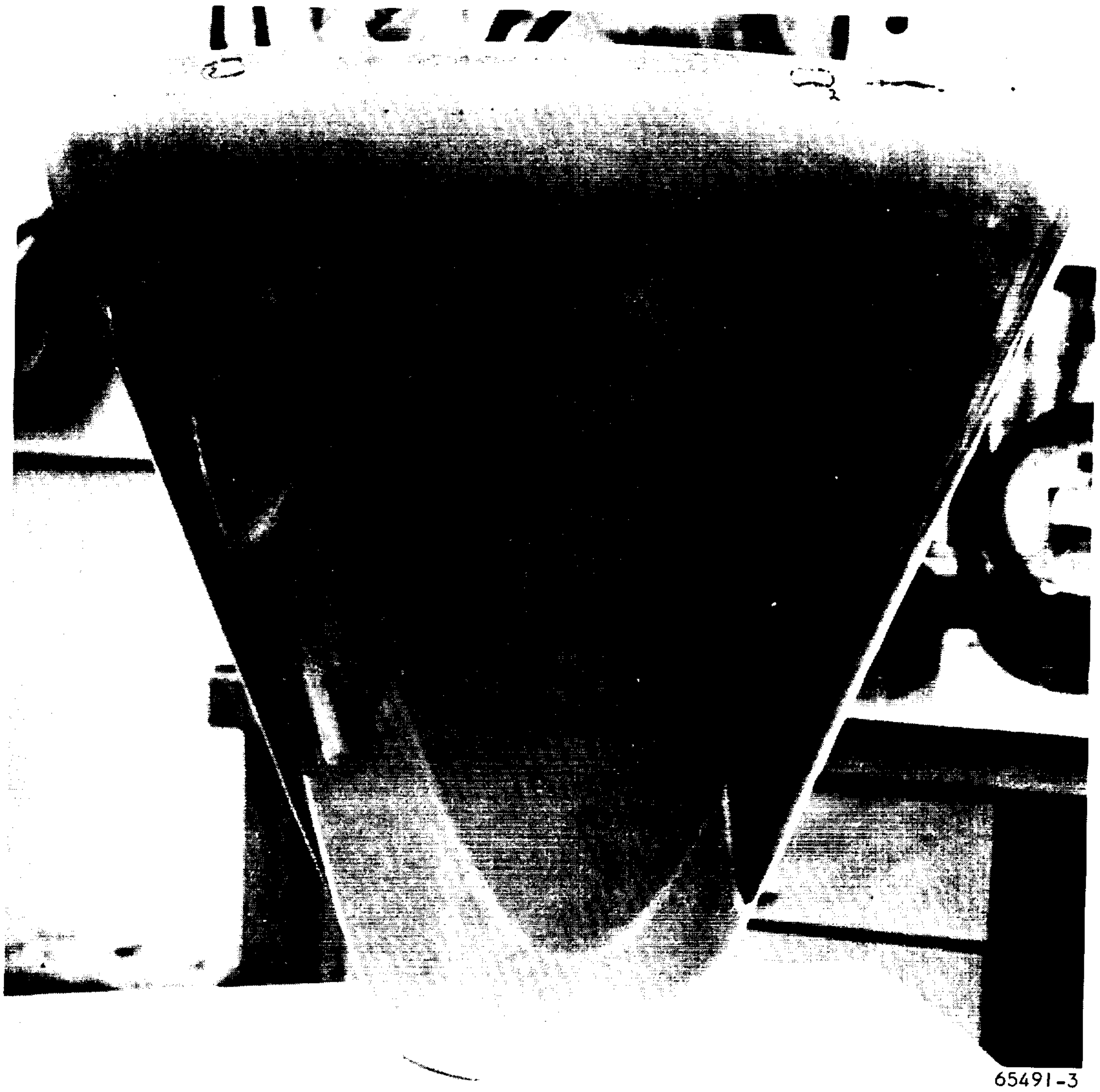

Figure 7.4-1 SN 5 Nozzle After StressCoat and 1050 psig Proof Pressure Test

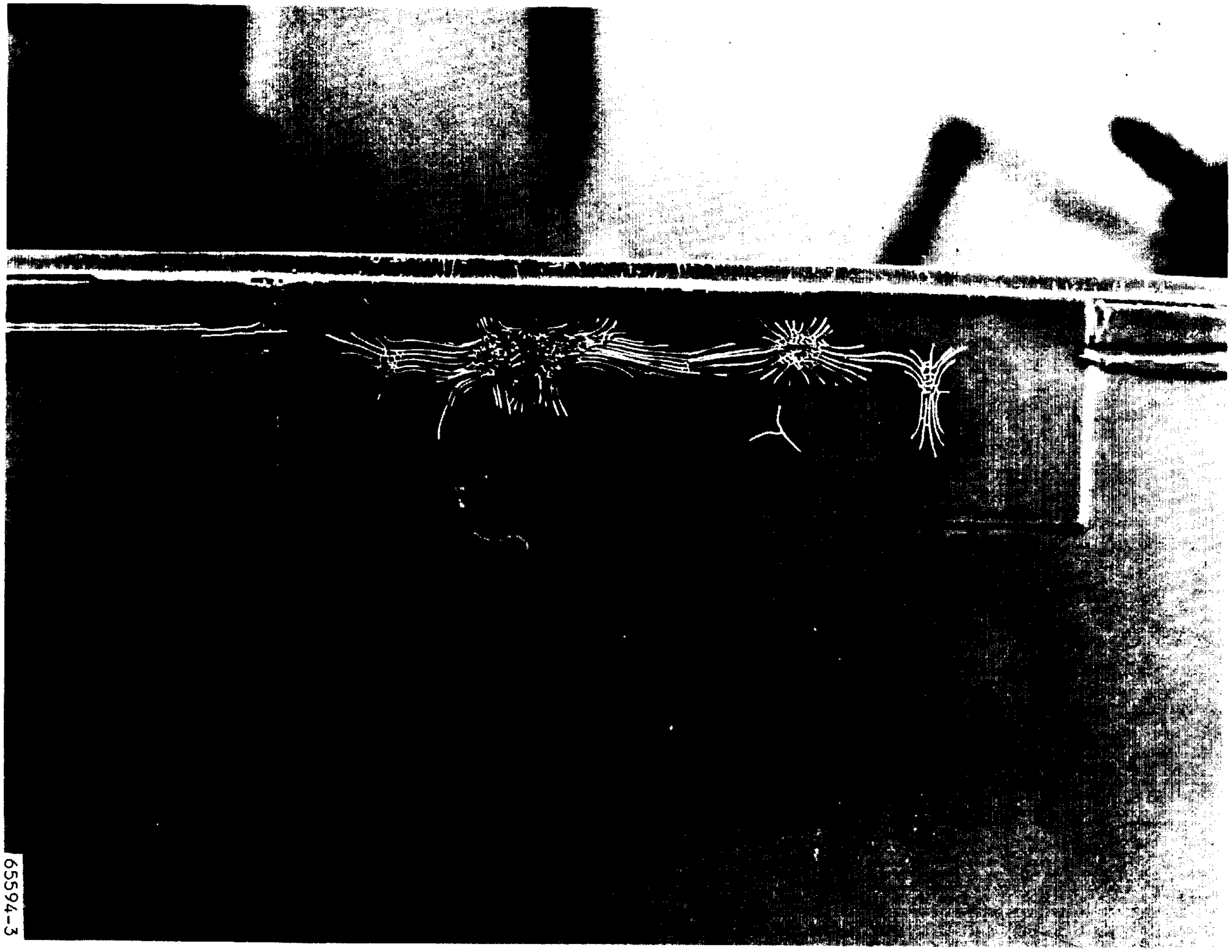

Figure 7.5-1 Aft Spike Shell Assembly After 2200 psig StressCoat Pressure Test

7.5.2 Status

7.5.2.1 Experimental Spike Assembly

The repair of the doubler and injector voids on the experimental spike assembly was delayed pending the test results on the use of induction heating on the SN 1 aft spike shell assembly. This procedure was then used to successfully seal the voids. The experimental spike will be subjected to a 1050 psig StressCoat proof-pressure test prior to flow distribution and pressure drop testing.

7.5.2.2 Static Spike Assembly

The fore spike and spike tip assembly have been brazed together. The aft spike assembly is being reworked to repair the hot-skin-to-header braze joint at the aft end of the assembly before being joined to the forward spike sections.

7.5.2.3 SAM Spike Assembly

The fore spike and spike tip assemblies are ready for the next braze cycle which joins the two assemblies together. The aft spike shell assembly has completed the second braze cycle for the installation of the fuel injector inserts. On the next braze cycle, the manifolds, actuator mount, and the fore-to-aft spike doublers are brazed onto the aft spike shell assembly, to complete the aft spike assembly.

7.6 LEADING EDGE

7.6.1 Development Effort

Fabrication of details has continued and is completed except for match machining operations to fit shell and manifold assemblies. Additional inner and outer shell assemblies and the first tip assembly have been assembled and brazed. Manifolds and instrumentation have been fitted and brazed to inner and outer shell assemblies to make up the inlet manifold assembly (outer shell) and the outlet manifold assembly (inner shell).

Fitup and assembly of the first structural assembly have been completed and the assembly is ready for brazing.

7.6.1.1 Inner Shell Assembly (Figure 7.6-1)

All work has been completed on the two assemblies that were brazed during the last reporting period. X-ray inspection, StressCoat pressure test and proof-pressure test showed no indications of any structural defects in these assemblies.

The third unit assembled and brazed during the period was rejected and scrapped after braze due to a nonrepairable bulge in the inner (hot) skin. The bulged area, approximately 1/2 in. wide by 0.040 in. high, extended axially for the full length of the shell and was not detectable

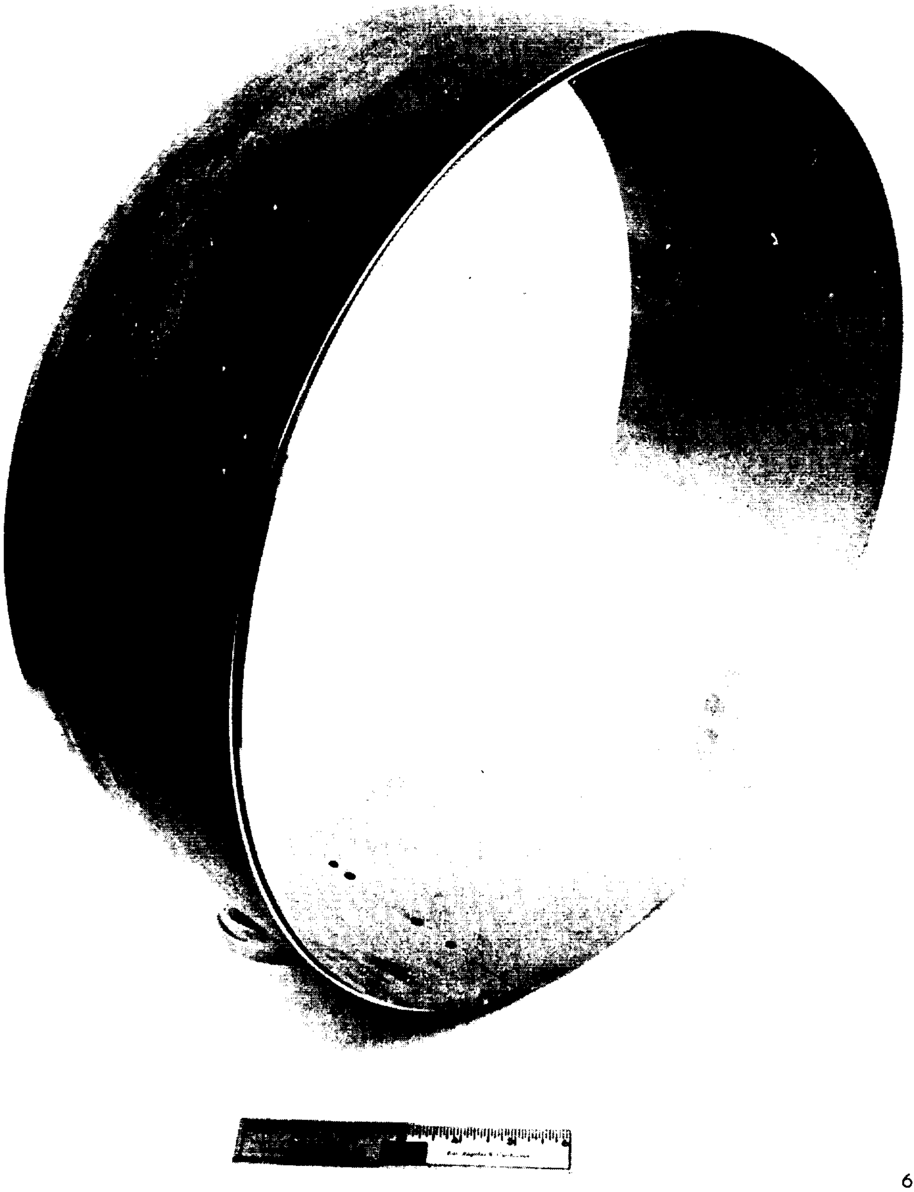

64967-1

Figure 7.6-1 Inner Shell Assembly

until the shell assembly had been cut from the braze fixture insert. Details for a replacement assembly have been completed, assembled, and are ready for brazing.

7.6.1.2 Outer Shell Assembly (Figure 7.6-2)

Three assemblies have been completed, two of which were brazed during this period. During the braze cycle on the last assembly, loading pressure could not be held, and it dropped off from 20 psig to 3 psig. Inspection of the assembly after brazing showed the part to be undersize by 0.040-in. dia. at different stations. Loss of pressure during the braze cycle was due to a small crack in the weld joint between the fixture insert and the inner (cold) shell.

The leak was repaired and the assembly recycled in the brazing furnace to resize the assembly. No difficulties were experienced during the recycle, and inspection after brazing showed the part to be within acceptable dimensions. All operations including dimensional inspection, X-ray inspection, and StressCoat and proof-pressure tests have been completed on these assemblies.

7.6.1.3 Tip Assembly (Figure 7.6-3)

The first tip assembly has been brazed, but was found to be undersize in diameter. With the undersize condition, the braze tip assembly cannot be trimmed to correctly match the mating structural shell assembly. Tooling is in work to resize the tip assembly by cold stretch-forming, since the braze fixturing cannot be adapted to resize the part at braze tempeatures.

To correct the size discrepancy, the braze fixture and the brazing cycle procedure have been modified for the second tip assembly, which has been fitted and assembled and is ready for braze.

Details for a third assembly are complete but are being held for assembly and braze, pending results of the second unit.

7.6.1.4 Inlet and Outlet Manifold Assemblies

Two each of the inlet and outlet manifold assemblies have been completed. Leaks at instrumentation insert-to-shell joints, and manifold-to-shell joints were found after the assemblies were brazed. These were repaired by cleaning and realloying the leak areas, then brazing. Palniro I braze alloy was used for the initial braze cycle, but repairs were made with Palniro RE alloy which has a slightly lower brazing range than the Palniro I, but a higher range than the Palniro 7 to be used in the next assembly operation. The inlet manifold assembled for brazing is shown in Figure 7.6-4.

7.6.1.5 Structural Assembly

This assembly consists of the inlet manifold assembly, outlet manifold assembly, a ring joining the manifold assemblies at the forward end, and a segmented structural support ring.

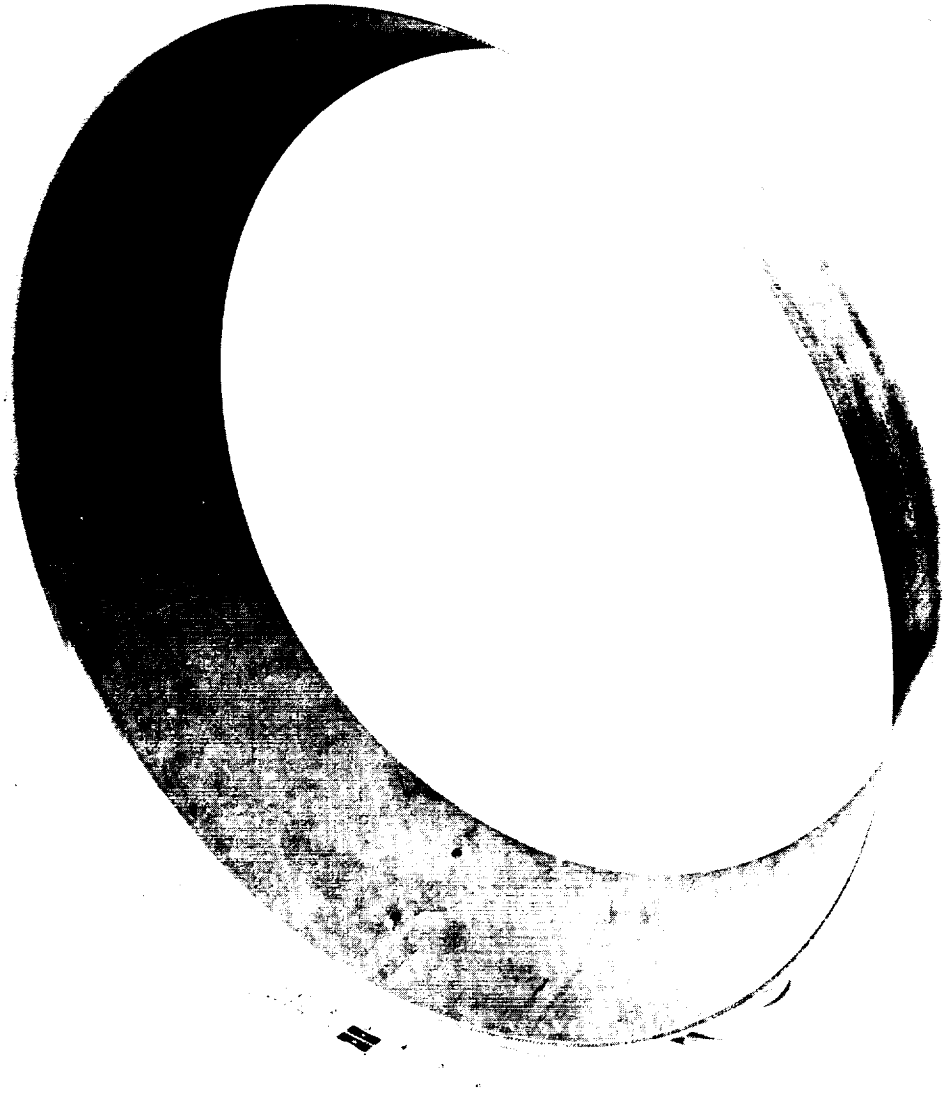

64967-9

Figure 7.6-2 Outer Shell Assembly

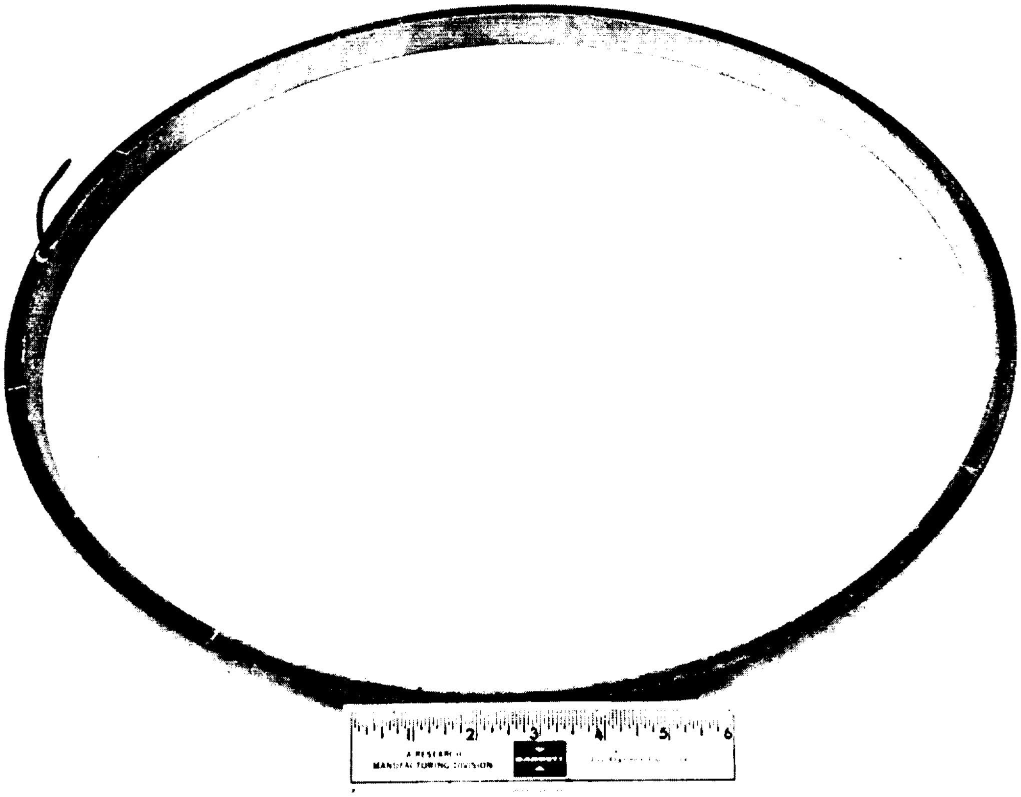
1
2
3
4
5
6
AIRESEARCH MANUFACTURING DIVISION
GARRETT

65724-2

Figure 7.6-3 Tip Assembly

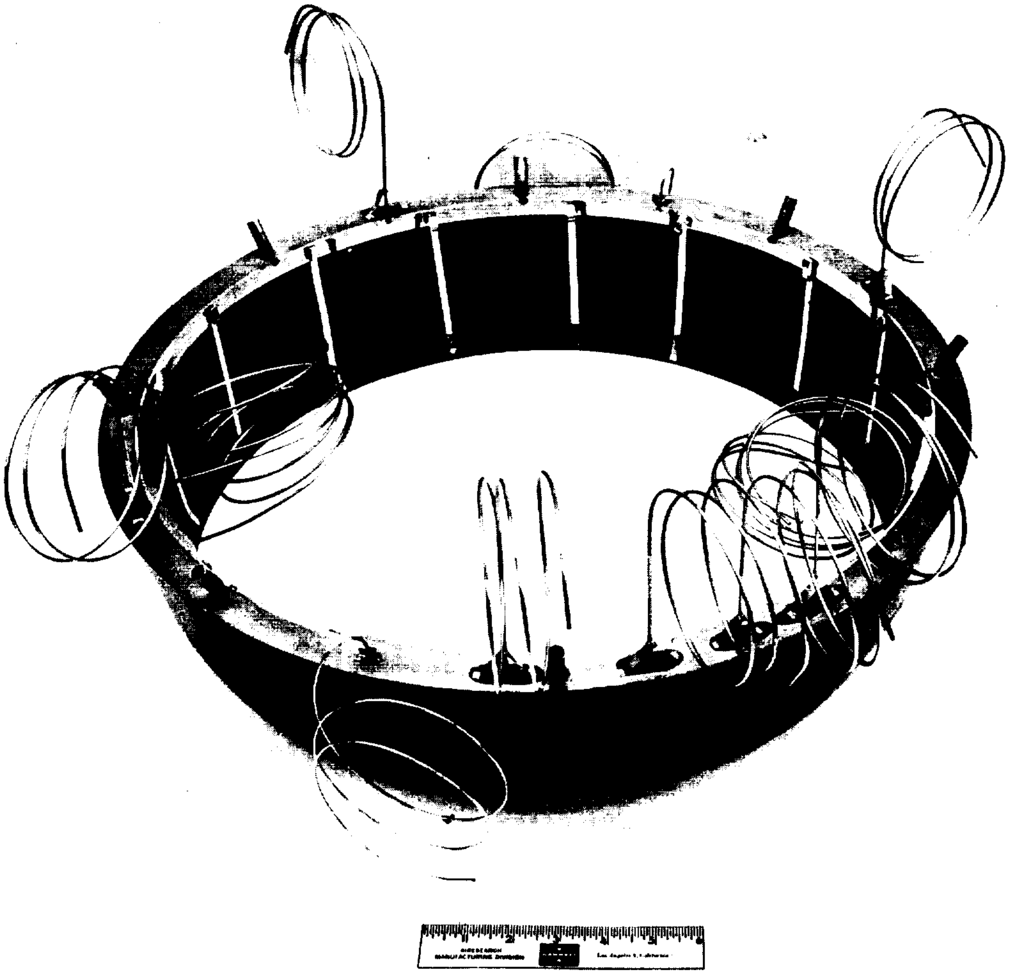

65128-2

Figure 7.6-4 Inlet Manifold Assembled for Brazing

Details for this assembly have been fitted and assembled. Installation in the braze fixture is now in process.

7.7 OUTER SHELL

7.7.1 Development Effort

During the reporting period, all of the detail components for the first (experimental) outer shell assembly were completed to the point of final fitup machining, and the three skin-fin basic shell assemblies scheduled for the program were successfully carried through the primary braze operation. Details of this effort are described below.

7.7.1.1 Aft Support Manifold

In the previous TDR (AiResearch Report No. 68-4482), the preliminary fabrication activities of machining and joining the outer rings of this manifold were described. Subsequent operations joined reinforcing channels to the outer ring and an inner ring (or doubler) to produce a structure with cross-section as shown by Figure 7.7-1 and general appearance illustrated by Figure 7.7-2. The final operation on this manifold before assembling to the skin-fin assembly, was a lathe cut to produce the clearance required for brazing.

7.7.1.2 Forward Support Manifold

Subassembly fabrication activities on this manifold were also described in the previous report. The operations involved in completing this manifold were essentially identical with those described for the atf support manifold with the addition of the tubular outlet duct. The cross-section geometry of this manifold is well illustrated by Figure 7.7-1, and the general appearance of the part is shown by Figure 7.7-3.

7.7.1.3 Second Fuel Injector Manifold

The cross-section geometry of this manifold is the same as that for both the forward and aft support manifolds, as illustrated in Figure 7.7-1. The appearance of this manifold just prior to the final fitup machining operation is shown by Figure 7.7-4.

7.7.1.4 First Fuel Injector Duct

This duct, shown in Figure 7.7-5, is typical of two other distribution ducts used on the outer shell assembly. The duct shown supplies fuel to the first stage injectors by means of individual 1/8-in.-dia tubes. The

The fabrication sequence consists of the forming of 1-in.-dia tubing into a torus, welding the joint, and brazing the required adapter rings in place. Supply tubes are then either welded or brazed in place, followed by final machining of holes.

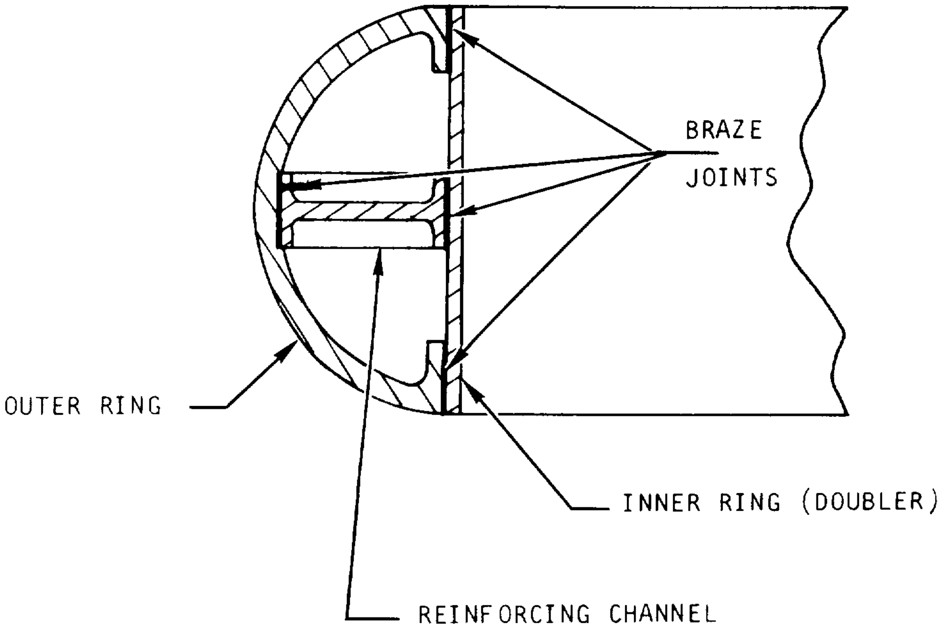
BRAZE
JOINTS
OUTER RING
INNER RING (DOUBLER)
REINFORCING CHANNEL

S-46900

Figure 7.7-1. Manifold - Typical Cross Section

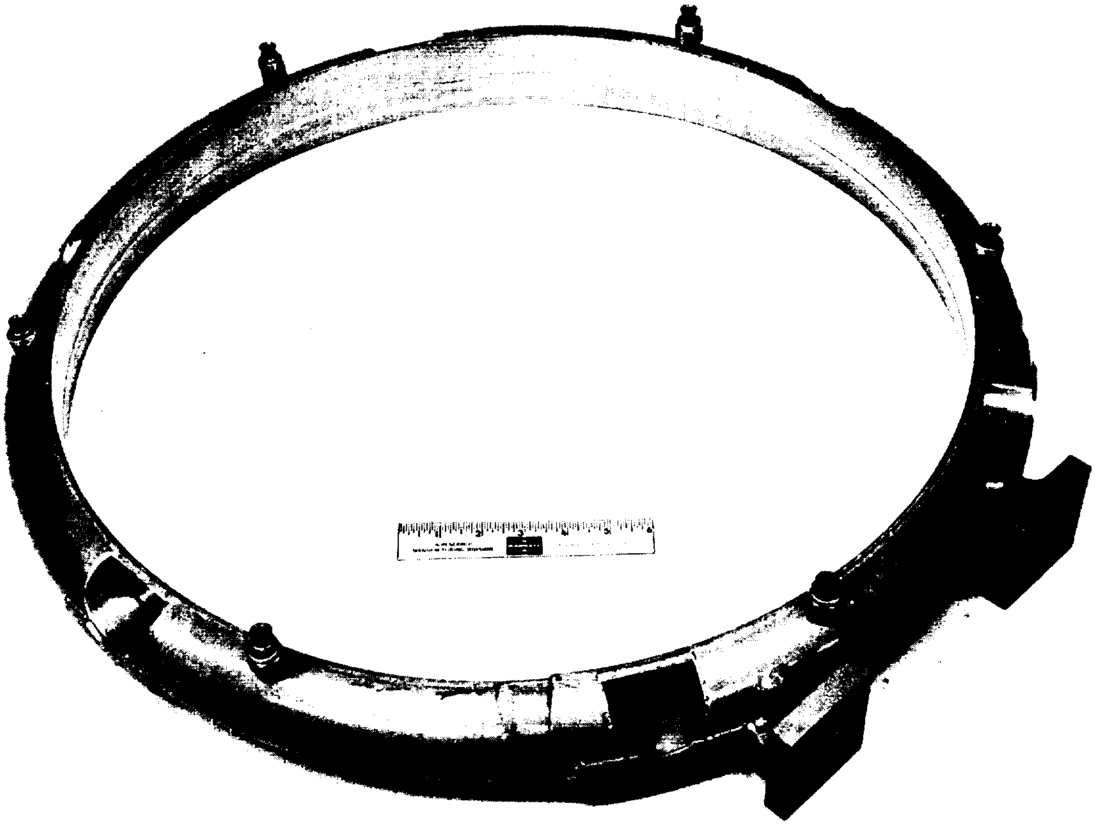

65655-9

Figure 7.7-2 Outer Shell Aft Support Manifold Final Assembly
Ready for Installation on Structure

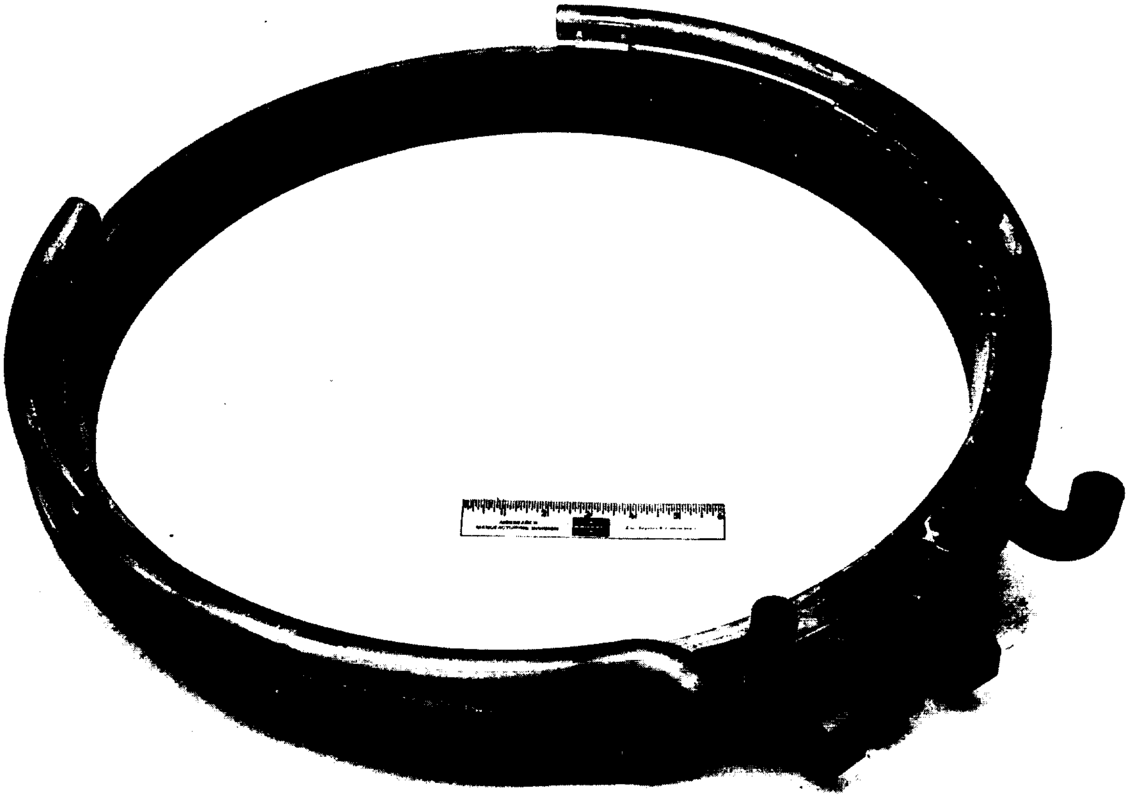

65655-6

Figure 7.7-3 Outer Shell Forward Support Manifold Assembly
Ready for Final Machining

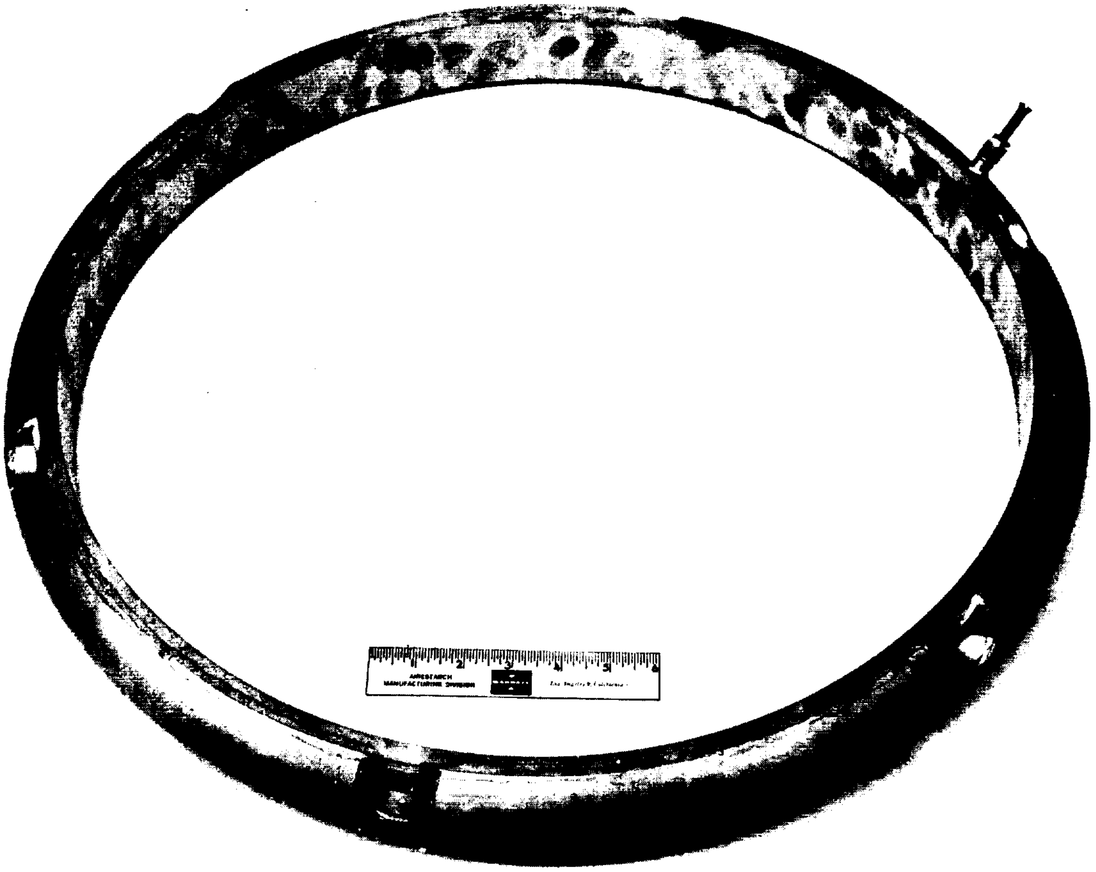

65655-10

Figure 7.7-4 Outer Shell Second Fuel Injector Manifold Final Assembly Prior to Fit-Up Machining

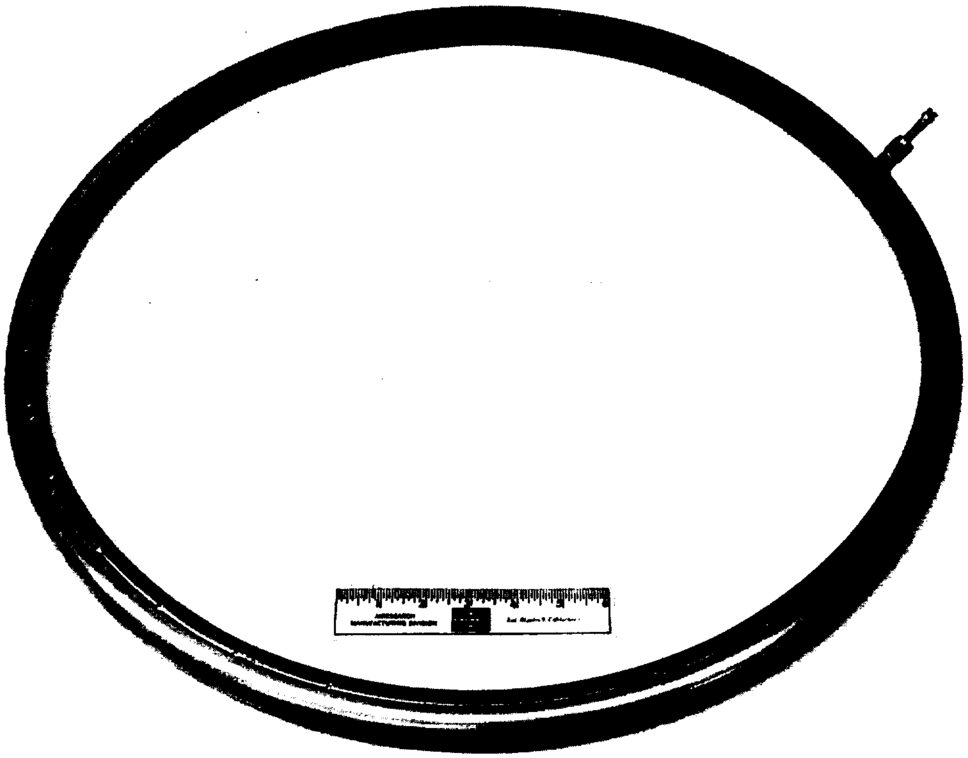

65655-1

Figure 7.7-5 Outer Shell First Stage Fuel Injector Duct

This and the other two distribution ducts are attached to the shell by means of a series of relatively flexible brackets.

7.7.1.5 Third Fuel Injector Ducts

Segmented tubular ducts are utilized directly over the third stage injectors. The segmented ducts fit the spaces between the struts.

The duct sections are first fabricated as a single torus, and the inner adapter ring brazed in place. The final operations consist of the machining to insure fit with the shell, and drilling the holes leading to the injectors followed by cutting into segments and sealing of the tube ends. The appearance of the required six segments is shown in Figure 7.7-6.

7.7.1.6 Forward Distribution Manifold

This multipurpose manifold is located at the extreme forward end of the outer shell assembly. Consisting of two rings brazed together, it serves to (1) channel fuel to the first stage injectors, (2) provide an inlet for the coolant to the forward fin passages of the outer shell, and (3) provide a bolt flange for attachment of the leading edge to the outer shell. The tube connection ring, machined from a Hastelloy X forging is shown in Figure 7.7-7.

7.7.1.7 Trailing Edge Coolant Inlet Manifold

The inlet for coolant to the fin passages at the aft end of the outer shell distributes the coolant from the aft coolant duct through 12 tubular connections equispaced around the circumference. The manifold consists of a brazed assembly of two machined forgings, on which final fitup machining stock has been left on both the inside and outside surfaces. The general appearance of the manifold is shown by Figure 7.7-8.

7.7.1.8 Shell Assembly - Primary Braze

The sequence of operations in brazing the outer shell skin/fin assembly is the same as used for the other assemblies (Reference Sixth TDR, AiResearch Report No. AP-68-4173, Section 7.3.1) except for the size of the assembly and fixturing. Three assemblies were brazed during the reporting period.

The first assembly progressed through the braze cycle without incident until just prior to attainment of the brazing temperature, when the loading pressure decayed. The cycle was carried to completion. Examination after removing the assembly from the insert disclosed a circumferential buckle in the inner skin approximately 11 in. from the large end, at the point of relatively sharp change in contour of the shell.

In addition, the assembly was approximately 0.030 in. smaller in dia than the target dimensions. The buckled area of the inner shell was machined out and a reinforcing doubler installed to permit continuing fabrication evaluation and use of the assembly for pressure drop testing.

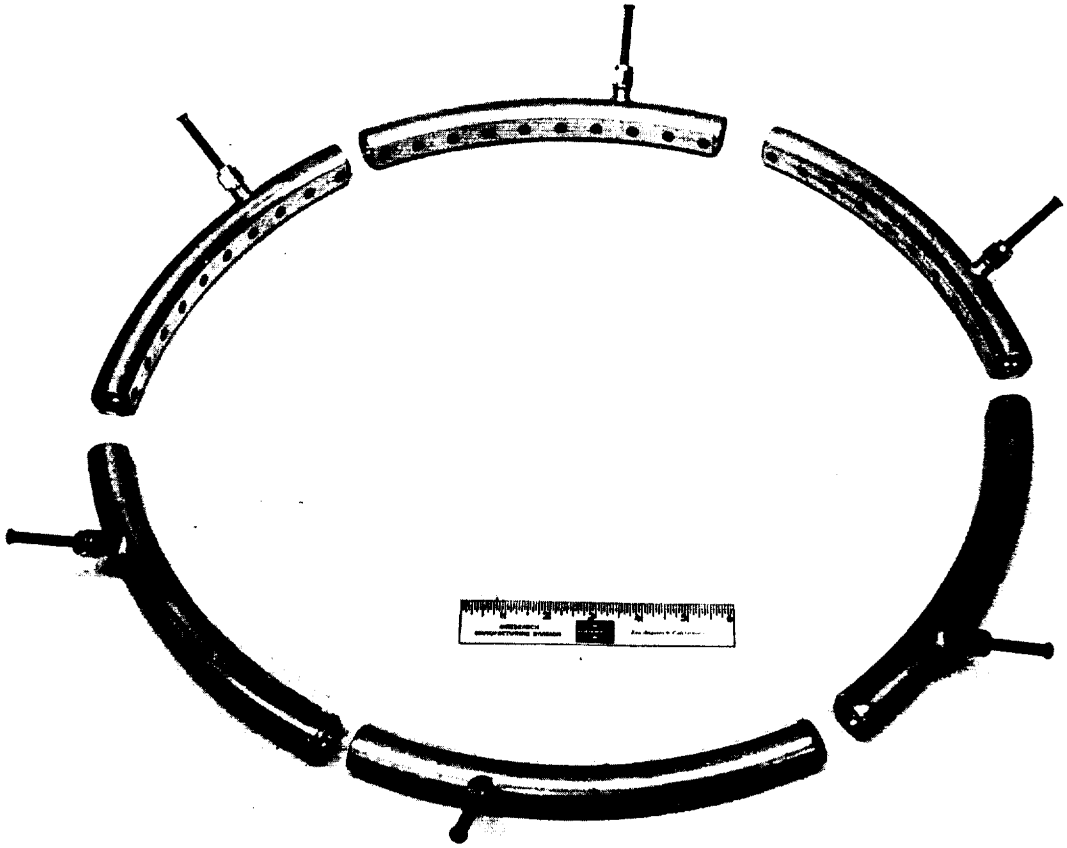

65655-2

Figure 7.7-6 Outer Shell Third Stage Fuel Injector Ducts

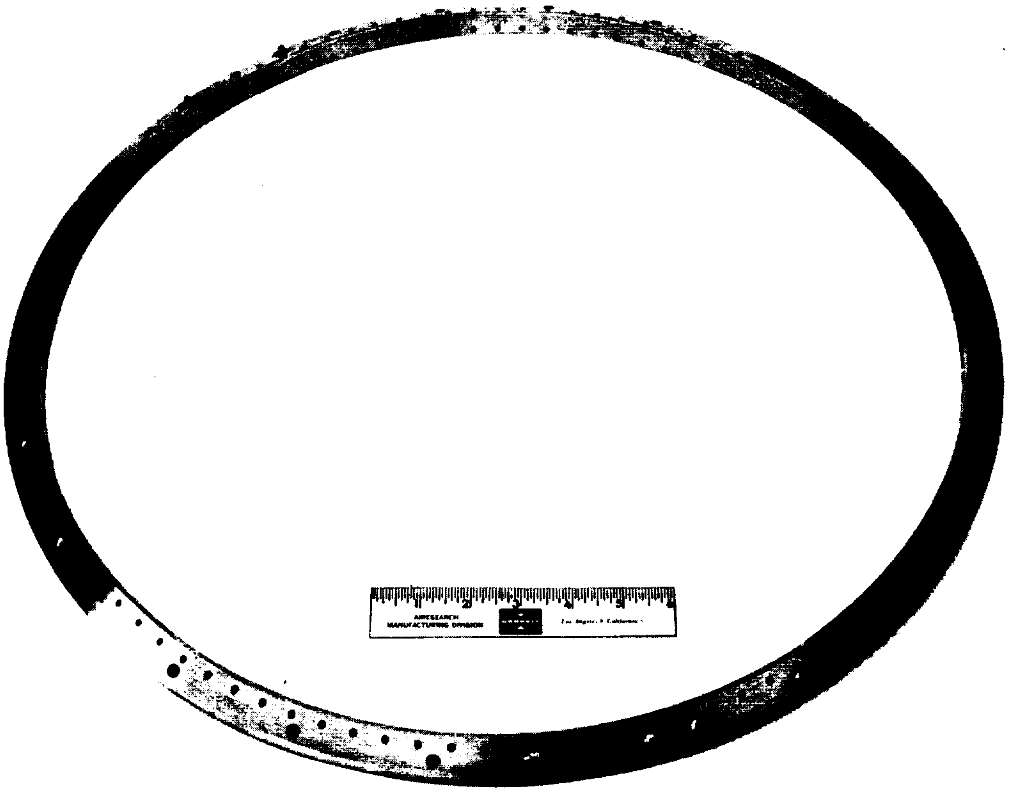
65655-4

Figure 7.7-7 Outer Shell Forward Distribution Manifold - Tube Connection Ring

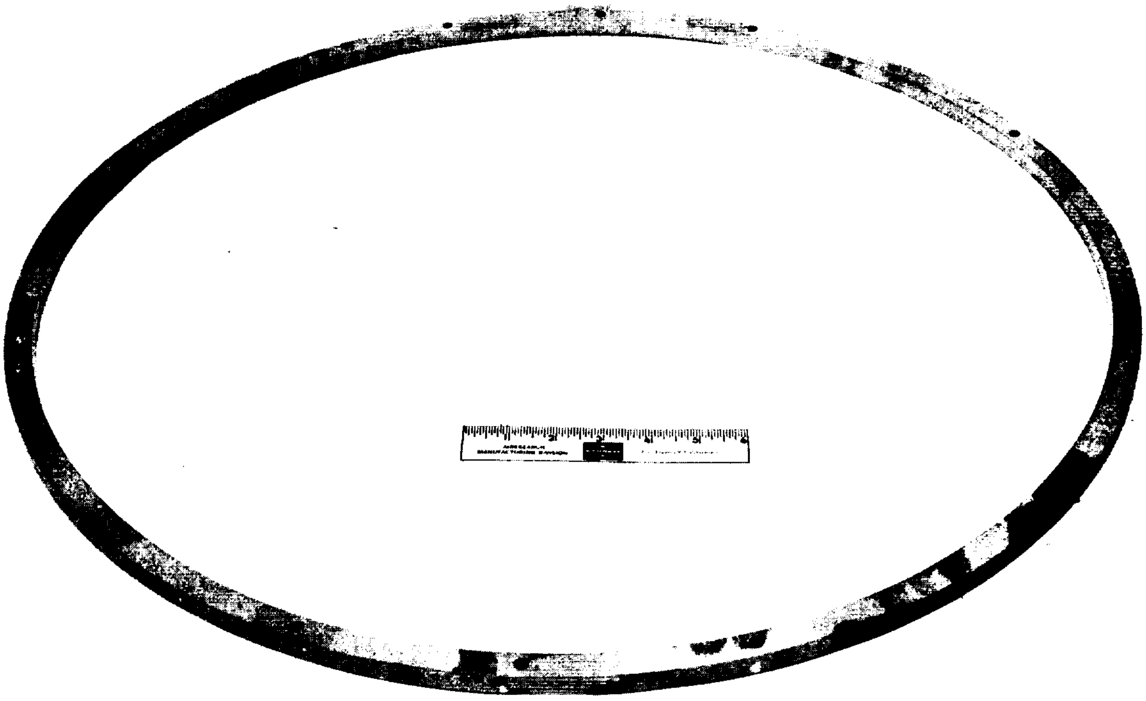

65655-8

Figure 7.7-8 Outer Shell Aft Coolant Inlet Manifold

A strain relieving bead was incorporated in the joint between the inner shell and pressurizingi insert before the second assembly was brazed. Also during this braze cycle, the maximum temperature differential within the assembly-fixture setup was restricted to 100°F. The affect of this limitation was to lengthen the heating portion of the braze cycle from approximately 13 hr to 27 hr. The completed assembly was free of buckling and the same procedure and fixturing was ueed to braze the third shell assembly.

7.7.1.9 Shell Assembly - Second Braze

Following the first braze and proof-pressure testing of the shell assembly, the next series of operations involved brazing the fuel injector inserts in the skin assembly and machining of the various openings in the outer skin preparatory to final assembly.

A series of 108 holes for the fuel injector inserts are first electronic discharge machined (EDM) through the skins, then the shell, fin passages and holes are thoroughly cleaned and inserts brazed in a hydrogen atmosphere. The strut openings are then cut by EDM and the shells proof-pressure tested. Following this, the coolant grooves and final end-trimming machining operations are performed to produce shells of the appearance shown by Figure 7.7-9

7.7.2 Status

The first of the three scheduled outer shell assemblies has completed all primary and secondary braze operations, and machining operations preparatory to final assembly. The installation of the first manifolds is in process.

The second shell assembly has progressed through primary and secondary braze operations and is in process of final machining preparatory to final assembly.

The third shell assembly has progressed through the primary braze operation and is in process of machining for installation of the fuel injectors.

7.8 COOLED-SURFACE PERFORMANCE TEST SECTION

7.8.1 Development Effort

The two cooled-surface performance heat exchangers were completed.

Figure 7.8-1 shows a cross-section of the air sides of the exchanger fin cores, which are the fin surfaces under evaluation. The top core has 20 fins per in., has a height of 0.050 in., and is made of 0.006-in.-thick Hastelloy X sheet. The middle fin sections for these cores, which form the water side, are shown in Figure 7.8-2. This design has 20 fins per in., a height of 0.075 in., and is made of 0.004-in.-thick sheet.

Figure 7.8-3 is a photograph showing the final assembly of one of the units.

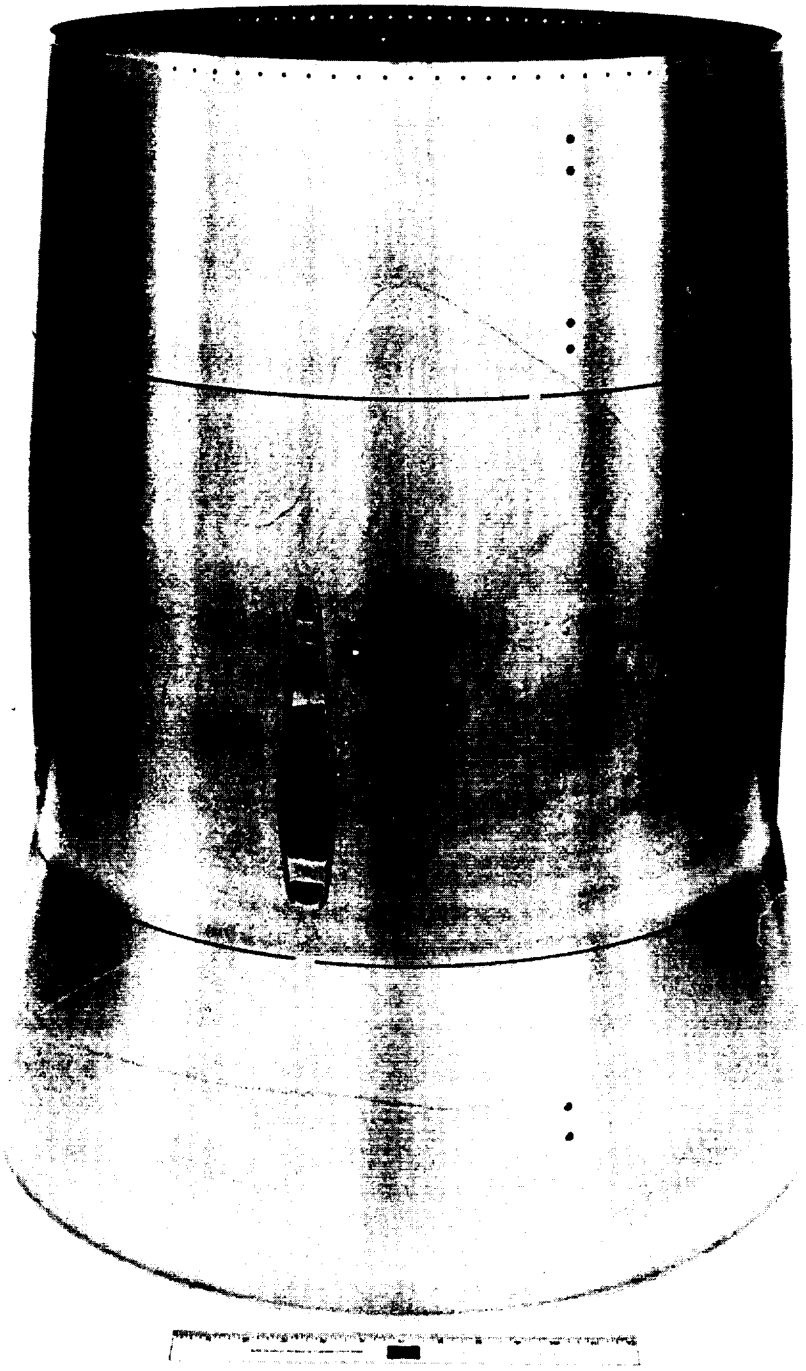

65655-3

Figure 7.7-9 Outer Shell Skin/Fin Assembly Ready for Final Manifold Attachment

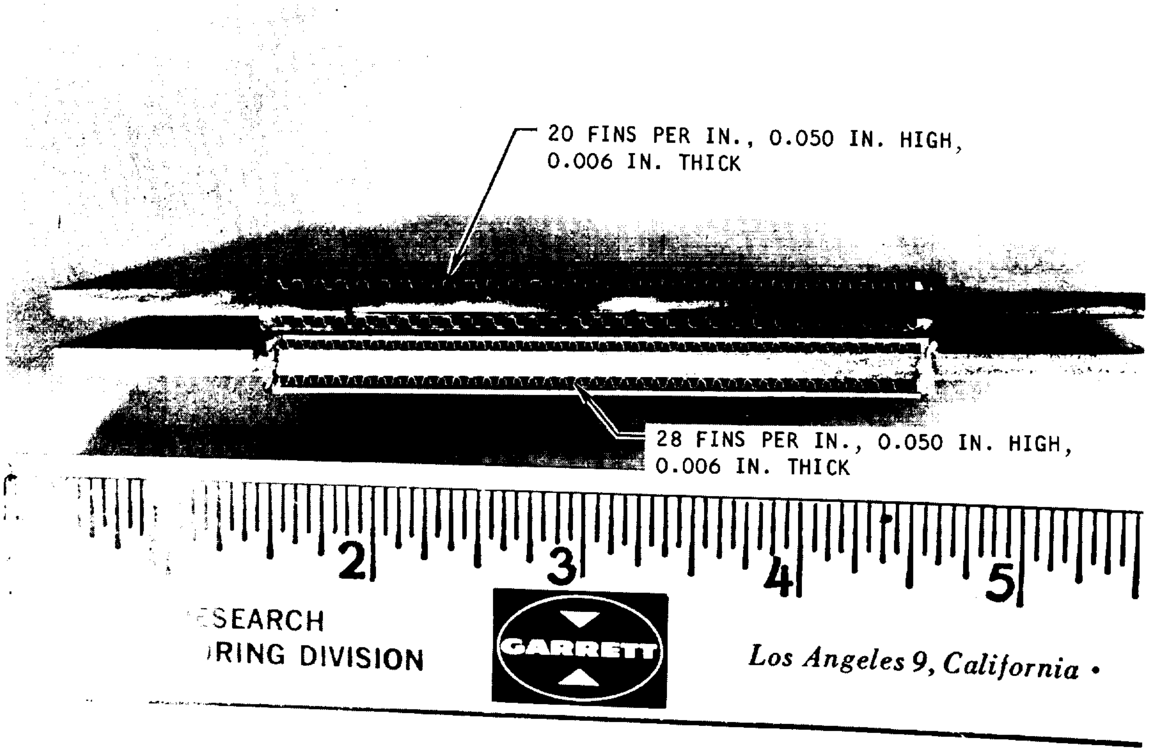
20 FINS PER IN., 0.050 IN. HIGH, 0.006 IN. THICK
28 FINS PER IN., 0.050 IN. HIGH, 0.006 IN. THICK
2
3
4
5
SEARCH
RING DIVISION
GARRETT
Los Angeles 9, California •

F-10344

Figure 7.8-1 Heat Exchanger Fin Cores, Air Side

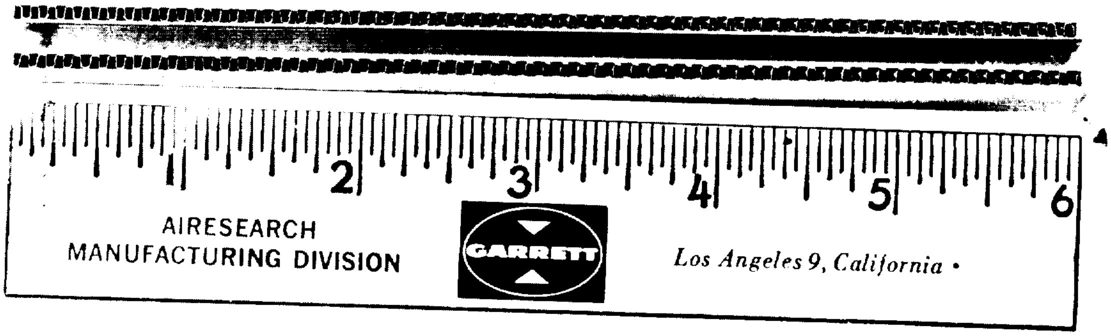
1
2
3
4
5
6
AIRESEARCH
MANUFACTURING DIVISION
GARRETT
Los Angeles 9, California

65057-3

Figure 7.8-2 Heat Exchanger Fin Cores, Water Side - 20 Fins Per in., 0.075 in. High, 0.004 in. Thick

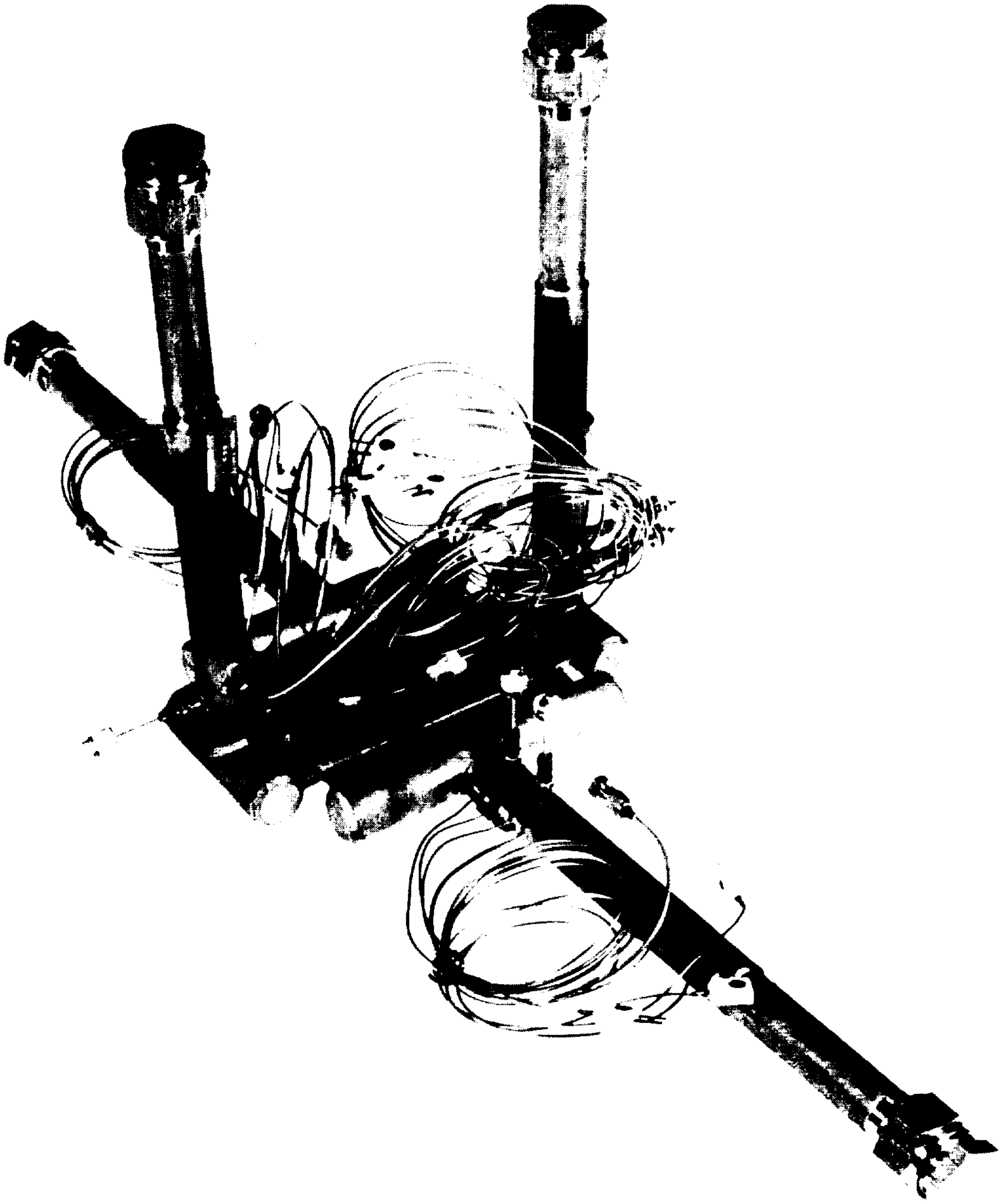

Figure 7.8-3 Cooled-Surface Performance Test Unit

7.8.2 Status

The first of the two units is currently in test (see Section 8.4).

8.0 TESTING

8.1 LEADING EDGE STRAIGHT SECTION

8.1.1 Radiant Heating Test Setup

The test setup shown schematically in Figures 8.1-1 and 8.1-2 is also shown in the photographs of Figure 8.1-3 and 8.1-4. The radiant heating lamp and the planned thermal performance and cycling tests were described in Reference 8, Section 8.1.5. Both the water and air cooling lines are shown connected to the leading edge straight section in Figure 8.1-2, but only one coolant is actually connected (air or water).

8.1.2 Test Conditions and Results

Preliminary calibration tests have been completed using water as the coolant in the perpendicular flow leading edge straight section (Configuration No. 1). At maximum lamp power and 70°F water at a flow of 40 lb/min., the measured stagnation temperature was 454°F. The equation used to obtain a coolant heat transfer coefficient of 5.24 Btu/sec-ft^2-°R was obtained from Section 8.1 of Reference 8 and is shown below.

$$Nu = 0.043\ (Re)^{0.86}\ \frac{(Pr)^{0.4}}{0.72}$$

Water properties were evaluated at an assumed film temperature of 100°F. The Prandtl number dependence in the above equation is assumed, since the hydrogen test data of Reference 8 had a practically constant Prandtl number. From the above values and an inside-to-outside heat flux ratio of 1.6, the outside heat flux was 560 Btu/sec-ft^2, the wall ΔT was 218°F, and the overall ΔT from outside stagnation to water was 387°F.

For thermal fatigue, the overall ΔT (hot surface to backside structure) of from 1000° to 1200°F is significant, rather than stagnation zone wall ΔT. Since maximum overall ΔT with water appears limited to about 400°F at the heat fluxes obtainable with the test equipment, air was substituted for water as the coolant.

8.1.3 Status

The test setup is currently being checked out and calibrated with air as the coolant.

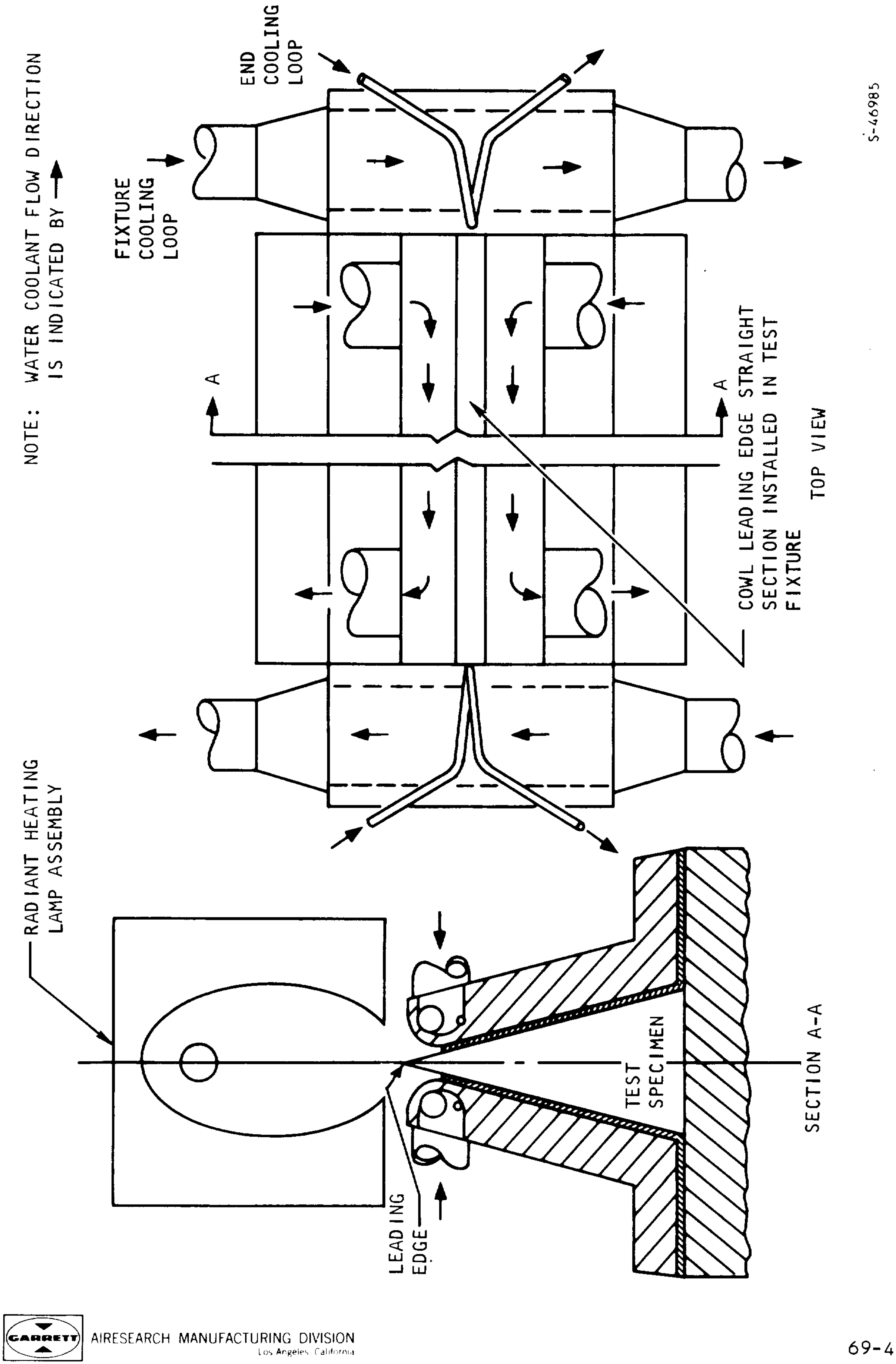
NOTE: WATER COOLANT FLOW DIRECTION IS INDICATED BY →
FIXTURE COOLING LOOP
END COOLING LOOP
A
A
COWL LEADING EDGE STRAIGHT SECTION INSTALLED IN TEST FIXTURE
TOP VIEW
RADIANT HEATING LAMP ASSEMBLY
TEST SPECIMEN
SECTION A-A
LEADING EDGE
S-46985

Figure 8.1-1. Leading Edge Straight Section Radiant Heating Test Fixture Schematic

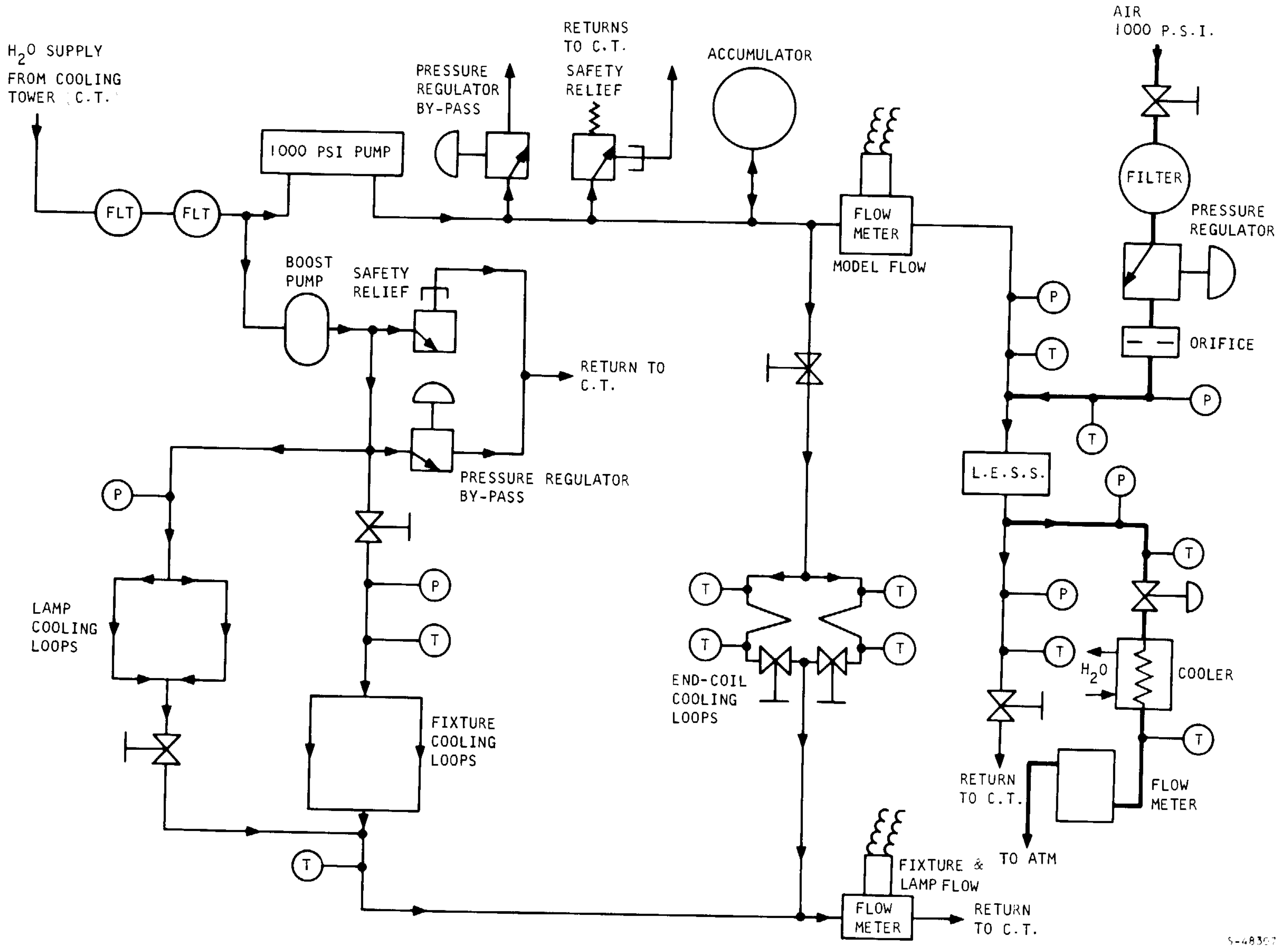
H_2O SUPPLY
FROM COOLING
TOWER (C.T.)
FLT
FLT
1000 PSI PUMP
PRESSURE
REGULATOR
BY-PASS
RETURNS
TO C.T.
SAFETY
RELIEF
ACCUMULATOR
FLOW
METER
MODEL FLOW
AIR
1000 P.S.I.
FILTER
PRESSURE
REGULATOR
ORIFICE
P
T
P
T
BOOST
PUMP
SAFETY
RELIEF
RETURN TO
C.T.
PRESSURE REGULATOR
BY-PASS
L.E.S.S.
P
P
LAMP
COOLING
LOOPS
P
T
T
T
T
T
END-COIL
COOLING
LOOPS
T
P
T
H_2O
COOLER
FIXTURE
COOLING
LOOPS
T
RETURN
TO C.T.
FLOW
METER
T
FIXTURE &
LAMP FLOW
TO ATM
FLOW
METER
RETURN
TO C.T.

Figure 8.1-2 Schematic Water and Air Coolant Systems for Leading Edge Straight Section

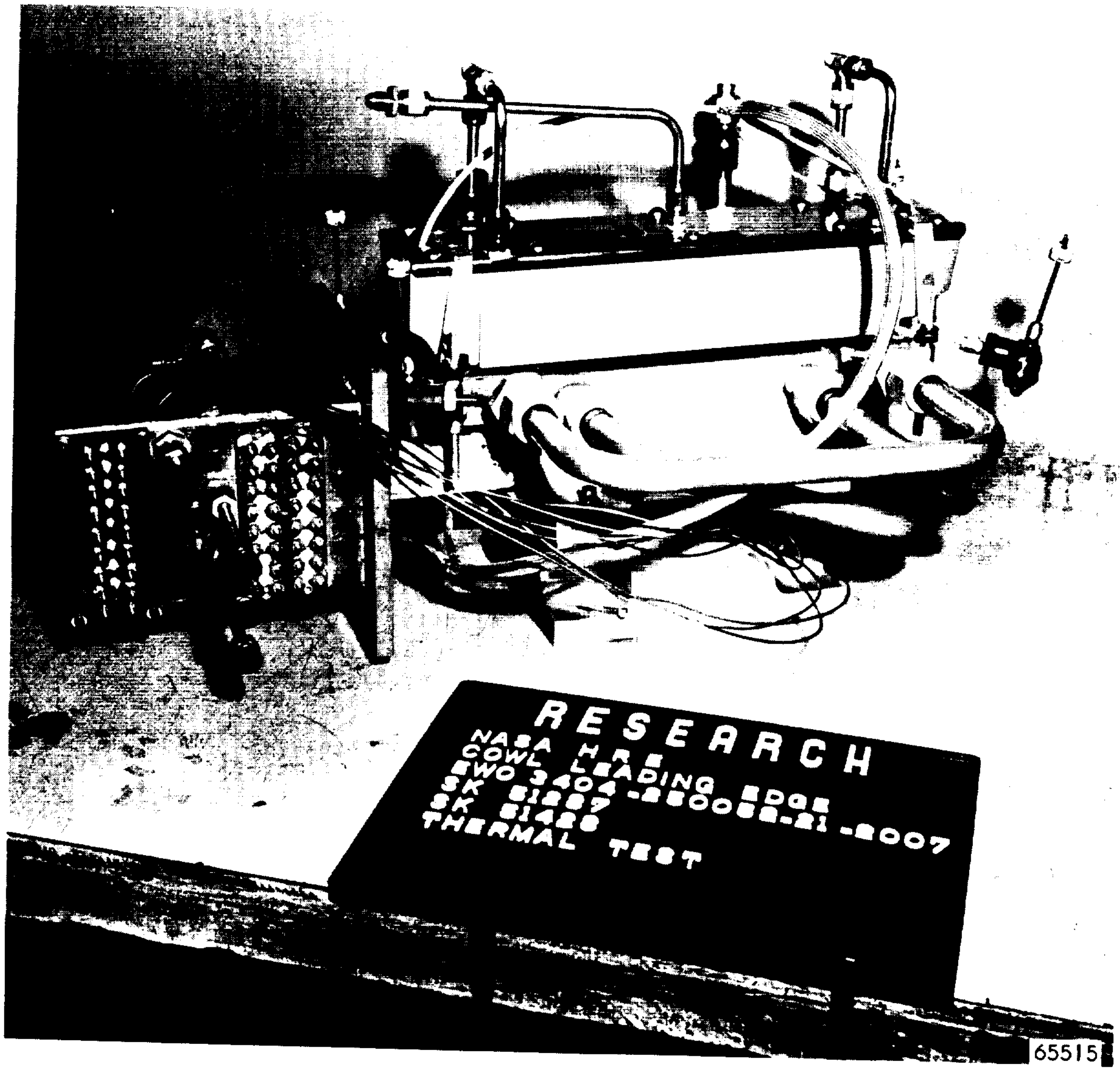
RESEARCH
NASA HRE
COWL LEADING EDGE
EWO 3404-250058-21-2007
SK 51287
SK 51428
THERMAL TEST
65515

Figure 8.1-3 Leading Edge Straight Section Test Setup with Lamp and Fixture

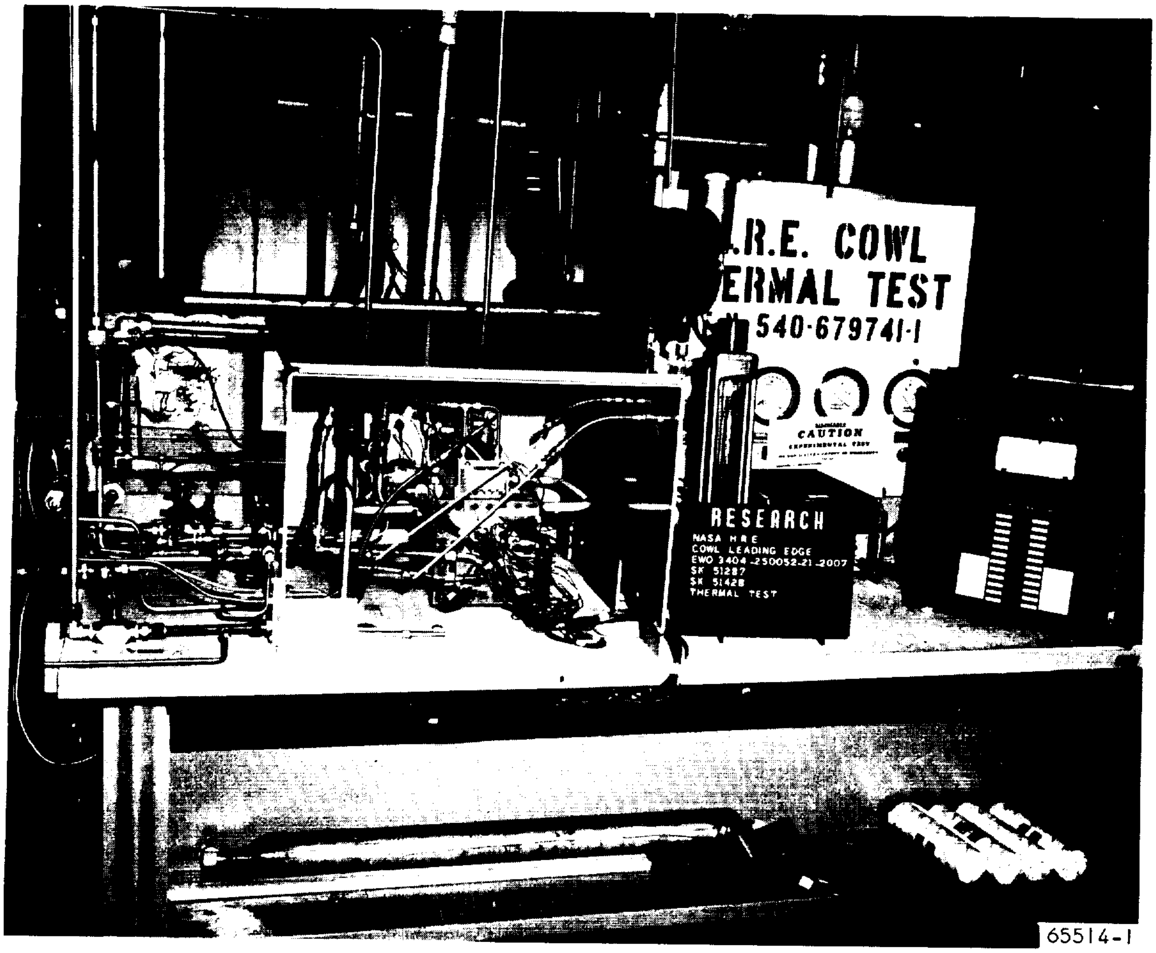
.R.E. COWL
ERMAL TEST
540-679741-1
CAUTION
EXPERIMENTAL TEST
RESEARCH
NASA HRE
COWL LEADING EDGE
EWO 3404-250052-21-2007
SK 51287
SK 51428
THERMAL TEST
65514-1

Figure 8.1-4 Leading Edge Straight Section in Radiant Heating Test Setup

8.2 FULL-SCALE STRUT

Strut leading edge cooling design requires accurate knowledge of the peak heat flux and the total heat load. Additional steady-state full-scale strut performance tests (Runs 30 to 35) were conducted to obtain a more accurate value for the peak heat flux. Eleven thermal cycles have been completed and sample temperature results are reported.

8.2.1 Test Section Configuration

The strut test schematic is shown in Figure 8.2-1 for the strut test assembly of drawing SK-51321, Reference 13. Runs 30 to 35 were conducted with additional instrumentation to measure the strut surface temperature. This consisted of low-melting-point metal strips plasma-sprayed onto the strut leading edge, and bare-bead thermocouples as shown in Figure 8.2-2. The area to be plated was marked off and the metal strips were applied to an approximate thickness of 0.005 in. The following metals, with melting temperatures noted, were plated onto the leading edge.

Metal	Melting Temperature, °F
Indium	313
Tin	449
Bismuth	520
Cadmium	610
Zinc	787
Antimony	1167

Thermocouple wires were spot-welded individually, or in beaded pairs, to the leading edge at the 0-deg (stagnation line) and 90-deg locations. These chromel-alumel thermocouples, with both 6-mil and 12-mil wire diameters, had Inconel sheaths which were trimmed back so that the sheath did not extend beyond the strut side panel.

8.2.2 Test Conditions and Results

8.2.2.1 Steady-State

Nominal strut test conditions are shown in Table 8.2-1 and measured test conditions are summarized in Table 8.2-2, including revised conditions for Runs 23, 24, and 25, previously reported in Reference 5 and discussed in detail below. The gas temperature at the nozzle exit vs hydrogen fuel percent is shown in Figure 8.2-3.

All thermocouples were broken off the strut surface during Run 31. Of the six metallic strips, only those coated with cadmium and zinc provided useful information. The others were completely melted or eroded away.

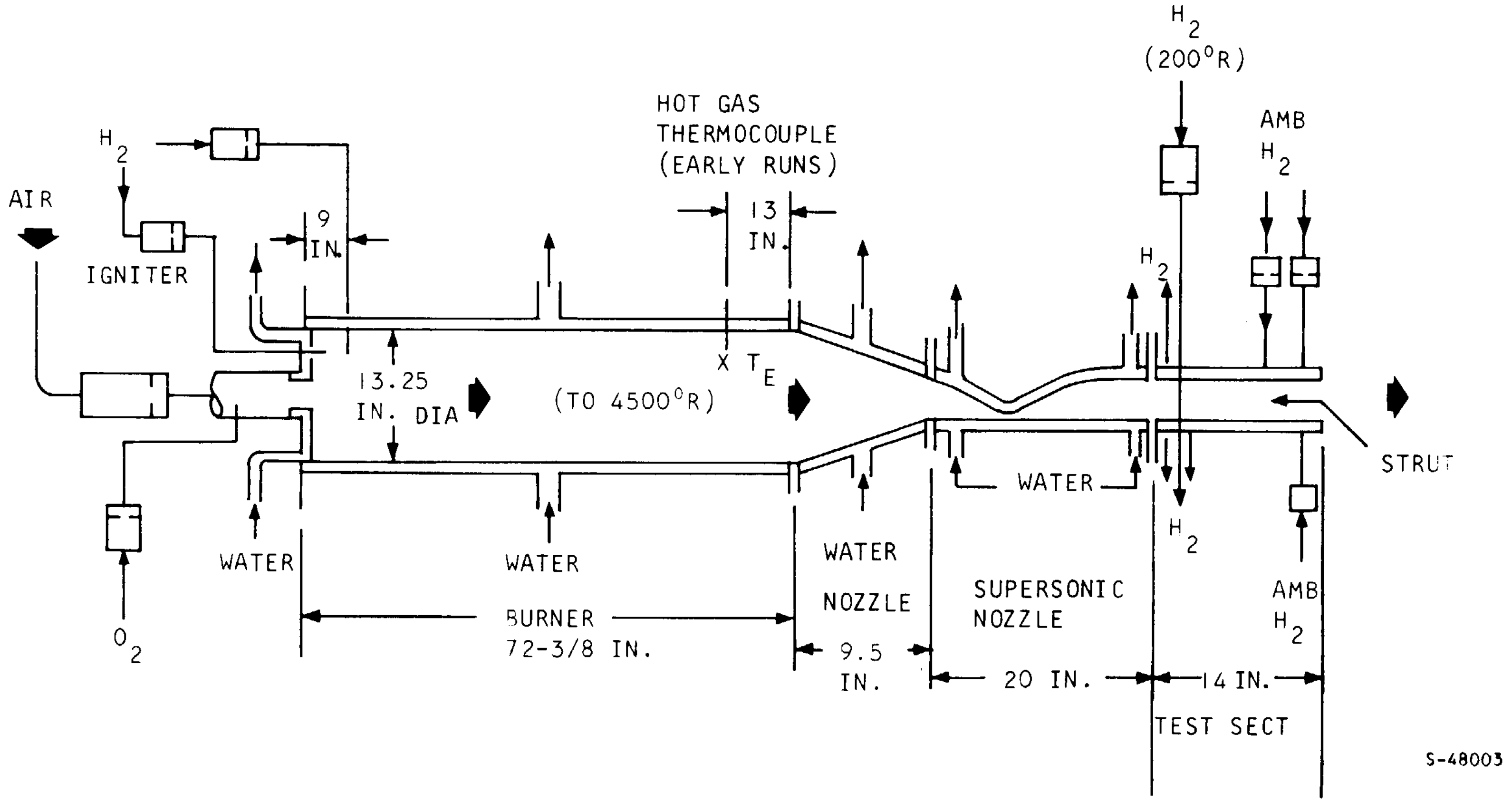
H$_2$
(200°R)
AMB
H$_2$
HOT GAS
THERMOCOUPLE
(EARLY RUNS)
H$_2$
AIR
IGNITER
9
IN.
13
IN.
H$_2$
13.25
IN. DIA
(TO 4500°R)
X T_E
STRUT
WATER
H$_2$
O$_2$
WATER
WATER
WATER
NOZZLE
SUPERSONIC
NOZZLE
AMB
H$_2$
BURNER
72-3/8 IN.
9.5
IN.
20 IN.
14 IN.
TEST SECT
S-48003

Figure 8.2-1. Strut Flow Test Setup Schematic

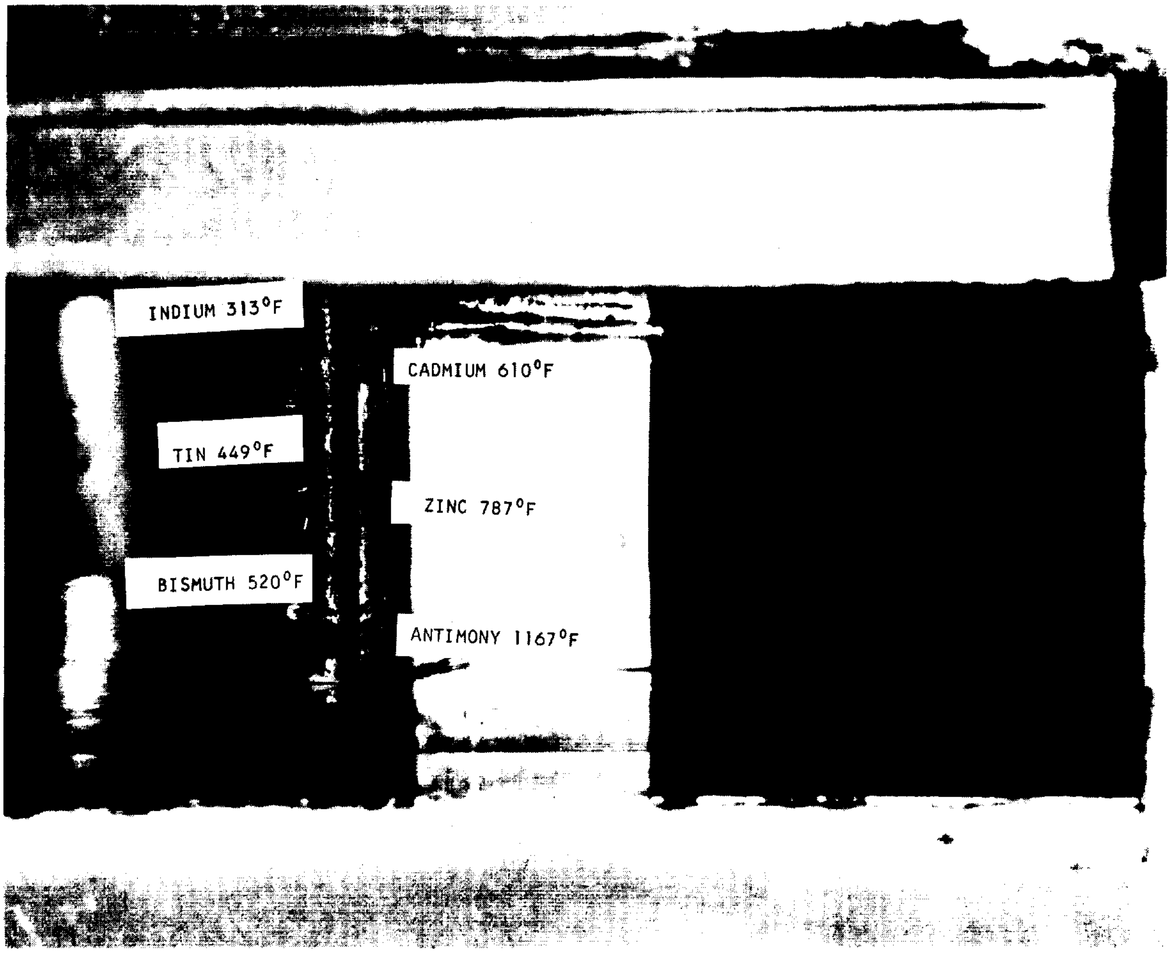
INDIUM 313°F
CADMIUM 610°F
TIN 449°F
ZINC 787°F
BISMUTH 520°F
ANTIMONY 1167°F

F-10363

Figure 8.2-2 Strut SN 6 Before Run 30

TABLE 8.2-1

NOMINAL STRUT SN 6 TEST CONDITIONS

Run Number	Temp, °R	Pressure, psia	Flow Rate, lb/sec	Remarks
28	2000	150	6	Burner checkout. Painted screen shows temperature distribution O.K.
29	2500	200	7.5	
30	2500	150	6	Ceramic placed in strut-support panel gap, LE instrumented with thermocouples (0° and 90°R) and low melting point metals. Lost thermocouples during run. Strut leading edge roughness of 111 to 167 μin. rms.
31	2500	200	7.0	
32	2500	250	7.5	
33	2500	300	8.2	Ceramic filler gone from top strut-support panel gap. During shut down, coolant was turned off before burner wass turned off completely.
34	2800	250	7.5	Ceramic remains only on bottom left side
35	3100	250	7.5	Two LE coolant flows
Cycles 1 - 11	4000	250		Strut leading edge roughness of 361 to 444 μin. rms

TABLE 8.2-2

HRE STRUT TEST

TEST CONDITIONS	Run: 23 Time: 122.35			Run: 24 Time: 2135.6			Run: 25 Time 194.18			Run: 32 Time 954			Run: 33 Time: 255			Run: 35 Time: 662		
Total hot gas flow, lb/sec	7.4			8.12			6.12			6.83			8.25			7.44		
Hydrogen flow, lb/sec	0.113			0.167			0.264			0.087			0.0986			0.129		
Hydrogen flow, percent	1.5			2.1			4.5			1.3			1.2			1.8		
Total enthalpy, Btu/lb	750			958			1766			660			615			865		
Total temperature, ^oR	2500			3030			4400			2360			2220			2810		
Total pressure, psia	243			290			304			214			247			257		
Static pressure, psia	18.4			24.2			28.3			16.5			18			17.3		
Static enthalpy, Btu/lb	356			548			1150			350			323			464		
Static temperature, ^oR	1320			1850			3130			1300			1220			1640		
Mach No.	2.2			2.1			1.9			2.2			2.2			2.2		
COOLANT CONDITIONS	Leading Edge	Side Wall	Support Panel	Leading Edge	Side Wall	Support Panel	Leading Edge	Side Wall	Support Panel	Leading Edge	Side Wall	Support Panel	Leading Edge	Side Wall	Support Panel	Leading Edge	Side Wall	Support Panel
H_2 flow rate, lb/sec	0.057	0.03	0.106	0.056	0.03	0.106	0.046	0.03	0.106	0.049	0.02	0.062	0.051	0.02	0.063	0.019	0.02	0.064
T in, ^oR	159	540	539	168	546	541	162	561	545	160	534	531	153	532	529	175	530	523
T out, ^oR	172	724	728	185	840	843	195	1128	1146	160.5	794	829	153	797	821	222	938	962
P in, psia	661	689	509	676	701	515	694	712	507	678	709	537	682	717	543	763	740	538
P out, psia	189	564	487	197	562	491	192	547	478	221	650	524	223	659	530	735	678	524
Measured local T wall, ^oR										1075 Cadmimum						1247 Zinc		
ANALYSIS RESULTS																		
Local P_T, psia(1)	122			142			134			90			97			105		
Local T, ^oR(2)	2310			2920			4200			2250			2130			2630		
Local V, ft/sec(3)	4030			4530			5400			3960			3820			4460		
Calculated T_W, ^oR(4)	1006			1150			1670			517			577			1190		
Test heat load, Btu/sec	3.37(5)	16.4	60	3.87(5)	28.4	103	5.0(5)	59.7	223.9	1.56			1.45			2.7		
Test avg q/A, Btu/sec ft^2	702	95.4	56	805	165	96	1040	347	209	382			354			660		
Calc avg q/A, Btu/sec ft^2	420			590			1090	338	196	415			395			475		
$(q/A)_{calc\ avg}/(q/A)_{test\ avg}$	0.6			0.74			1.04	0.97	0.94	1.09			1.11			0.72		

(1) Total pressure behind bow shock
(2) Static temperature behind bow shock
(3) Velocity upstream of bow shock
(4) Average outside from $(q/A)_{test\ avg}$ and coolant heat transfer coefficient
(5) Excluding heat load from end effects (back heating and slot heating)

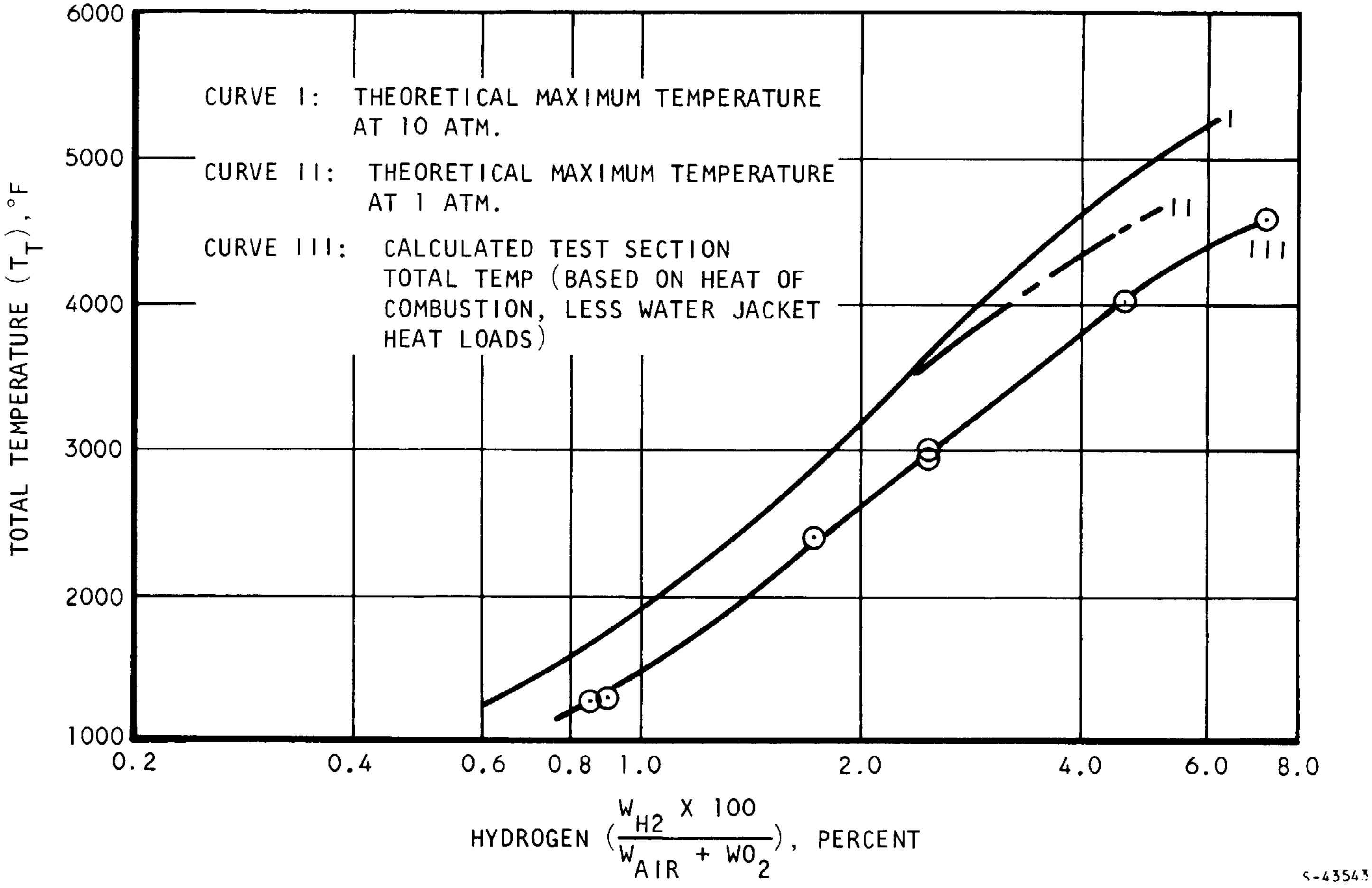

Figure 8.2-3. Combustor and Test Section Total Temperature

The coatings were examined after each run to determine the area melted. It was difficult to distinguish whether the disappearance of the coating material was due to melting or erosion; however in cases of erosion, the surface was pitted and specks of metal remained. Melting action not only produced a clean surface, but left ridge-like edges parallel to the stagnation lines. These were the criteria used in determining the angle to which the coating receded and are necessarily somewhat qualitative. The interpreted temperature constitutes the upper limit local temperature. The actual temperature can be lower than the indicated value if the coating recession was produced in part by erosion.

The cadmium coating was observed to have receded to an angle of 30 deg from the stagnation line after Run 32 (Figure 8.2-4, top). The zinc coating appears melted after Run 32, but was actually eroded, as indicated by specks of zinc still remaining on the stagnation line. The zinc coating was observed to have receded to an angle of 45 deg from the stagnation line after Run 33 (Figure 8.2-4, middle), and receded further back to an angle of 70 deg from the stagnation line after Run 35 (Figure 8.2-4, bottom). During the Run 33 shut-down period, the leading edge coolant was turned off, prior to complete shut-down of the burner. Melting of the zinc, therefore, could not be used to interpret the surface temperature for Run 33.

The strut outer surface temperature at the edge of the receded metal strips was assumed to be the same as the metling temperature. The corresponding heat flux at this location can be computed with knowledge of the internal cooling coefficient. Hence, for Runs 32 and 35, one local heat flux as well as the average heat flux are known. The strut leading edge total heat load and the average heat flux were obtained from the increase of coolant enthalpy. The stagnation line heat flux can be determined from the total heat load providing that the heat flux distribution about the leading edge is know. In general, the heat flux distribution around a leading edge is predictable with reasonable accuracy. However, the tested strut leading edge heat flux distribution is uncertain because of (1) possibility of boundary layer transition over the leading edge region, and (2) turbulence in the flow approaching the leading edge. The latter condition is known to increase the stagnation zone heat transfer rate significantly (References 14 and 15). The combination of the above effects can produce various ratios of the peak heat flux to the average heat flux. Therefore, knowing the average heat flux is insufficient to accurately determine the peak value. Because the stagnation line surface temperature was not obtained from the test, the stagnation line heat flux cannot be determined directly. Instead, using both the average and one known local heat flux and the constraint from plausible modes of heat flux distribution, the peak heat flux was calculated. As an initial step of data reduction, the following heat flux distributions were examined:

(a) Leading edge boundary layer is laminar and the freestream is free of turbulence. The stagnation line heat flux is predicted with Fay-Riddell (Reference 3) and the heat flux distribution around the leading edge is by Lees' theory (Reference 16).

(b) The leading edge boundary layer is laminar, and the approaching flow is turbulent. For this case, the heat flux from the stagnation

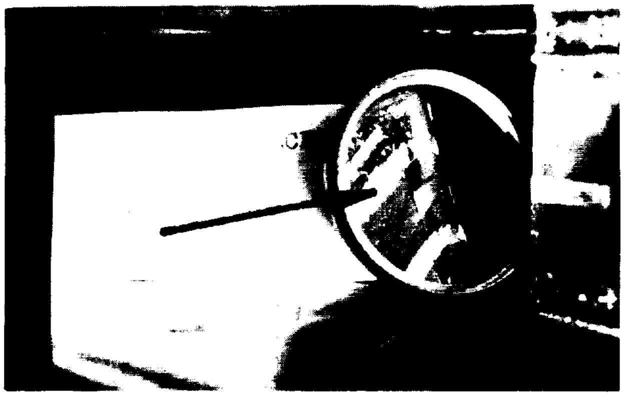

Leading Edge After Run 32
(arrow points to cadmium strip)

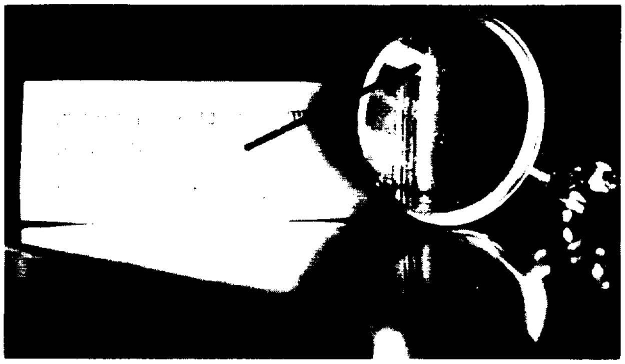

Leading Edge After Run 33
(arrow points to zinc strip)

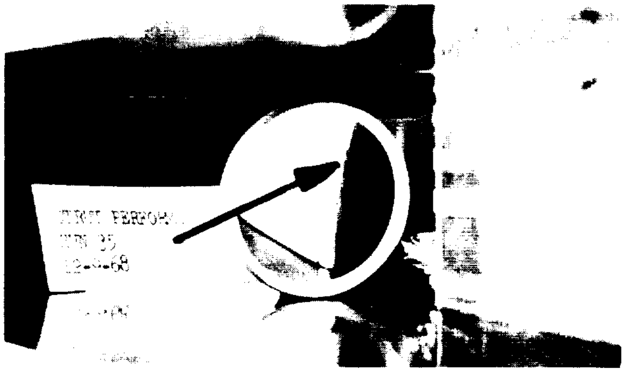

F-10362

Leading Edge After Run 35
(arrow points to zinc strip)

Figure 8.2-4. Strut SN 6 Metal-Strip Melting Results

to the cylinder-wedge junction (θ = 70 deg from the stagnation line) will be higher than Lees' theory predicts. How large an increase is yet to be determined, but the heat flux increase in this region is essentially at a constant multiple of Lees' value. This multiple factor is defined as K-factor. Heat flux distribution for K-factors of 1.0 through 3.5 are shown in Figure 8.2-5. The cylinder-wedge junction is approximately S = 0.1 in. Aft of this station, the heat flux is gradually diminished to K of 1.0 at Station S = 0.16.

(c) The leading edge boundary layer is assumed to become turbulent aft of S = 0.04 in. The freestream turbulence contributes little toward raising the heat transfer on the stagnation line when the local boundary layer is turbulent (Reference 14). Thus, only one level of heat flux is expected, following the boundary layer transition as indicated in Figure 8.2-5. The boundary layer transition can occur earlier or later than that shown. The selection of transition at S = 0.04 in. is arbitrary.

The average leading edge heat flux is defined as the heat absorbed by the leading edge coolant, less the heat conduction and end-effects, divided by the external surface area, which is 0.00408 ft^2. The end-effects were due in part to hot gas flows into the 10- to 40-mil-wide slots around the strut at both the top and bottom panels. This flow produces especially intense heating of the strut flange and the strut socket on the lower panel in the area between the leading edge tube and the plane of the strut-sides-coolant-outlet tube forward edge. Thermocouples were spot-welded to the flange and socket in these locations. The slot was filled with a zirconium oxide base cement from the leading edge to about two in. aft, visible in Figure 8.2-2. The flange, socket, and strut-sides hydrogen outlet temperatures are noted in Table 8.2-3 for Runs 30 through 34 where hot gas conditions were essentially constant, as in Table 8.2-2. The difference between metal and hydrogen outlet temperatures is small through Run 32, but increased by 135^0 to 160^0R between Run 30 and Run 34, when the ceramic cement had been completely removed by gas flow. The cement in the upper slot adjacent to the strut flange had already begun to come out in Run 31.

The ceramic cement in the slot during Runs 30, 31, and 32 permitted a check on the method of calculating the slot heating effect on the strut leading edge heat load. The test data show good agreement with the analytical results, which were calculated based on the following flow model. A one-dimensional-slot flow with slot width of 0.03 in. having the flow rate given by choked-flow with a total pressure corresponding to the value behind the strut-bow shockwave and a flow-contraction ratio of 0.6. The gas total temperature is assumed to be the average between the test-section total and the wall temperatures, since the entering flow was from the boundary layer stream.

In most runs, the coolant ΔT is but 10^0 or 20^0F. For high coolant flow (W = 0.05 lb/sec), the flow either choked, or nearly choked, at the station where the downstream thermocouple was located. A typical pressure

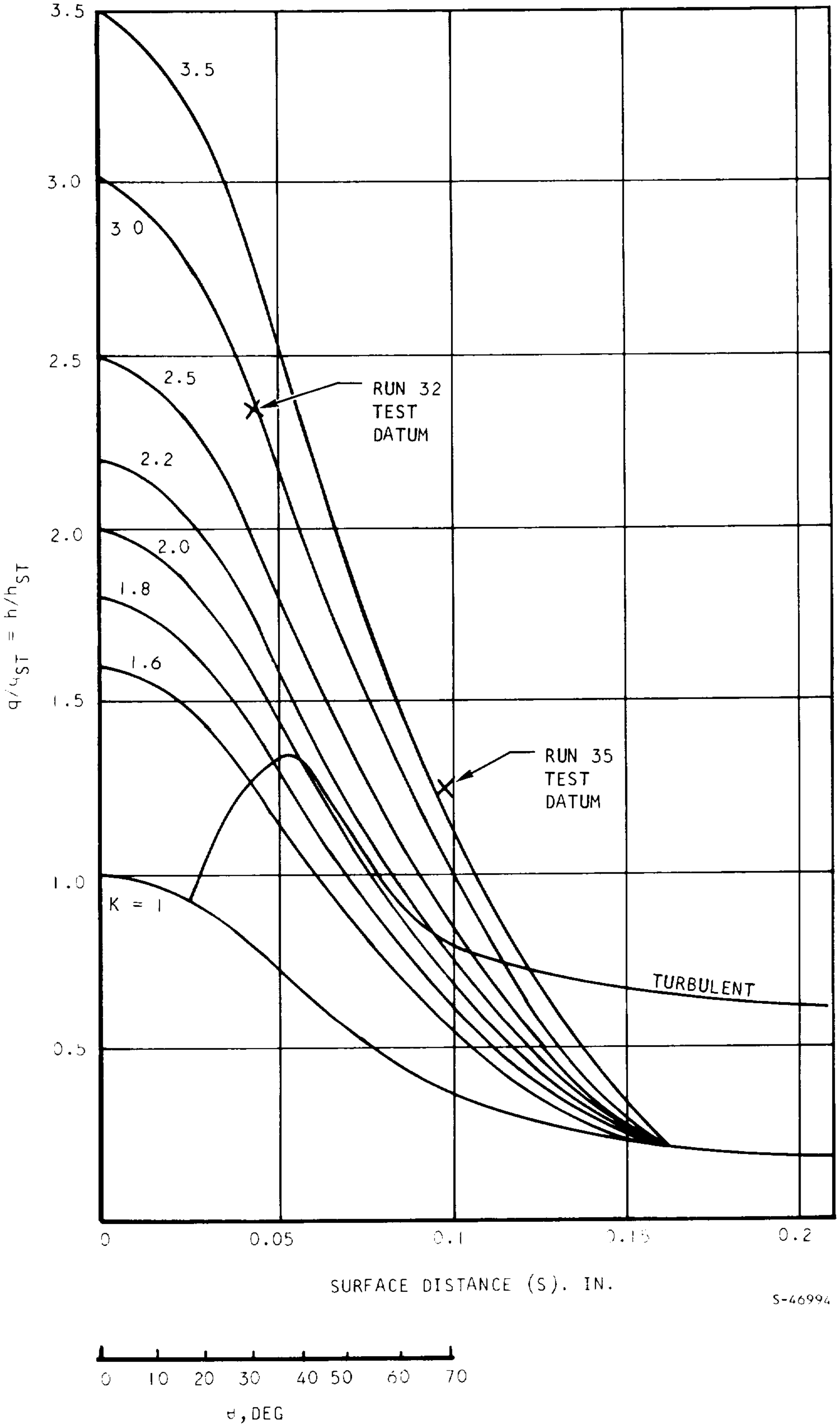

Figure 8.2-5 K-Factor Effects on Heat Transfer Rates

TABLE 8.2-3

STRUT FLANGE AND SOCKET HEATING
FROM SLOT FLOW

Run	Strut Sides Outlet, °R	Flange Temp, °R	ΔT, °R	Socket Temp, °R	ΔT, °R
30	750	730	-20	720	-30
31	781	800	19	745	-36
32	794	816	22	766	-28
33	800	857	57	755	-45
34	800	915	115	930	130

drop for high flow is from 700 psia at the inlet station to 200 psia at the exit station. This throttling action lowered the exit temperature by 8° to 10°F. This corresponds to 25 Btu/lb and has been included in these analyses. The difference (at choking) between the recovery and total temperature corresponds to an additional heat load of about 10 Btu/lb of leading edge cooling hydrogen. The thermocouple recovery factor was the one-third power of the Prandtl number. The heat fluxes for Runs 23, 24, and 25, as reported in Reference 5, were in error because of the above effects. The data have been corrected and are shown in Figure 8.2-6 and Table 8.2-2. The enthalpy for para-hydrogen was taken from Reference 17. The enthalpy for ortho-hydrogen was converted from the para-hydrogen with the aid of Figure 8.2-7.

The internal cooling coefficient is a function of the coolant flow rate wall-to-bulk temperature, and thermal entrance effects. This latter effect is significant because the heat transfer rate is practically zero for the coolant prior to its entering the strut leading edge cooling passage, where the heat flux is several hundred Btu/ft²-sec. The strut leading edge internal cooling coefficient is given by (Reference 18).

$$Nu_b = 0.023 \, R_{e_b}^{0.8} \, P_{rb}^{0.4} \left(\frac{T_w}{T_b} \right)^{-0.57} F_t \qquad (8.2\text{-}1)$$

where F_t is a coefficient to account for the thermal entrance effects and is shown as a function of l/D in Figure 8.2-8. The data points shown in Figure 8.2-8 were taken from Reference 18 for para-hydrogen at an inlet temperature of about 110°R. The entrance length-to-diameter ratio at the position of the cadmium strip is l/D = 2. At this station, the value of F_t is 2.3. The corresponding value for the location of the zinc (l/D = 5.5)

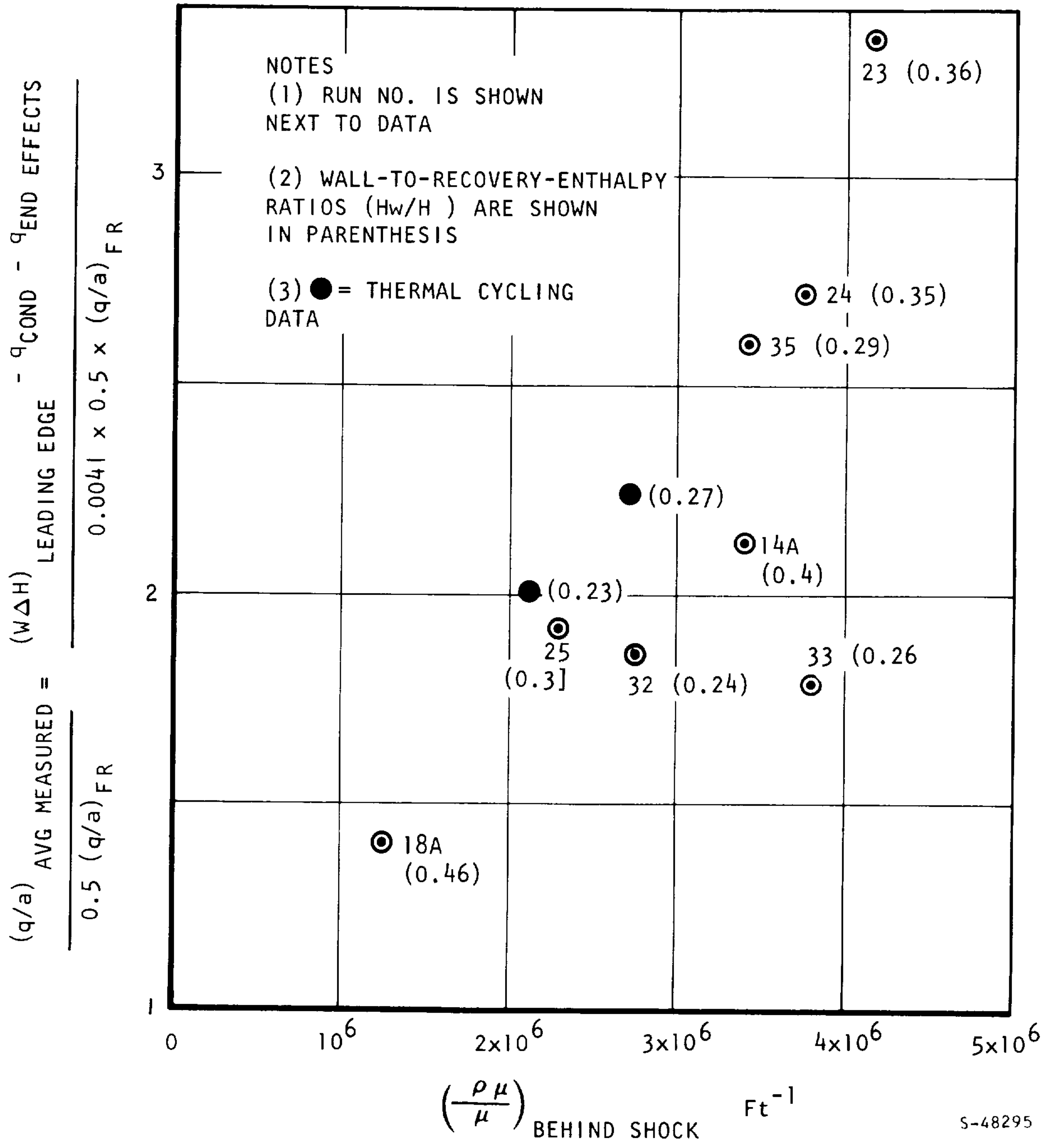

Figure 8.2-6 Ratio of Measured-to-Calculated Average Heat Flux For Strut Leading Edge

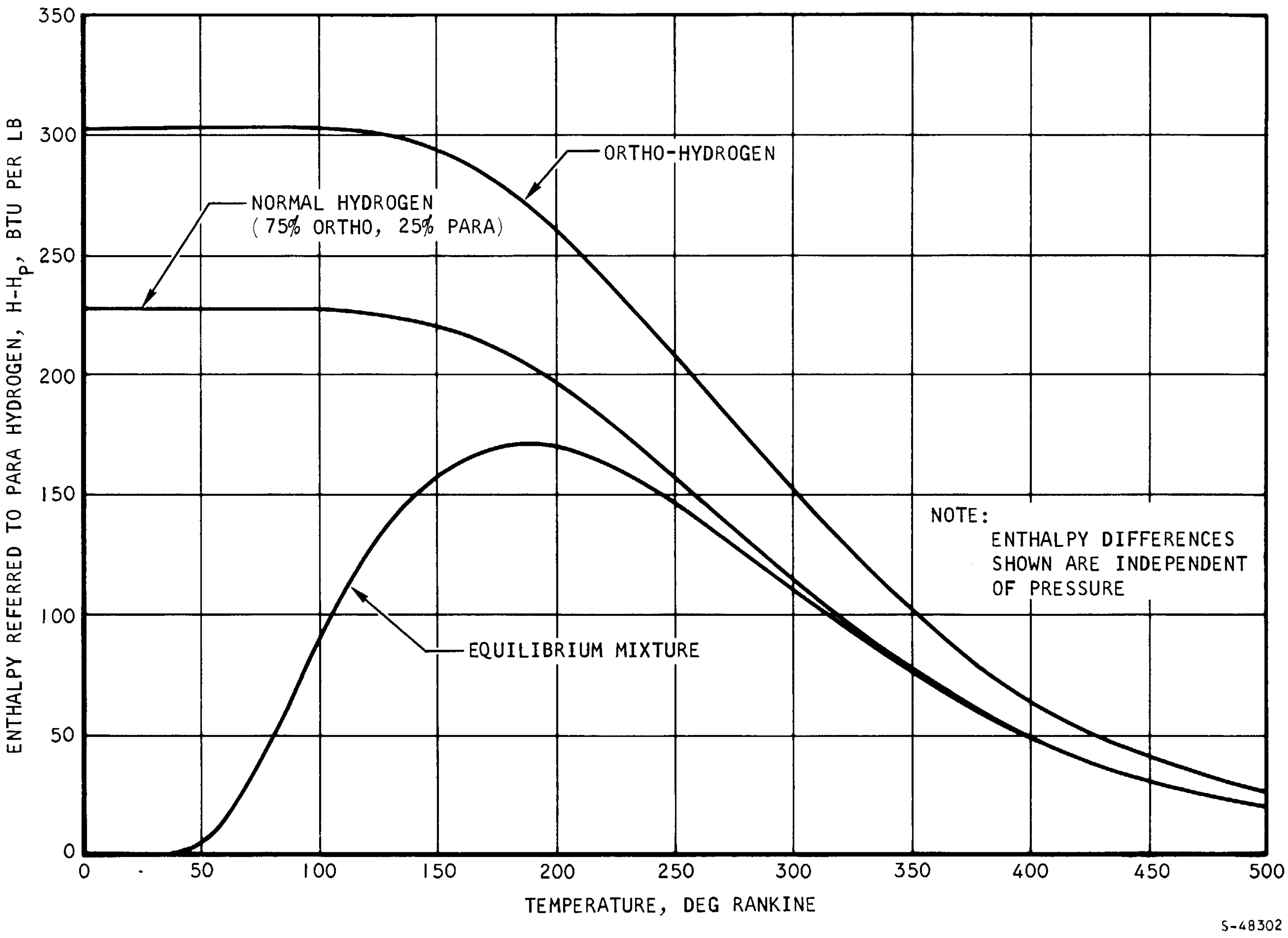

Figure 8.2-7 Enthalpy of Ortho-, Normal-, and Equilibrium-Hydrogen Relative to Para-Hydrogen

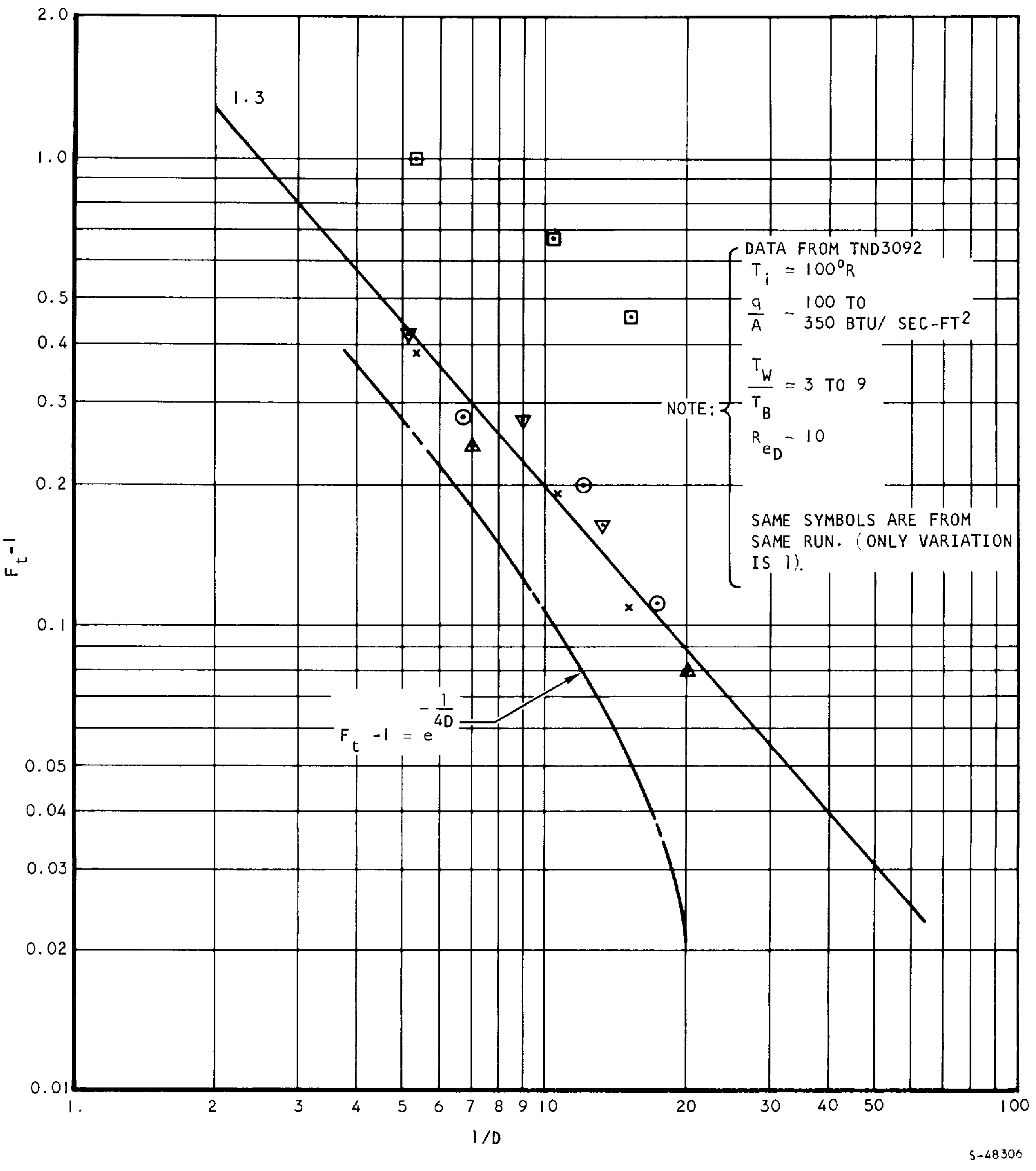

Figure 8.2-8 Thermal Entry Effect for Para-Hydrogen at 110^{0}R (Approximately)

is $F_t = 1.35$. The heat flux can be computed with the internal cooling coefficient, the bulk coolant temperature, and either the internal or external wall surface temperature as shown below (this procedure is described in Reference 19).

Conduction equation

$$\left(\frac{q}{a}\right)_1 = \frac{k\left(T_{w_1} - T_{w_2}\right)}{B_1 \; r_1 \; \ln \frac{r_1}{r_2}} \tag{8.2-2}$$

Internal heat transfer

$$\left(\frac{q}{a}\right)_2 = 1.23 \left(\frac{q}{a}\right)_1 = h_2 \left(T_{w_2} - T_b\right) \tag{8.2-3}$$

The coefficient B_1 was introduced to account for tangential conduction effects. B_1 was unity for $\theta = 30$ deg and was 1.2 for $\theta = 70$ deg. The coefficient 1.23 is the ratio of outside to inside radius.

One of the major objectives of this test was to determine the heat flux distribution so that a more accurate stagnation line heat flux is known. To this end, the test was partially successful. The experimental data from Runs 32 and 35 (only runs offering surface temperature) yield the required information--one local heat flux in addition to the average heat flux. These are:

Average heat flux		Run 32	Run 35
Theoretical stagnation heat flux	$\frac{(q/A)_{avg}}{(q/A)_{FR}}$	1.2	1.5
$(q/A)_{local}/(q/A)_{FR}$		2.35	1.25
Angle for $(q/A)_{local}$, deg		30	70

The approximate K-value may be read from Figure 8.2-5 with the measured local heat flux. A better K-value is obtained when a smooth curve guided by Lees' distribution is drawn through the point of local heat flux and at the same time satisfying the average heat flux value. This result is shown in Figure 8.2-9 which indicates a K of 2.9 and 3.6 for Runs 32 and 35, respectively. Since the average heat flux was computed from the coolant heat load (w_{cp} ΔT), while the local heat flux was computed from the wall

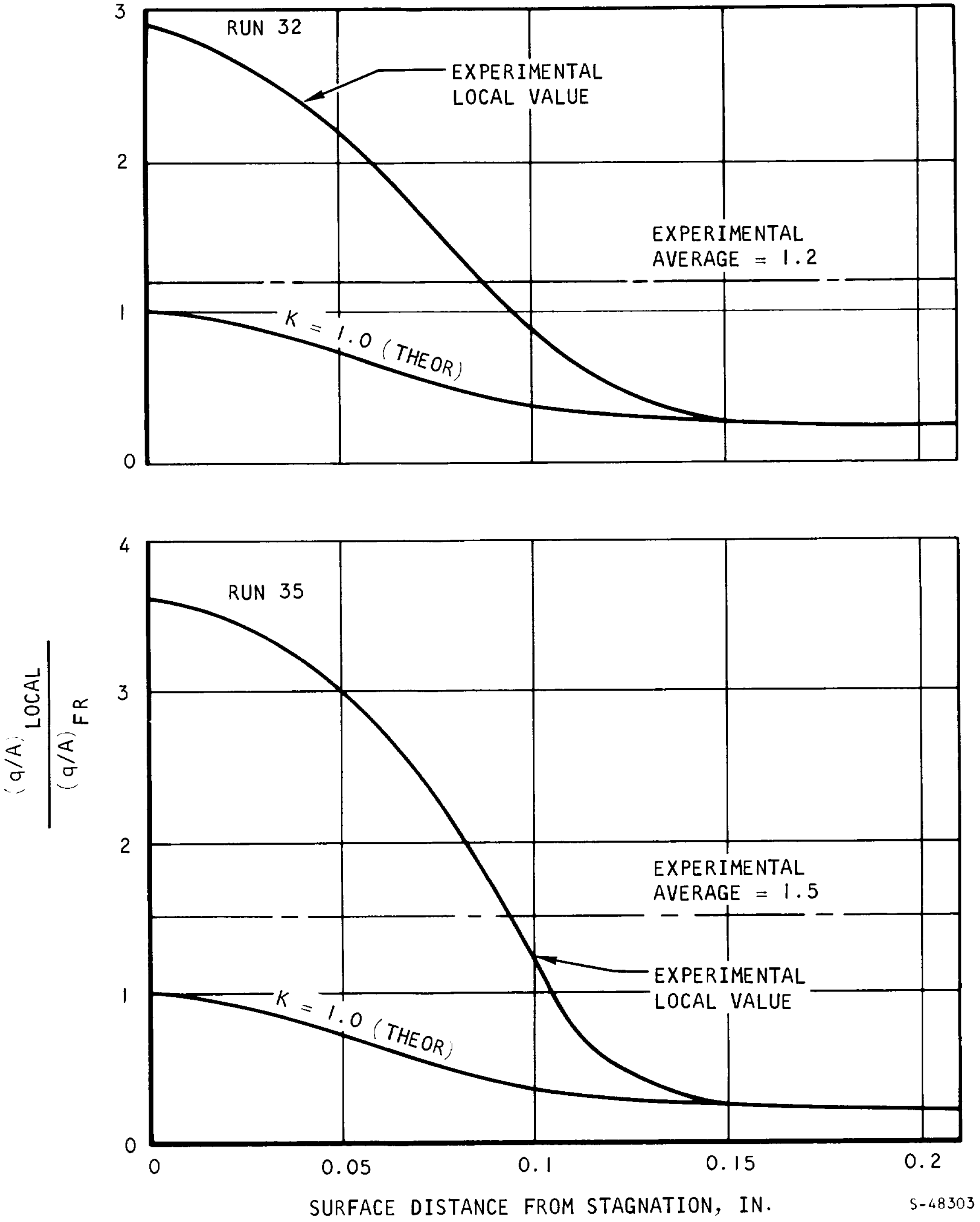

Figure 8.2-9 Heat Flux Distribution

surface and coolant temperature, two independent methods of data reduction were employed.

The zinc strip showed considerable erosion after Run 32. As a check to determine that erosion and not melting was responsible for the disappearance of the zinc, the K-value obtained from the cadmium data was used to calculate the stagnation line temperature at the zinc strip location (zinc strip located at $l/D = 6$ which required thermal entrance factor, F_t, of 1.35 for cooling calculation). The predicted stagnation wall temperature was 1170°R which is below the 1247°R melting temperature of the zinc.

Since most test data provide an average heat flux only, it is desirable to estimate the K-value from the average heat flux. Figure 8.2-5 is cross-plotted to show the relationship between the ratio of the average heat flux to theoretical stagnation heat flux and the multiplier K, Figure 8.2-10. Also shown in Figure 8.2-10 are the test results, including earlier runs. The shaded area represents the possibility of boundary layer transition at the leading edge. Although for Runs 32 and 35, a laminar boundary layer was indicated, no conclusive evidence is found to show that transition never occurs for other runs. Since a laminar boundary layer yields a K-factor for a given average heat flux, the laminar boundary layer curve will yield an upper limiting K-value.

It is noted that heat flux and wall temperatures for Runs 23, 24, and 25 have been revised to incorporate (1) the throttling effects of the coolant flow and (2) the newly adopted internal cooling coefficient, Equation (8.2-1) These revisions do not apply to Runs 14A and 18A, since the coolant flow in these was water.

8.2.2.2 Thermal Cycling

Eleven thermal cycles have been completed on strut SN 6 to nominal hot gas conditions of 250 psia total pressure and 4000°R total temperature. Some of the resulting temperatures for Cycle 3 and Cycles 8 through 11 are shown in Figures 8.2-11 through 8.2-18. Cycle 3 has a longer steady-state time than subsequent cycles but the same maximum temperatures reached in the shorter cycles. Good repeatability of conditions is indicated by a comparison of the maximum temperatures for the various cycles. The plotted hot gas temperature was obtained by use of Figure 8.2-3. The leading edge of strut SN 6 after Cycle 11 is shown in Figure 8.2-19, and has a maximum roughness of 444 μin.rms compared with Figure 8.2-1a in Reference 6, which has a roughness of 167 μin. rms after Run 27.

Strut leading edge temperature was obtained from Figure 8.2-20. For high temperature (4000°R), where the Reynolds number is lower, the hot gas heat transfer coefficient was calculated by the method of Fay-Riddell (Reference 3) and multiplied by 1.5 for surface roughness up to about 300 μin. rms and 1.8 for greater roughness. At lower gas temperatures (2000°R and below) where the Reynolds numbers are higher, only the 1.8 multiplier was used for the heat transfer coefficient from the Fay-Riddell method. Test results in Section 8.2.2.1 indicate that the multiplier may be higher than 1.8. A limit

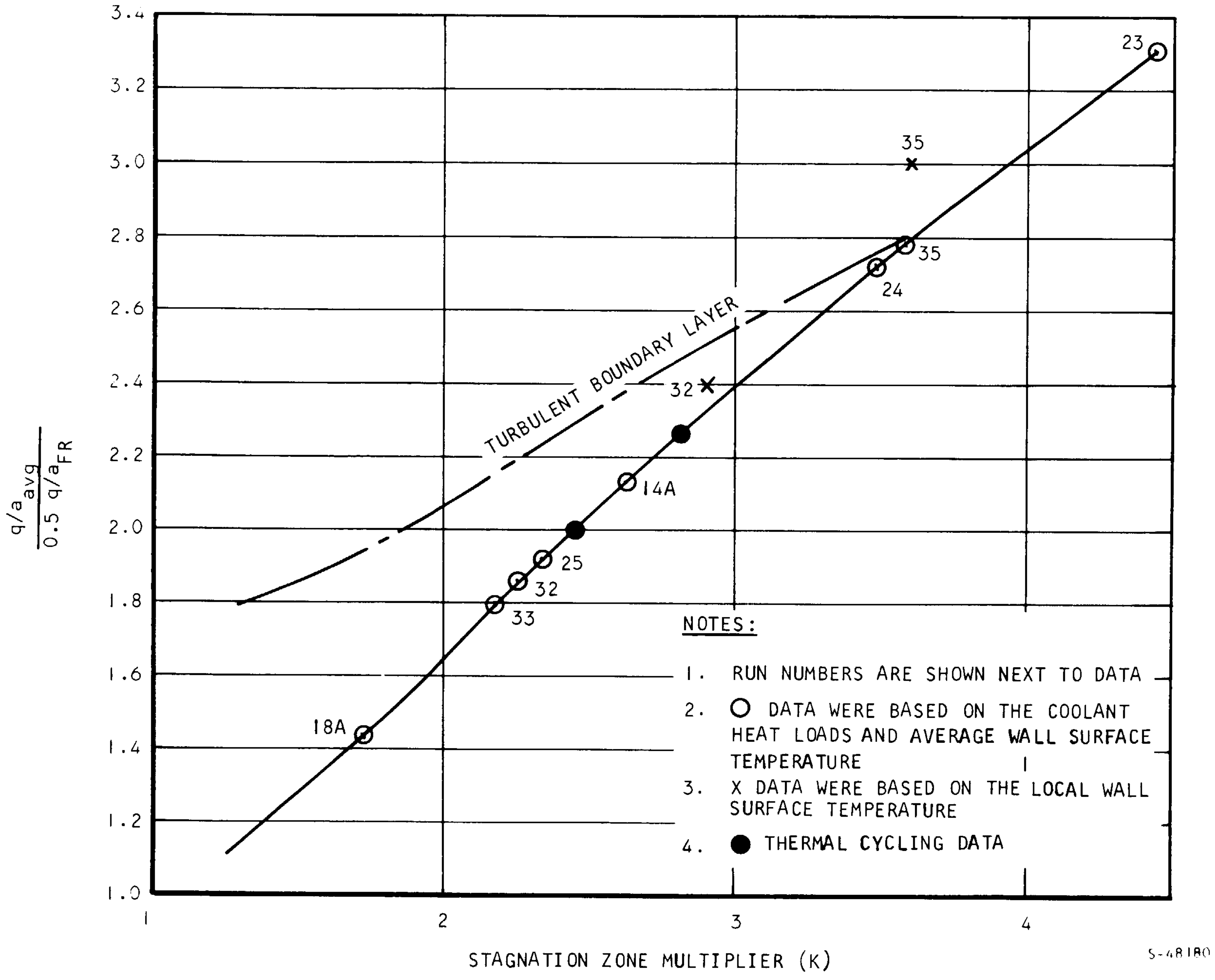

Figure 8.2-10 Average Heat Flux vs K-Factor

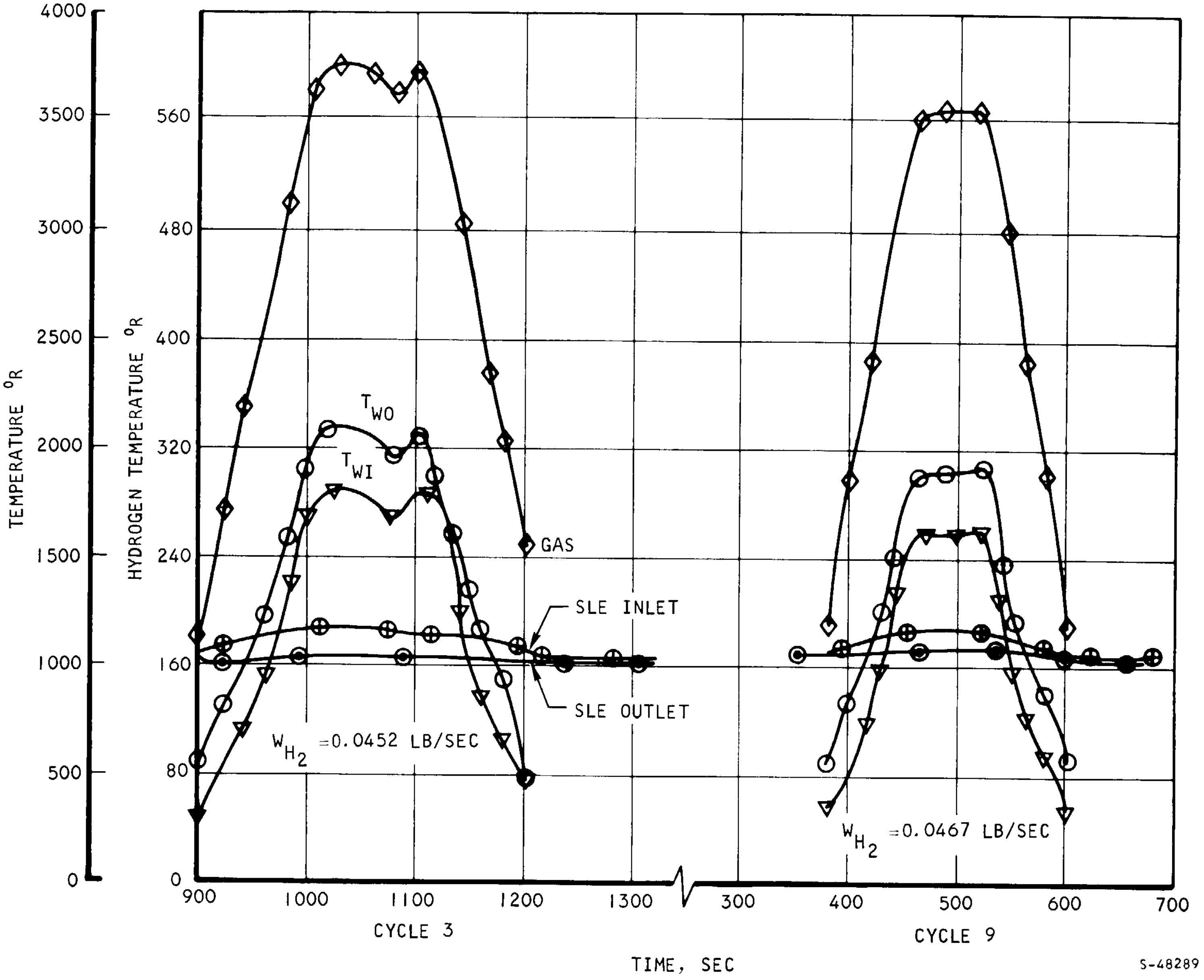

Figure 8.2-11 Strut SN 6 Leading Edge Temperatures for Cycles 3 and 9

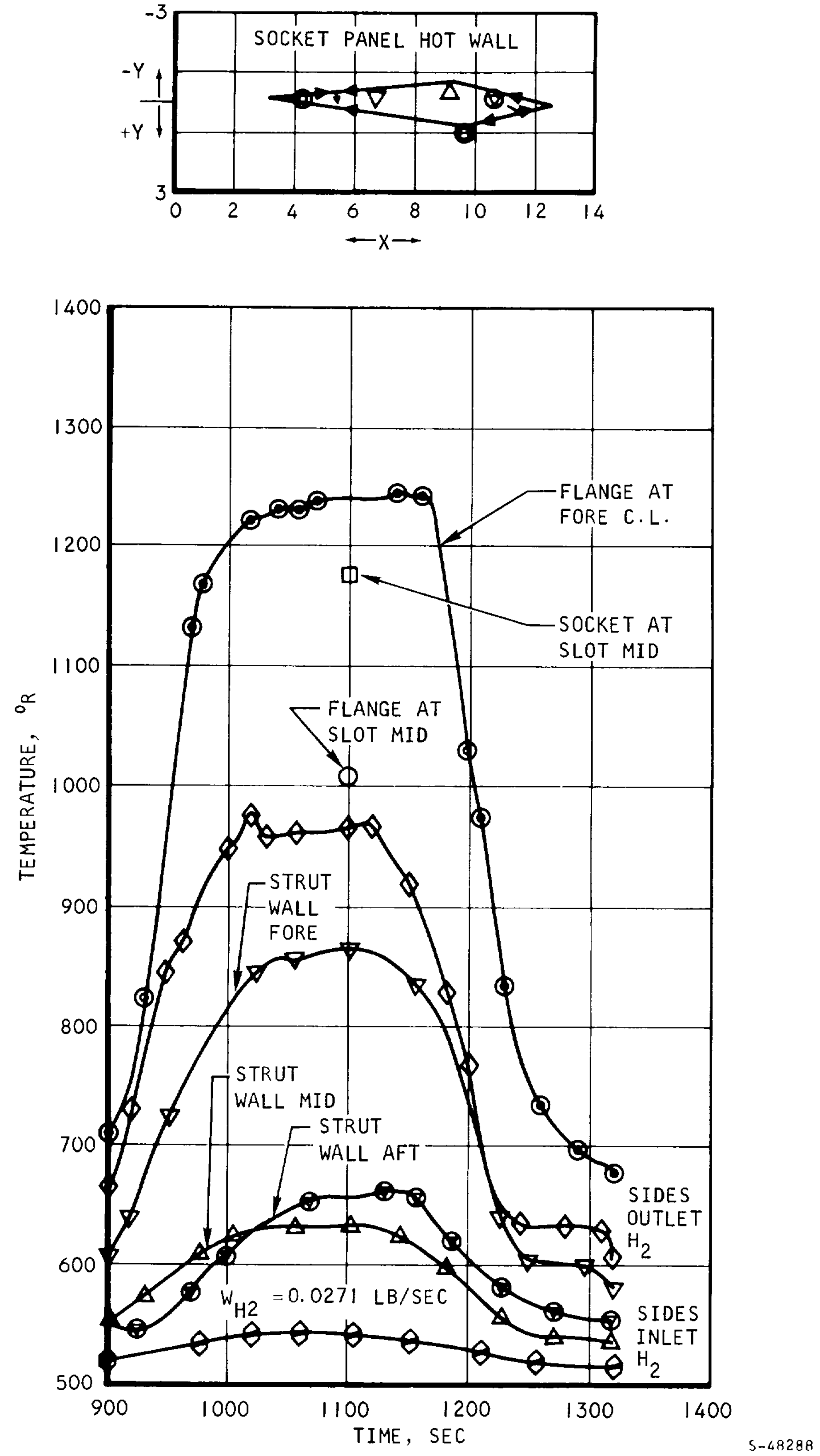

Figure 8.2-12 Strut SN 6, Cycle 3 Strut Temperatures

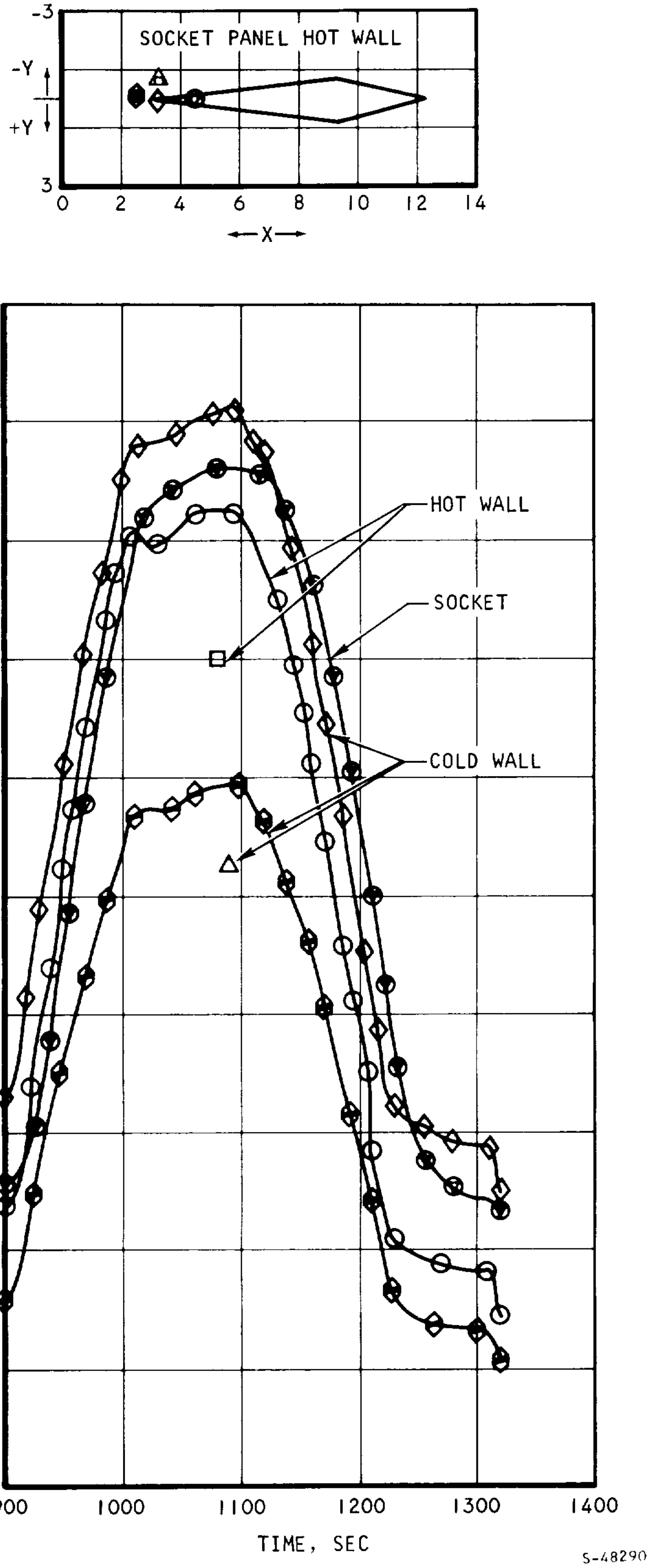

Figure 8.2-14 Strut SN 6, Cycle 3 Panel Wall and Socket Temperatures

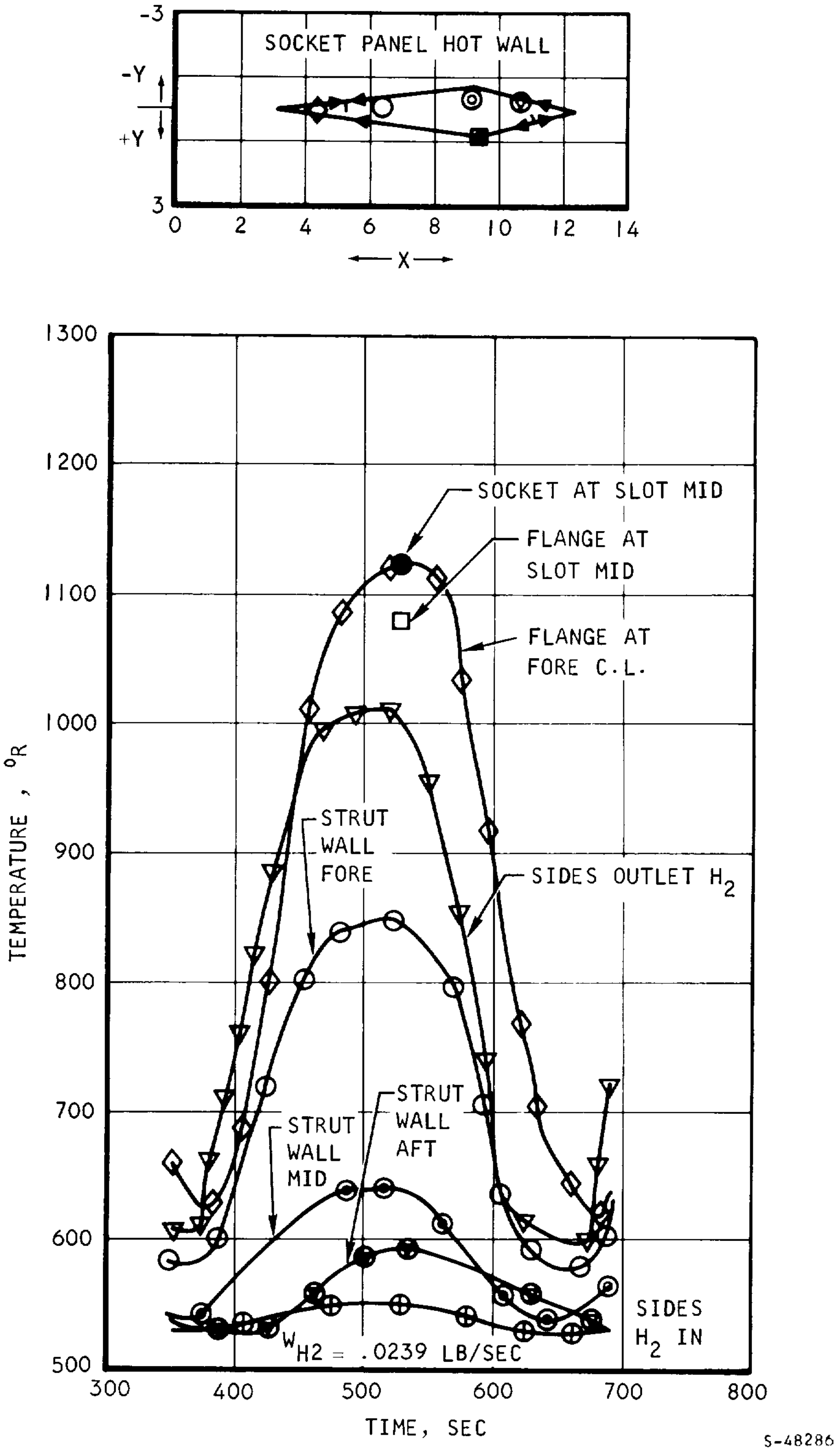

Figure 8.2-15 Strut SN 6, Cycle 9 Strut Temperatures

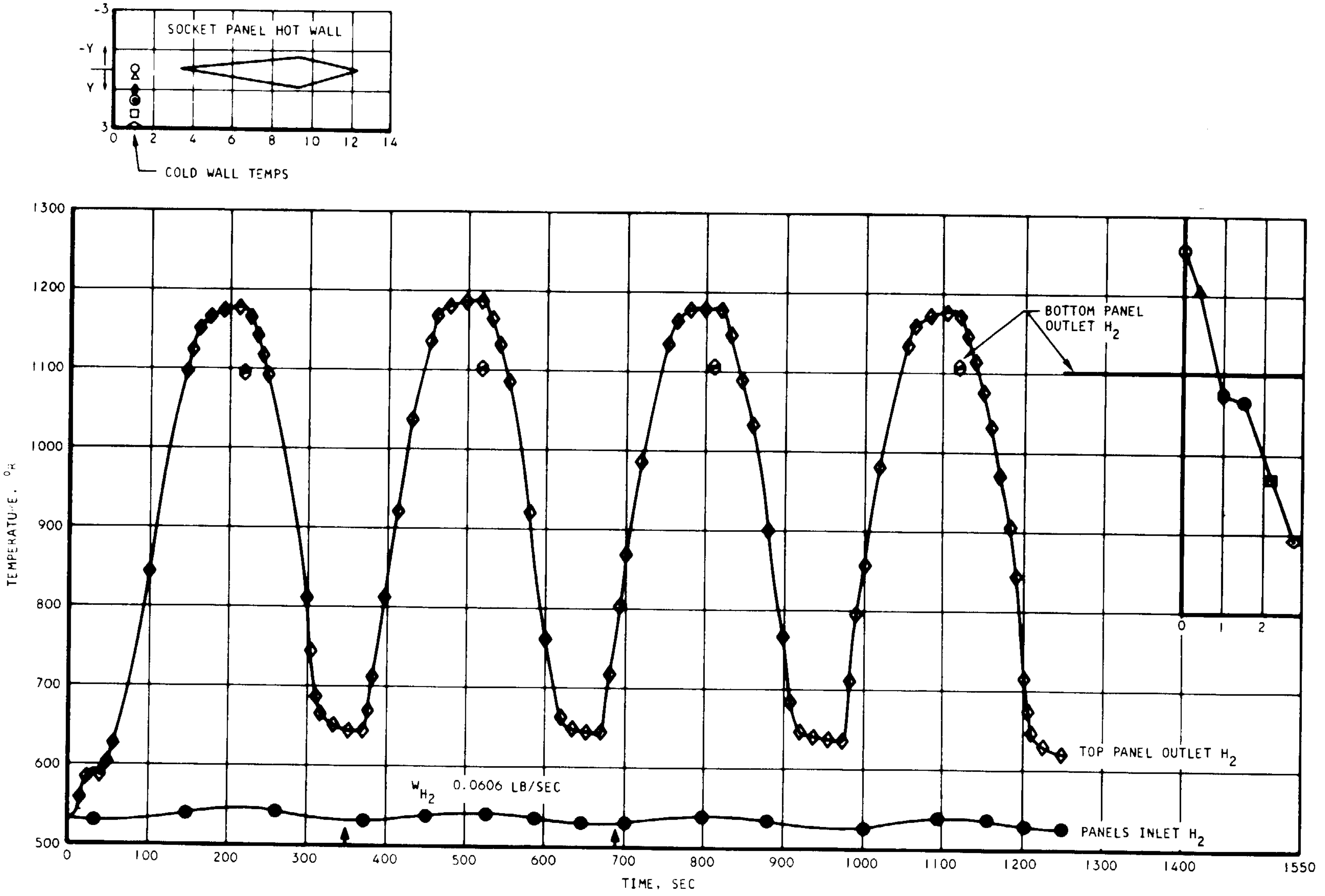

Figure 8.2-16 Strut SN 6, Cycles 8 Through 11 Hydrogen Temperatures

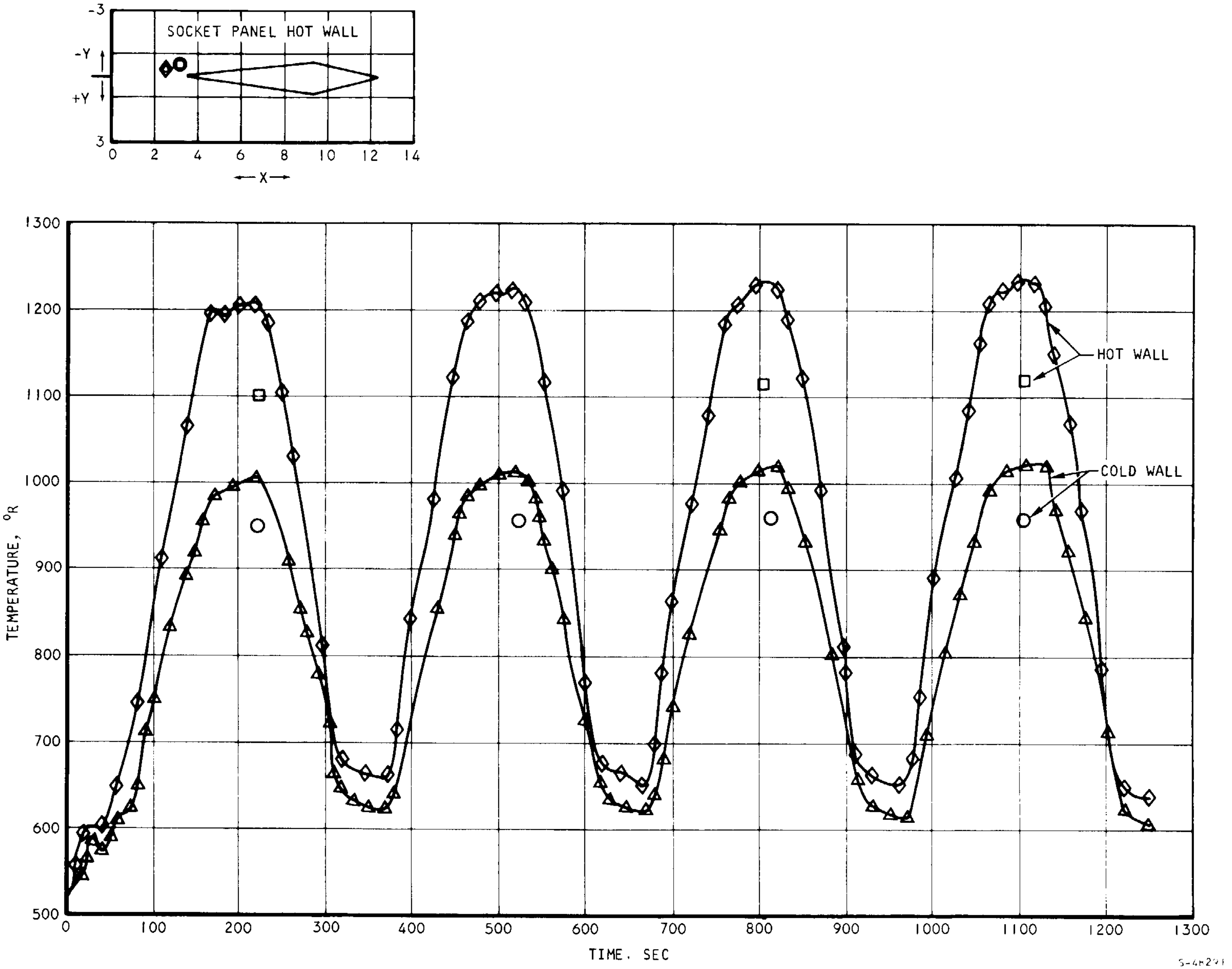

Figure 8.2-17 Strut SN 6, Cycles 8 Through 11 Panel Wall Temperatures

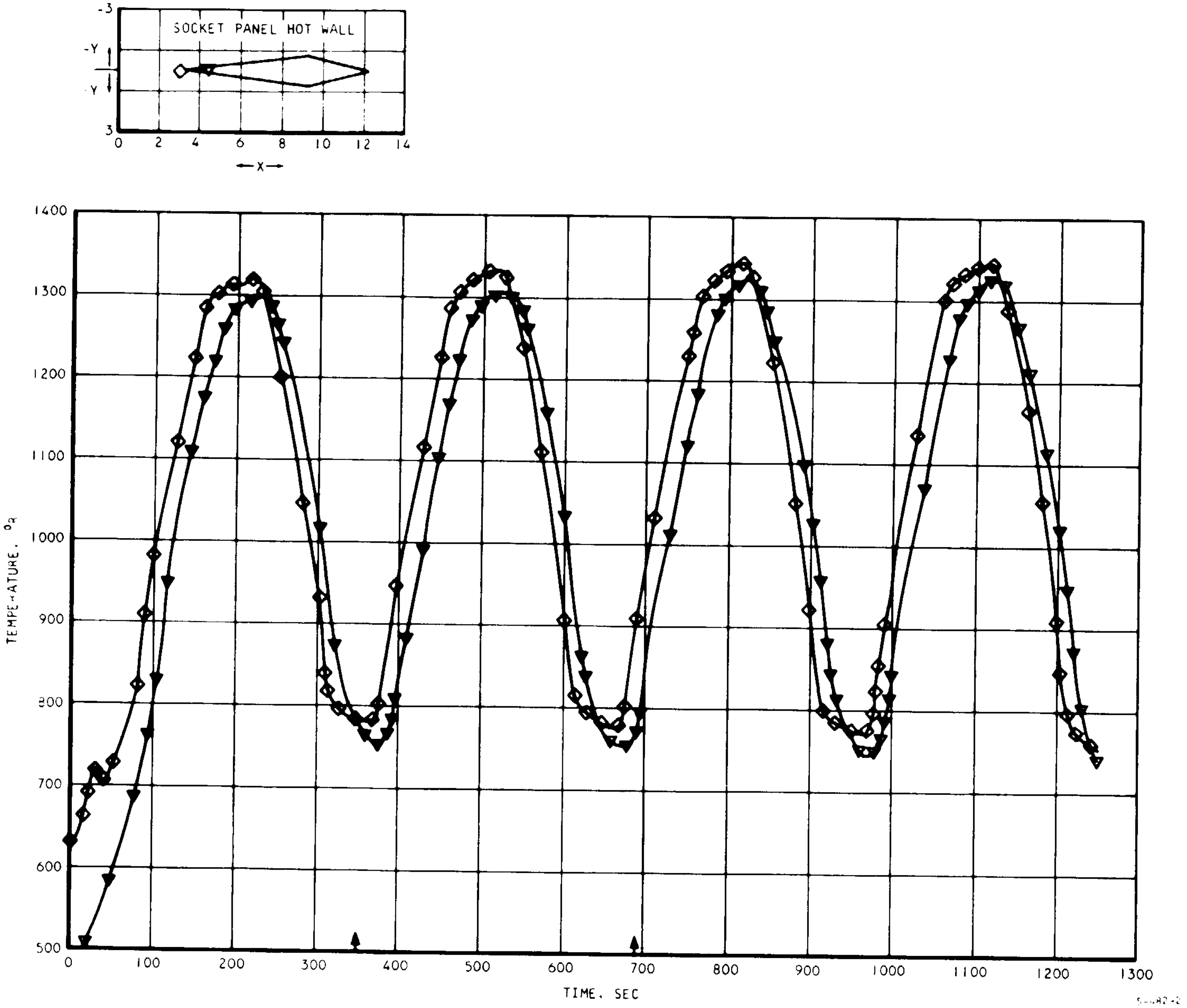

Figure 8.2-18 Strut SN 6, Cycles 8 Through 11 Panel Wall and Strut Socket Temperatures

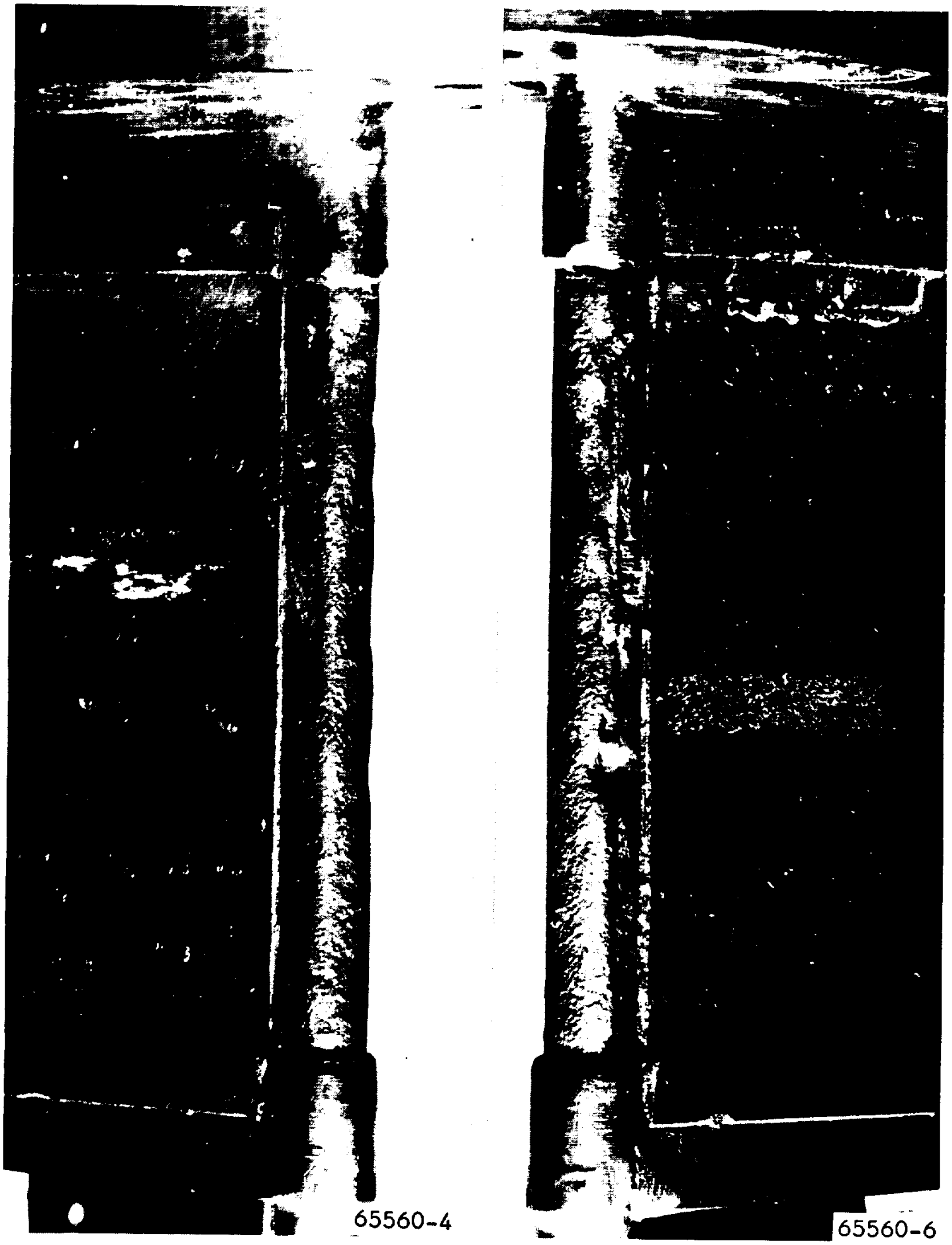
65560-4
65560-6
F-10367

Figure 8.2-19 Strut SN 6 Leading Edge After Cycle 11

$$h\ (\text{FAY-RIDDELL}) = \frac{0.56}{(Pr_w)^{.6}}\left(\frac{\rho_w \mu_w}{\rho_2 \mu_2}\right)^{0.1}\left(\frac{2\rho_2 \mu_2}{D}\sqrt{\frac{2q_c\left(P_{T2} - P_\infty\right)}{\rho_{T2}}}\right)^{0.5}\left(\frac{H_T - H_W}{T_T - T_W}\right)$$

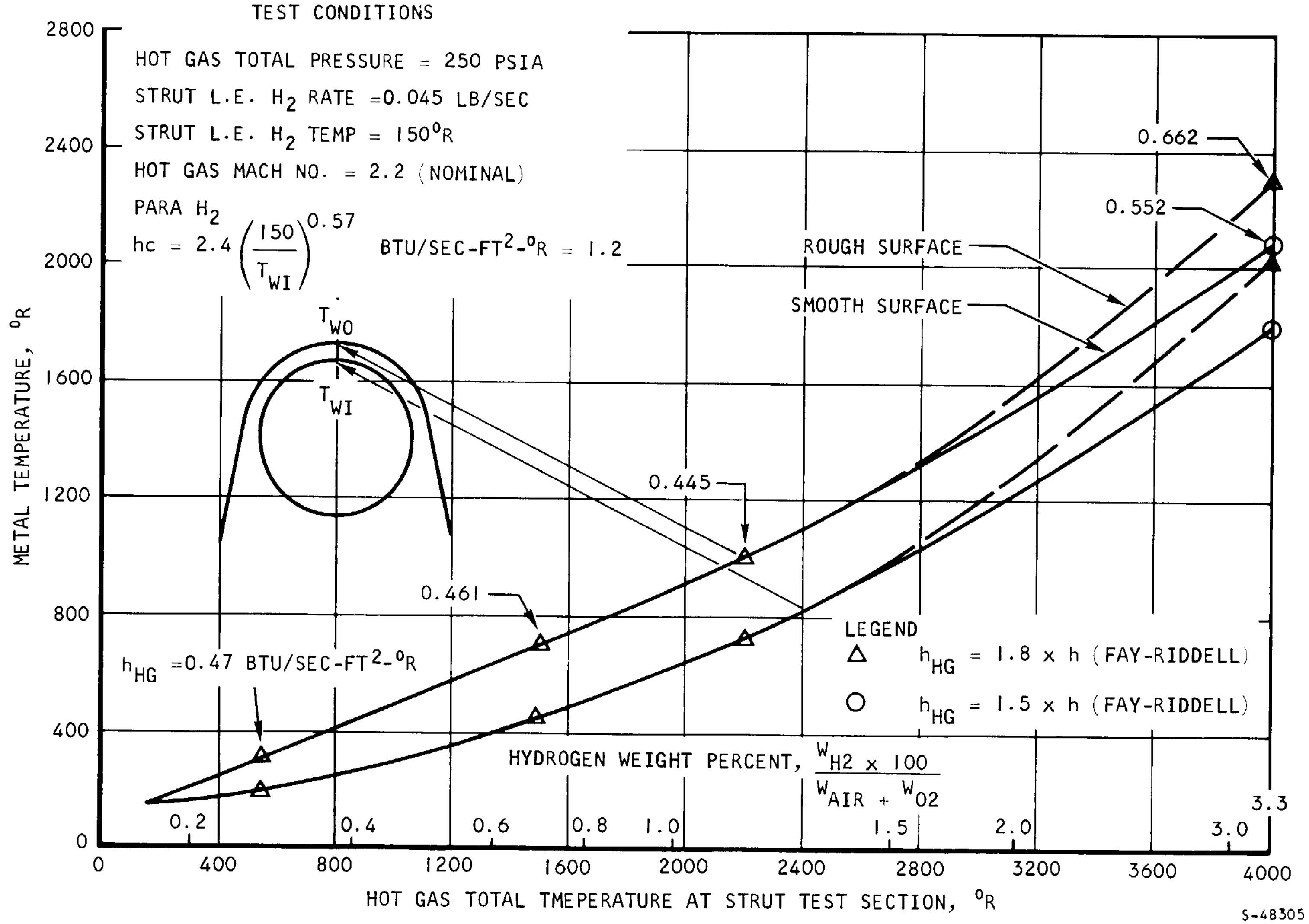

Figure 8.2-20 Strut Leading Edge Temperatures During Thermal Cycling

on the multiplier is established at a temperature somewhat below the Hastelloy X melting temperature of about 2760°R, or about 500°R above the maximum estimated temperature. The coolant heat transfer coefficients are minimum and the temperatures are maximum on Figure 8.2-20 because they were evaluated adjacent to the lower panel nearest the leading edge outlet where the thermal l/D is approximately 10. The heat transfer coefficient for fully developed flow was multiplied by 1.2 to account for an l/D of 10.

The leak in the hot wall of the strut support panel at the left of Figure 8.2-21 is shown in detail in Figure 8.2-22. The leak is adjacent to the strut leading edge because of local intense-heating and inadequate coolant heat transfer coefficient. This panel had inlet and outlet manifold flow distribution holes sized at the fin entrance and exit, in an attempt to provide adequate hydrogen in the strut cutout shadow, forward of the strut leading edge. Figure 8.2-12 shows the cold wall temperature across the half-width of the right hand panel in Figure 8.2-21. The high temperature in line with the strut indicates the low hydrogen flow in this region. The flow distribution design described in Reference 5 for the inner and outer shells will be used in the next cycling series and is expected to provide adequate cooling in the failed area.

8.2.3 Conclusions

Strut leading edge performance analysis indicates that

(a) The stagnation line heat flux increases 75 percent to 260 percent (K = 1.75 to 3.60) over that predicted by the Fay-Riddell equation. The cause for this increase is apparently due to the turbulence present in the approaching stream. It is characteristic of the specific wind tunnel installation. The extent of the increases in the HRE operating environment would require specific data for that environment, including simulation of the supersonic combustion process.

(b) The K-value appears to increase with the unit Reynolds number and also is affected in a smaller degree by the wall-enthalpy-to-recovery-enthalpy ratio.

(c) The boundary layer flow appears to be laminar, however, no conclusive evidence is found to prove that boundary layer transition around the leading edge never occurred.

8.2.4 Status

Thermal cycling of the SN 6 strut assembly is scheduled to resume in March. Doublers will be brazed to the top and bottom of the strut assembly to reduce the gap between the strut assembly and the support panels. One new support panel, with the coolant flow distribution channels next to the header, will be installed prior to the resumption of thermal cycle testing. This panel will replace the one that was damaged in test.

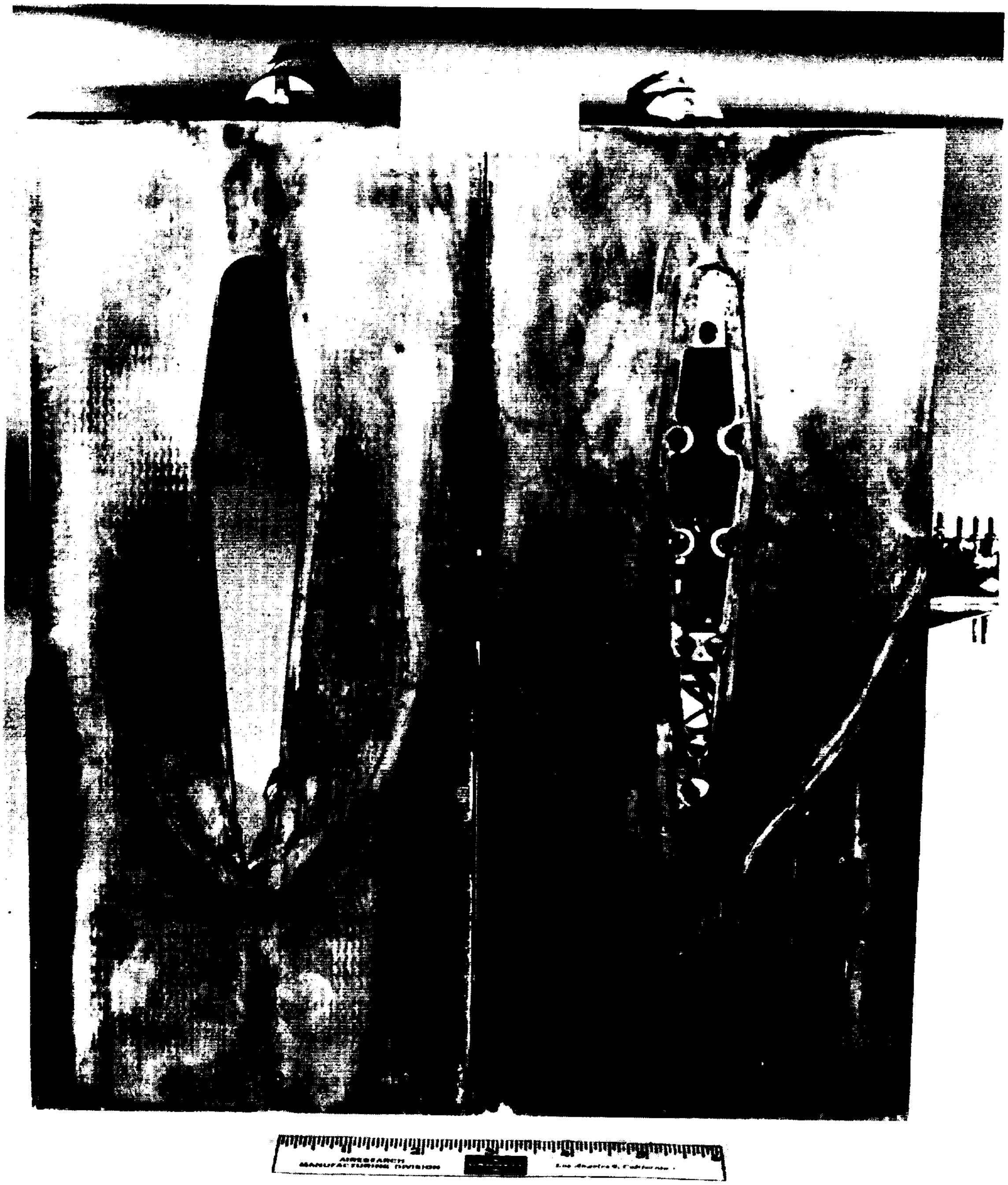

65560-1

Figure 8.2-21 Strut Support Panels (-4) After Cycle II

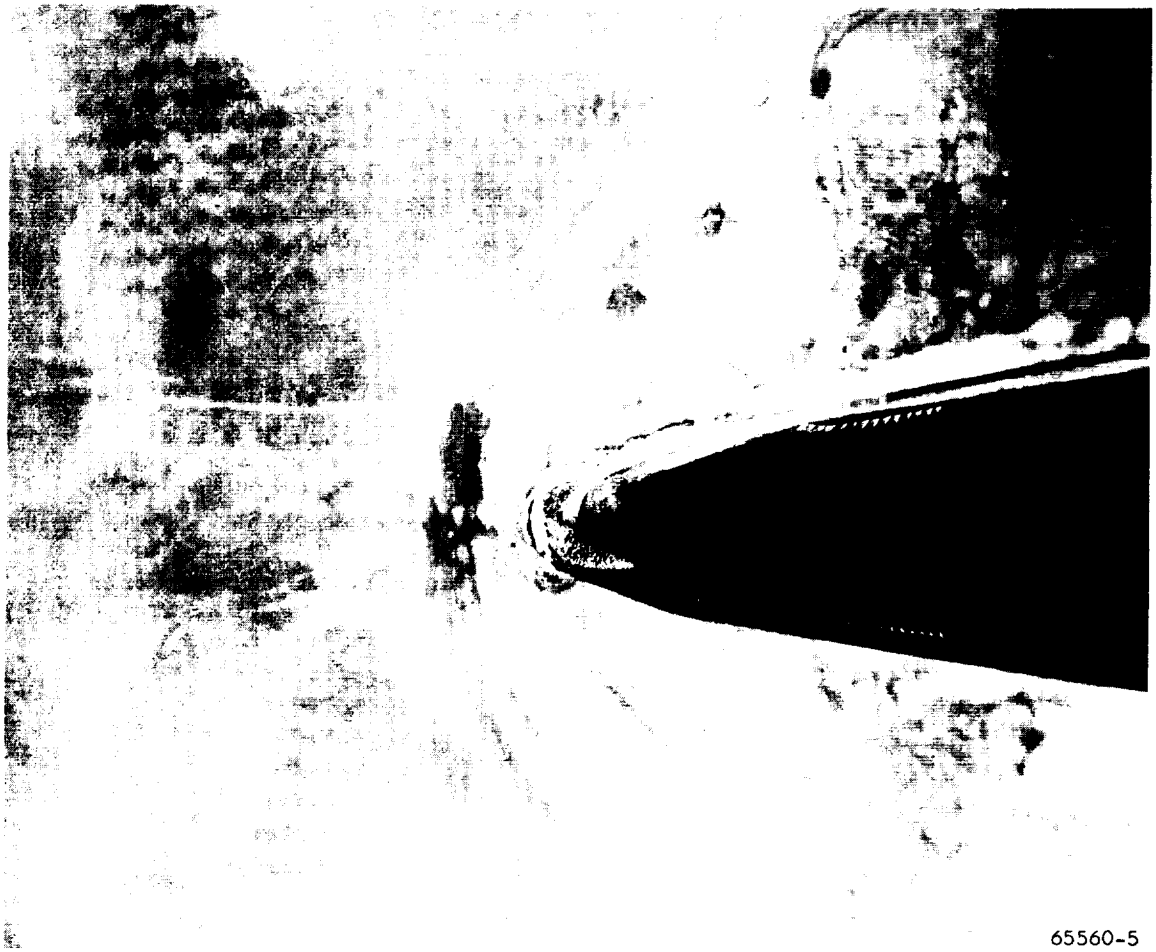

Figure 8.2-22 Strut Support Panel Failure

8.3 INLET SPIKE ACTUATOR AND CONTROL SYSTEM (ISACS)

Both prototype units PN 981190-2-1, SN 1, and PN 981190-1-1, SN 2, have been assembled and partially tested.

The first unit tested was PN 981190-2-1. Data was taken on (1) positioning accuracy, (2) response to load profiles for axial and normal loads, and (3) lateral load deflections. During load profile tests, prior to the planned endurance tests at 160°F, a failure occurred. The failure occurred when an inadvertent tensile load was applied to the unit, causing failure of the MS 21295-92 screws that attach the actuator to the housing. Corrective action consisted of replacing the screws with 17-4 PH screws and a 5/8 in. threaded stud to increase the load carrying capacity by a factor of six. This will eliminate a recurrence of the failure.

The PN 981190-1-1 was also modified to incorporate the 17-4 PH screws, which will double the load-carrying capacity. This unit was assembled and installed in the test assembly for functional acceptance testing. Data was obtained on (1) positioning accuracy, and (2) response to load profiles.

In addition to the above performance tests, both units were functionally tested to determine (1) ability to withstand a locking load of 8200 lb, (2) positioning rate (retracting and extending) (3) ability to unlock at "no-load", and loaded to 8200 lb, and (4) ability to overcome the friction level of the journal bearing preload.

8.3.1 Test Results

Data on positioning accuracy and the functional tests on PN 981190-2-1 taken prior to failure are included in this report. Testing on PN 981190-2-1 has been delayed until the damaged hardware has been reworked and the unit reassembled. Data has also been included on PN 981190-1-1 positioning accuracy functional tests and load profiles.

8.3.1.1 Load Profiles for PN 981190-1-1

The preprogrammed functions on the analog computer have been modified since the tests were performed on the 981190-2-1 unit in order to obtain better correlation with the design aerodynamic loads. The results of the load profile tests are shown in Figures 8.3.1 and 8.3.2. Figure 8.3-1a depicts the axial loads during retracting, showing good correlation with the design aerodynamic loads. Variations from the desired value are attributed to inertia effects within the system. Figure 8.3-1b shows a typical inlet unstart sequence. The axial loads exceed the aerodynamic load initially, then show reasonable correlation. This is also the case with Figure 8.3-1c. Figure 8.3-2a is operated in conjunction with 8.3-2d. Both the axial and the normal loads show a resonable correlation. Figure 8.3-2b is run in con unction with Figure 8.3-2c to demonstrate an inlet unstart sequence. The normal loads, Figure 8.3-2c, are the most significant and show very good correlation. The axial loads, Figure 8.3-2b, do not reflect the programmed inlet start-unstart sequence, but the load change is not

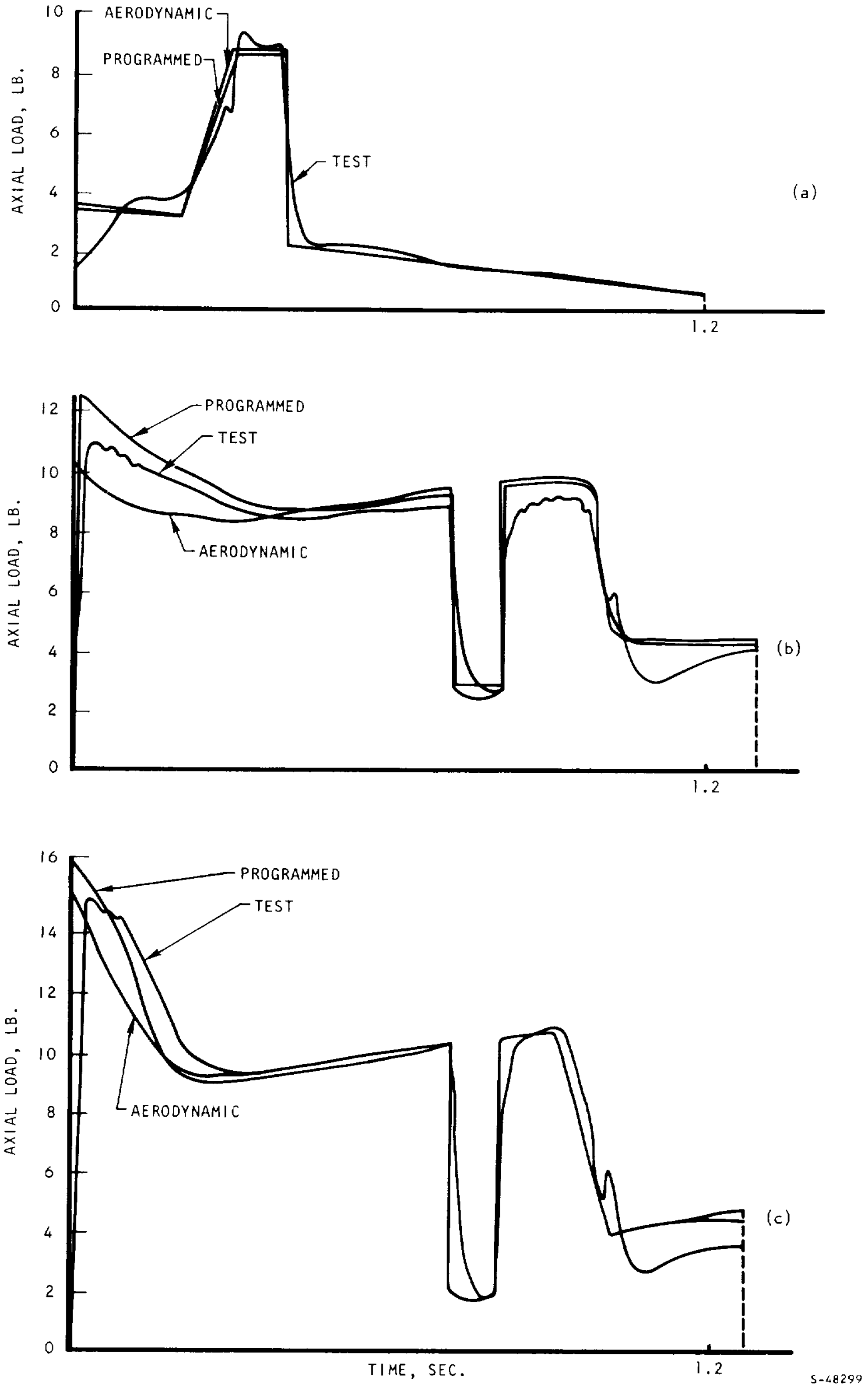

Figure 8.3-1 Load Profiles for PN 981190-1-1

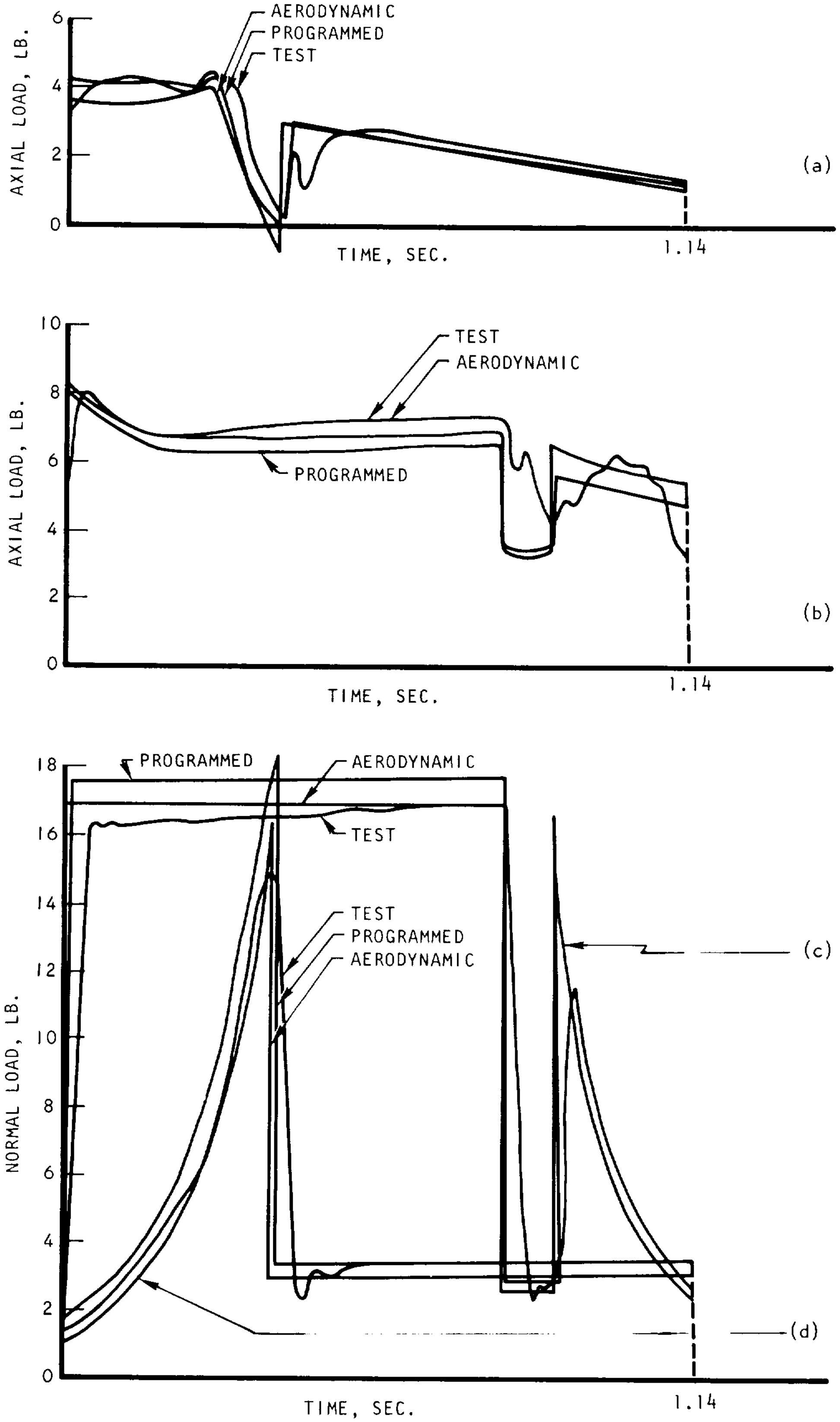

S-48298

Figure 8.3-2 Load Profiles For PN 981190-1-1

critical. In general, all the load profiles run on PN 981190-1-1 appear to acceptably demonstrate the capability of the ISACS to position and control loads applied at rapid rates.

8.3.1.2 Positioning Accuracy of PN 981190-1-1 and PN 981190-2-1

The data for the positioning accuracy for both units is summarized in Figure 8.3-3 for "no-load" and a 10,000 lb load. The displacement uncertainties, which are essentially the hysteresis effects, are shown as a function of the actuator displacement. The actuator displacement was determined by using precision dial indicators, and command positioning the actuator at intervals from two in. of retracted stroke to fully-retracted, and from fully-retracted to two in. of retraction. The plotted data is the difference between measurements during retractions and extension.

The displacemnt variation as a function of 10,000 lb load is shown in Figure 8.3-4. This indicates the maximum variation that can occur for a load change of 10,000 lb, and includes the uncertainties in Figure 8.3-3. Figure 8.3-4 is derived by plotting the maximum differences in positioning errors at given positions, considering both "no-load" and 10,000 lb load cases, and extension and retraction strokes. The positioning uncertainty was found to be well within the acceptable limit for the Mach 8 condition of ±0.058 in. The reason for the good positioning accuracy is largely attributable to the electronic integrator on the input command logic circuit, which tends to reduce the steady-state error value to null.

8.3.1.3 Functional Tests on PN 981190-1-1 and PN 981190-2-1

The results of the functional tests are summarized in Figure 8.3-5 and Table 8.3-1. The positioning rates in Figure 8.3-5 were obtained for "no-load" conditions. The pressure required for extending is less than half that required during retraction. This reflects the unbalanced piston design that is used. Also, the maximum pressure for retraction at 5 in./sec is less than half that available (1500 psi vs 3000 psi), leaving ample margin. Friction forces could not be obtained from this data, since there was no way of instrumenting the pressures on both sides of the actuator during stroking. Table 8.3-1 shows the static loads vary somewhat between units.

8.3.2 Data Evaluation

Testing on both units is incomplete, but comparative data has been taken on (1) load profiles, (2) positioning accuracy, and (3) functional performance.

8.3.2.1 Evaluation of PN 981190-2-1

Load profile data was submitted in the previous report (Reference 8), Figures 8.3-1 and 8.3-2. These profiles were acceptable, but refinements have been incorporated in the test electronics to give the results shown in Figures 8.3-1a, b, and c, which achieve better correlation with aerodynamic loads.

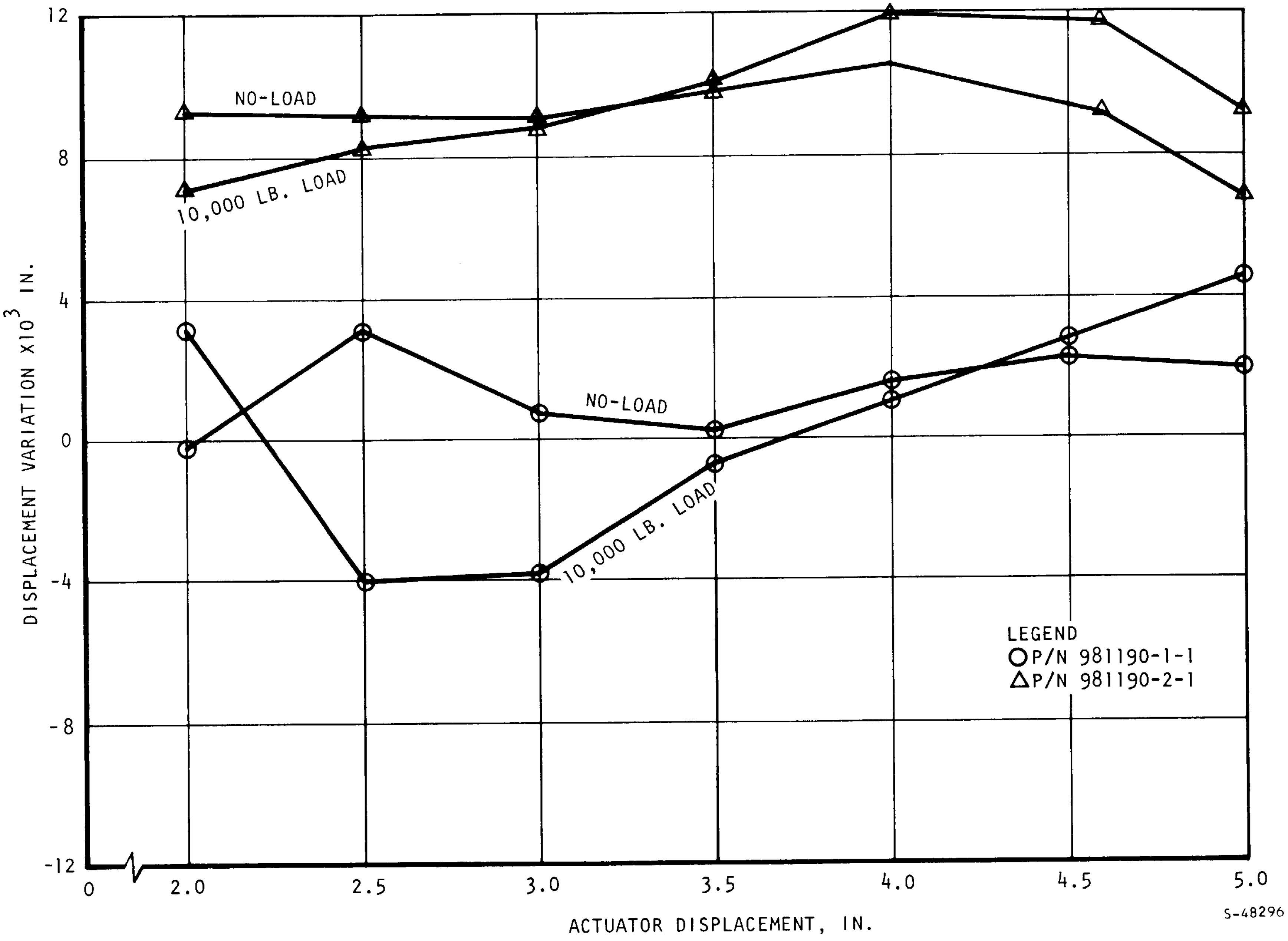

Figure 8.3.3 ISACS Positioning Accuracy

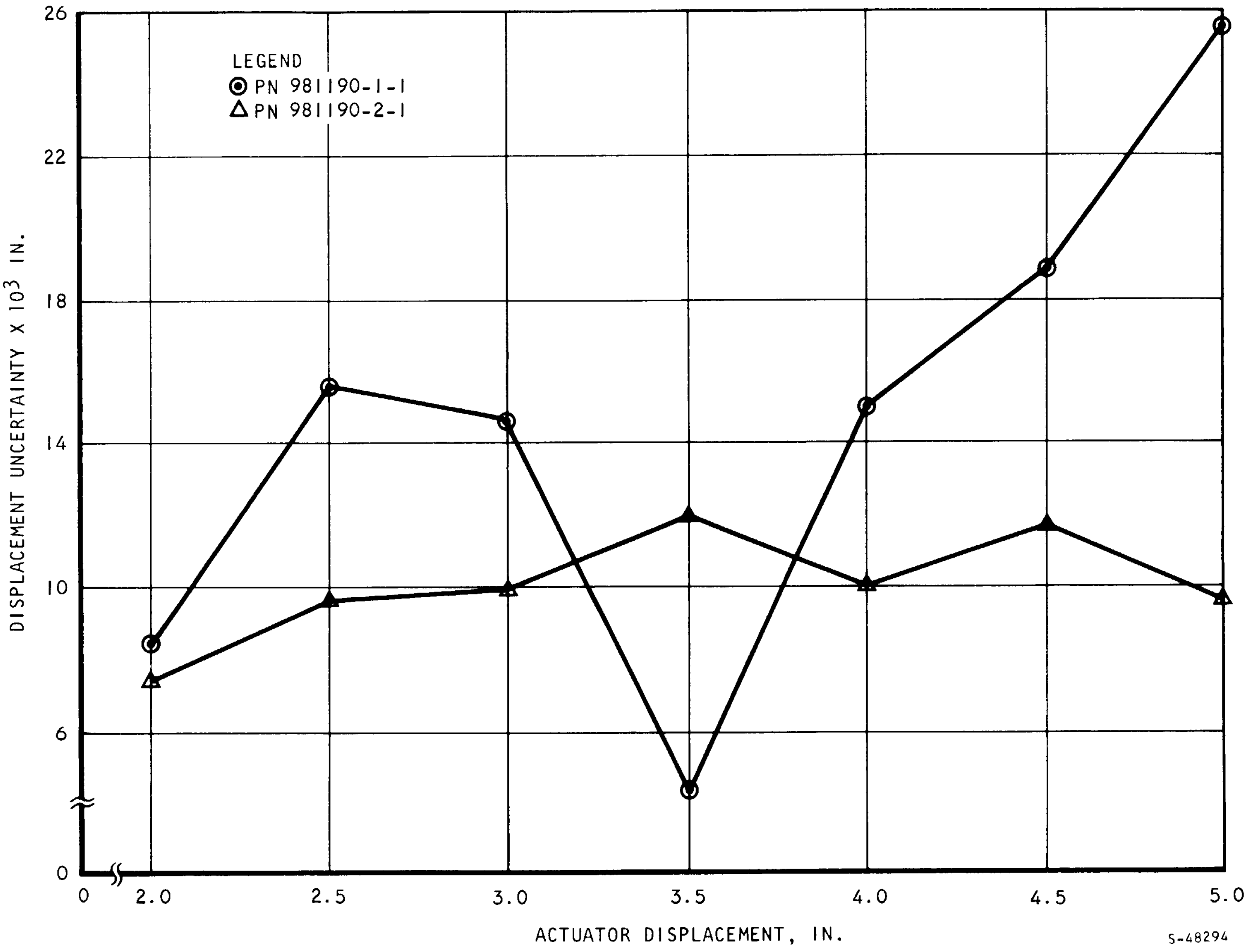

Figure 8.3-4 ISACS Displacement Variation

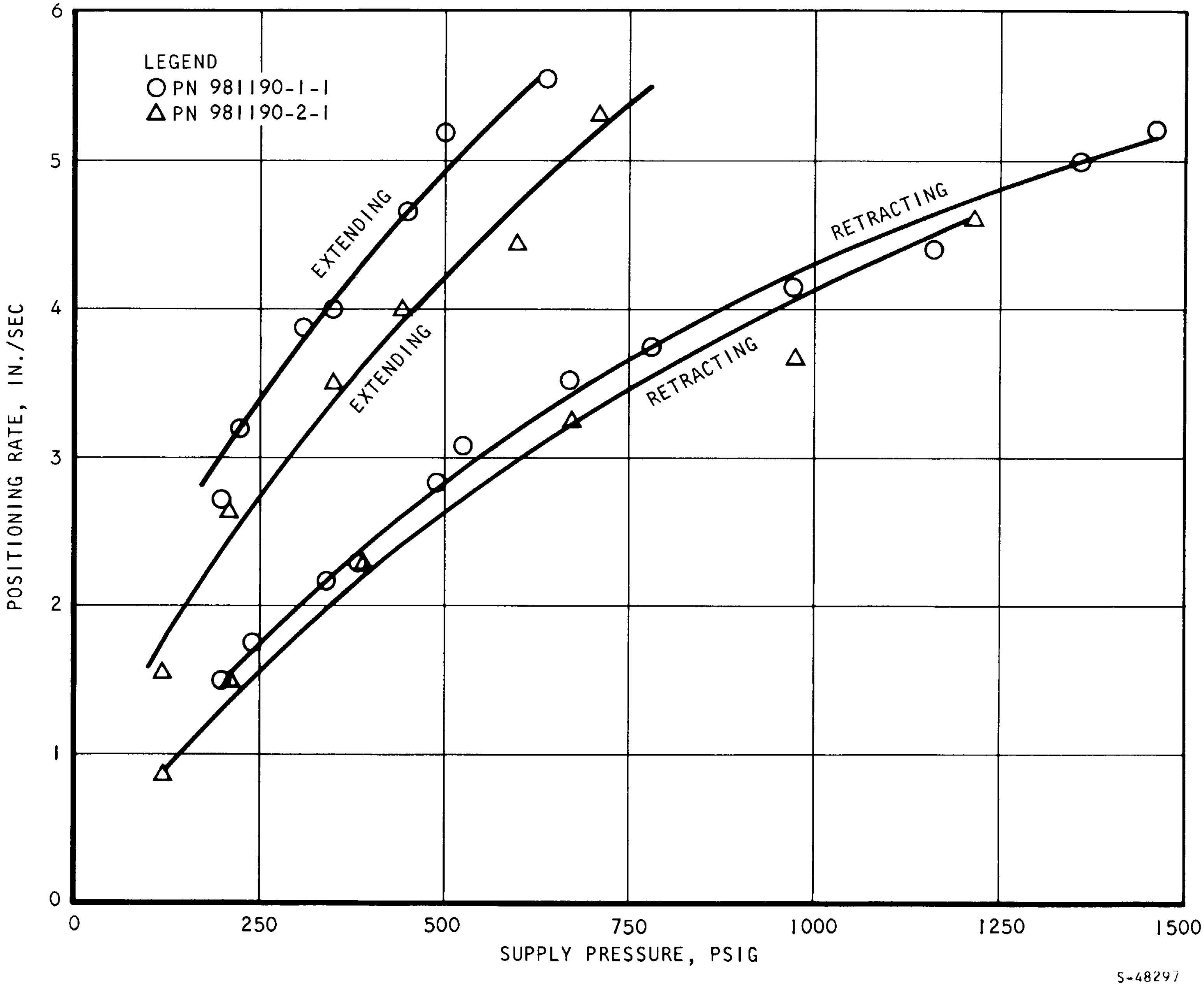

Figure 8.3-5 ISACS Positioning Rate vs Supply Pressure

TABLE 8.3-1

ACTUATOR LOADS

Unit	Friction Level of Journal Bearing Preload (lb) Avg.	Actuator Unlocking Pressure	
		Unloaded, psi	Loaded to 8200 lb, psi
981190-1-1	277	100	Not Recorded
981190-2-1	245	108	1375

A dynamic response capability to step load changes of the test assembly and unit, of 16,000 lb in less than 40 μsec, was obtained. Load profile data using the revised inputs will be forthcoming after reassembly and retest of the unit.

Positioning accuracy appears to be better for this unit than the 981190-1-1. Further testing is required to evaluate the effects of operation at 160°F and to determine the combined effects of temperature and load on positioning accuracy. The functional tests indicate an acceptable unit.

8.3.2.2 Evaluation of PN 981190-1-1

The testing on this unit was to demonstrate functional acceptance. Test results indicated that the unit was acceptable on all tests performed and comparable to the PN 981190-2-1.

8.3.3 Conclusions

Both units tested have demonstrated acceptable positioning accuracy, load profile transients, and functional characteristics. The results of the lateral deflection tests on PN 981190-2-1 indicate structural characteristics close to those predicted by analysis. The primary discrepancy was the increased structural compliance of the journal bearings. This indicates a higher preload is desirable to reduce lateral deflection during normal loads.

In general, the dynamic capabilities of the unit to meet the load profiles have been better than expected. Even with the rapidly changing aerodynamic loads, i.e., less than 60 μsec, the unit was able to change from 0 to 16,000 lb in about 40 μsec, which appears to be acceptable.

8.3.4 Status

After teardown of PN 981190-2-1 a bearing failure was noted. The failure was attributed to the poor surface finish on the mating structural housing. The second unit, PN 981190-1-1, was disassembled and inspected for comparison. Inspection of the bearings indicated no wear that was detectable on either bearing. In addition, the surface finish of the housing was checked and found to be within tolerance. This unit is in the process of being reassembled and installed in the test fixture for continued testing to determine the frequency response characteristics. PN 981190-2-1 has been completely disassembled, including the hydraulic actuator assembly. No further signs of excessive wear or damage were observed, and it is now in the process of being reassembled. Upon receipt of replacement bearings, and upon reassembly, the unit will be retested to evaluate the positioning accuracy, load profiles, and endurance at 160°F.

8.4 COOLED-SURFACE PERFORMANCE TEST

The purpose of this testing is to determine the friction factors and the heat transfer coefficients, as a function of Reynolds number, of two fin configurations used in the regeneratively cooled shells.

The test specimen for each fin design is a cross-flow heat exchanger with a core composed of two outer layers of the same fin structure and one center fin layer. The outer fin layers have the fin structure being evaluated for HRE performance (also see Section 7.8).

For the heat transfer performance evaluation, air at up to 600°F flows through the outer fin layers, and water at ambient temperature flows through the center fin layer. The temperature differences across the air and water sides of the fin cores and the flow rates are measured. Temperatures are measured using chromel/alumel thermocouples; airflow is measured with a sharp edged orifice, and water flow, with a turbine type flowmeter. Data is recorded over an airflow range of 0.3-15 lb/min., with the water flow held constant at about 85 lb/min. The friction factor for the fin structure is determined from pressure-drop measurements at isothermal conditions and during heat transfer tests.

Heat balance checks are run at reduced water flow rates (6 lb/min.) and at selected airflow rates. The resulting water temperature differences are sufficienty large (10° - 50°F) to minimize inherent instrumentation errors and permit meaningful heat-balance calculations. Actual performance data is run at high water flow rates to minimize cross-flow effects and uncertainties in water-side performance predictions. Water temperature differences are about 2°F and heat transfer coefficient ratios, water-side to air-side range from 4 to 10.

A schematic of the test arrangement is shown in Figure 8.4-1 while photographs of the laboratory test setup are shown in Figures 8.4-2 and 8.4-3.

During the reporting period, testing of the unit having 28 fins per in. has been started.

8.5 INTERNAL DOUBLER PANELS CREEP RUPTURE TESTS

Three flat panels with internal doubler strips were subjected to creep rupture tests to obtain basic data on the fin-strength performance. The decision to utilize this configuration in the fin-gap of the outer shell, was based primarily on manufacturing considerations; i.e., the relative ease of using an OD as compared to an ID doubler. A well defined fin gap of 0.050 to 0.060 in. occurs at this station. The doubler serves the function of reinforcing the skin thickness at the unsupported span and thereby preventing local hot-surface buckling due to the large operating temperature differences. A second important function of the doubler is the distribution of the added pressure load due to the fin-gap over a sufficient distance from the gap to effectively eliminate the edge-concentration effect.

The internal doubler will prevent thermal buckling of the hot skin. Test data was considered to be necessary to evaluate the effect of the load concentration due to the gap.

8.5.1 Test Specimens

The tests were carried out for three flat panels that consisted of a 0.015-in.-thick top face sheet, 0.062-in.-thick back sheet, and 20 per in. 0.006-in.-thick fins. These test specimens are identified as SK 51371 (SN 1 through 3) in the subsequent text. The panels, which were 2 in. wide by 3 in. total length, were constructed with two controlled fin gaps within the range 0.050 in. to 0.060 in. Doubler strips 0.050 in. wide by 0.020 in. thick were then brazed to the internal surface of the 0.015-in.-thick plate. In this way the test result would reflect the performance of the weaker fin (20 per in. as opposed to 28 per in.) and hence a conservative design edge-concentration could be established.

8.5.2 Test Data and Results

Each specimen was tested at 1600°F and at an initial pressure of 650 psi for a maximum of 10 hr. If a creep rupture did not occur, the pressure was raised to 800 psi, again for a maximum of 10 hr. or until rupture. The following results were obtained:

SN-1:	650 psi for 9.2 hr when rupture occurred
SN-2:	650 psi for 10 hr 800 psi for 0.5 hr when rupture occurred
SN-3:	650 psi for 10 hr 800 psi for 2.20 hr when rupture occurred

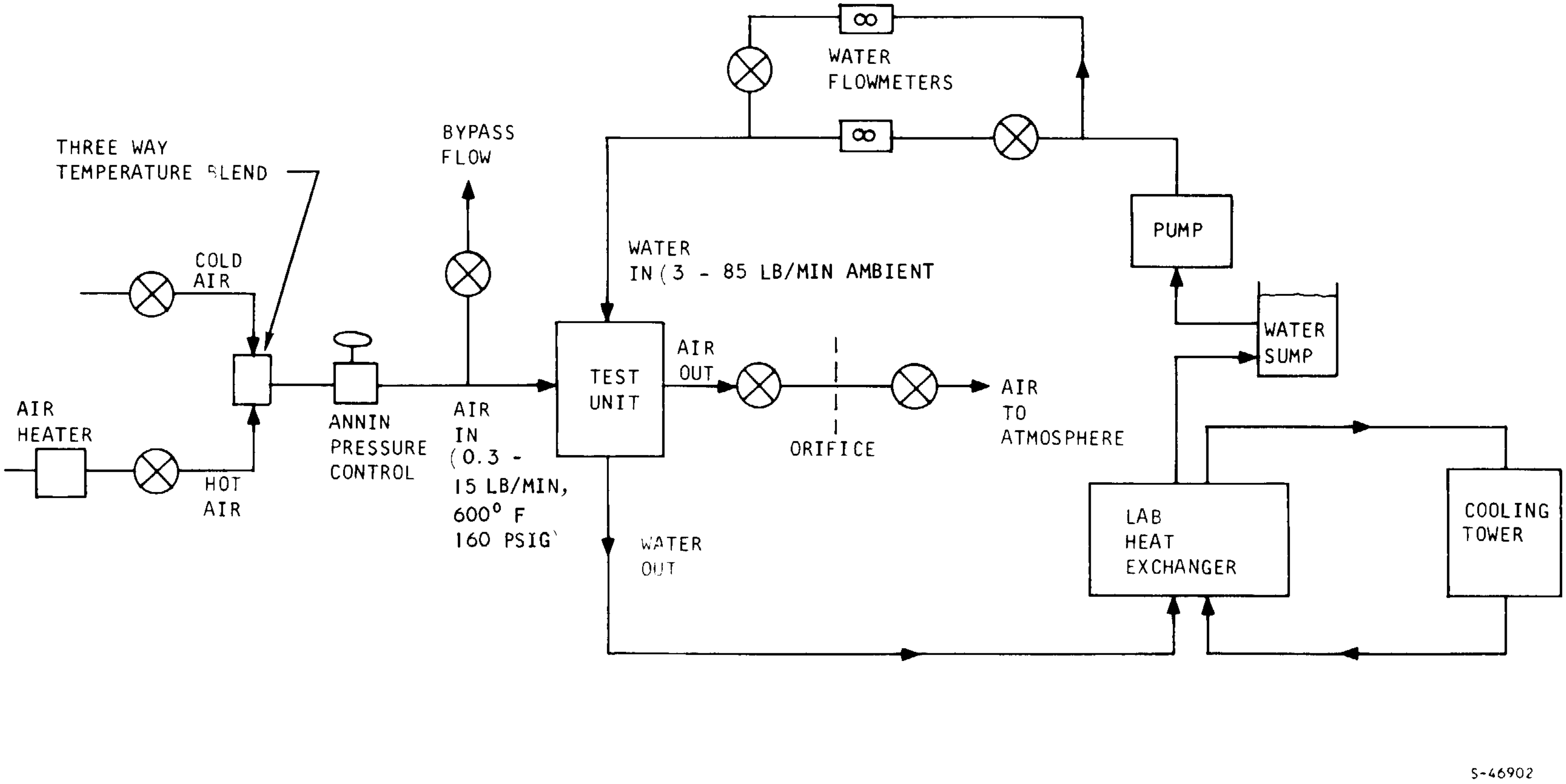
THREE WAY
TEMPERATURE BLEND
COLD
AIR
AIR
HEATER
HOT
AIR
ANNIN
PRESSURE
CONTROL
BYPASS
FLOW
AIR
IN
(0.3 -
15 LB/MIN,
600° F
160 PSIG
TEST
UNIT
WATER
IN (3 - 85 LB/MIN AMBIENT
AIR
OUT
ORIFICE
AIR
TO
ATMOSPHERE
WATER
OUT
WATER
FLOWMETERS
PUMP
WATER
SUMP
LAB
HEAT
EXCHANGER
COOLING
TOWER
S-46902

Figure 8.4-1 Schematic of Laboratory Test Setup for Cooled-Surface Performance Test Unit

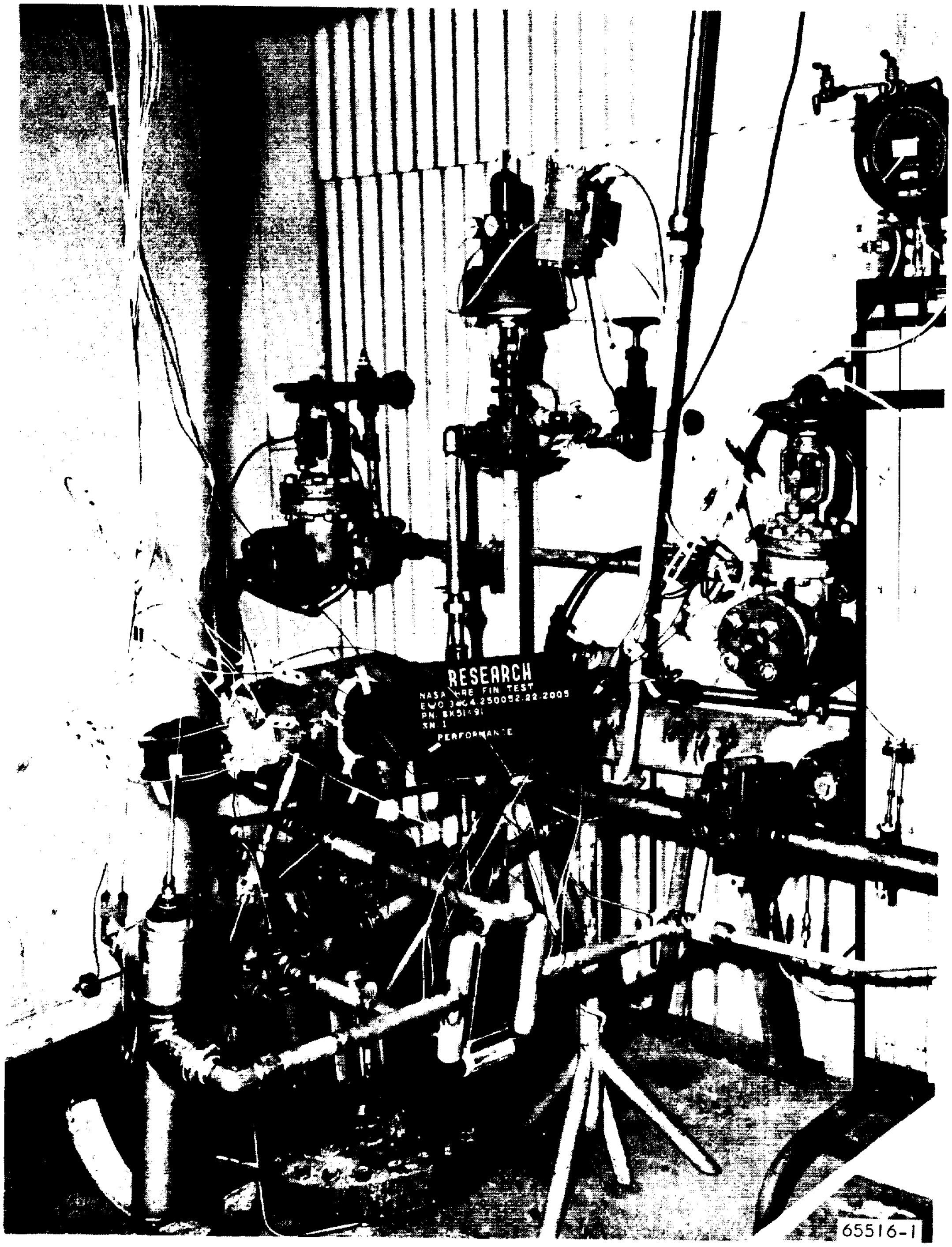
RESEARCH
NASA HRE FIN TEST
EWO 3464.250052.22.2005
PN. SK51491
SN. 1
PERFORMANCE
65516-1

Figure 8.4-2 Cooled-Surface Performance Test Setup

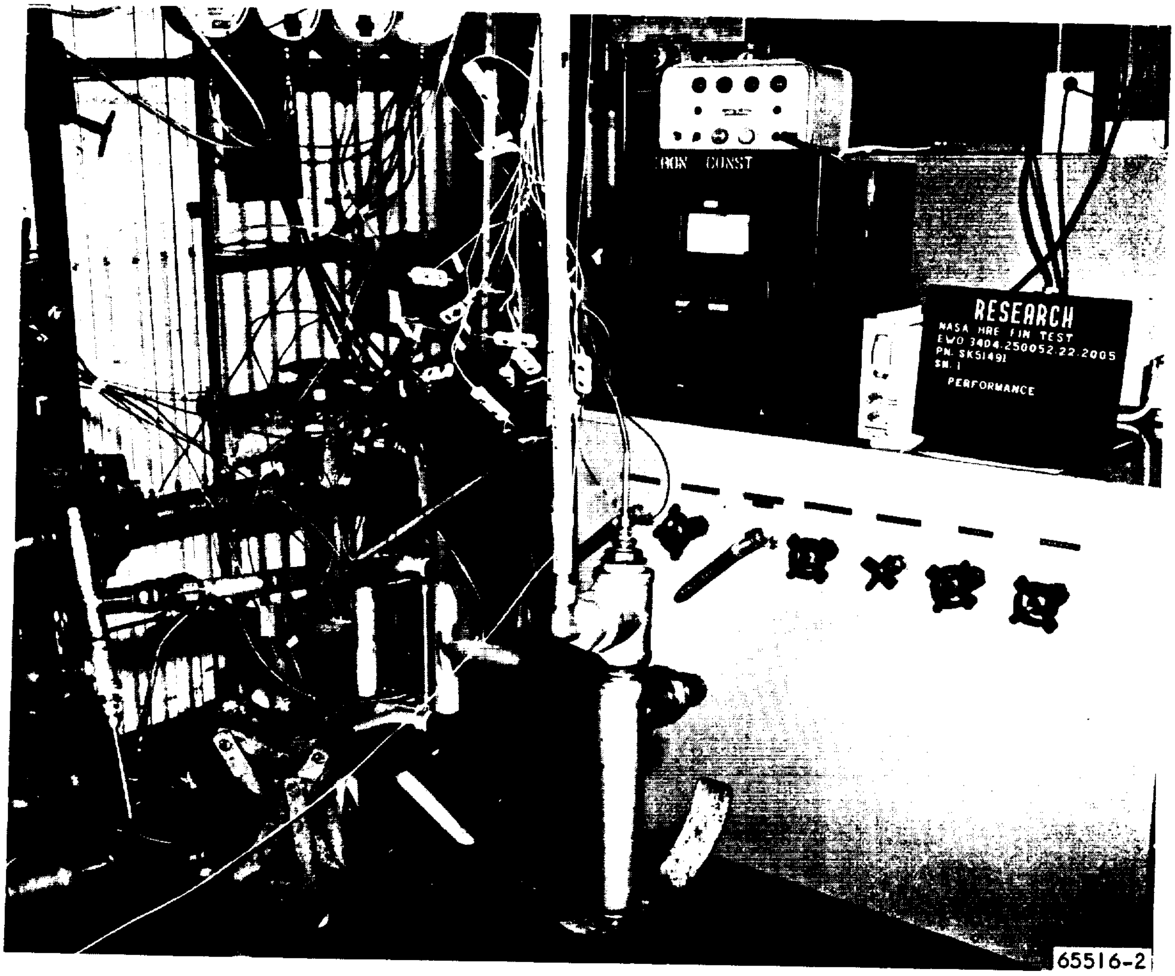
IRON CONST
RESEARCH
NASA HRE FIN TEST
EWO 3404.250052.22.2005
PN. SK51491
SN. 1
PERFORMANCE
65516-2

Figure 8.4-3 Cooled-Surface Performance Test Setup

8.5.3 Test Data Reduction

SN-1:

Hastelloy X stress to rupture in 9.2 hr at 1600°F = 14,600 psi

Step-multiplier for fins = S.M. = 7.333

Fin-strength efficiency factor = ν = 0. 423 (Sec. 8.1, Ref. 19)

Nominal fin stress = σ_{fin} = p x S.M. = 4760 psi

Effective fin strength efficiency factor for panel

$$\nu_{eff} = \frac{\sigma_{fin}}{14{,}600} = \frac{4760}{14{,}600} = 0.326$$

Defining the decrease in fin-strenght efficiency factor for the fins without the gap to that denoted above as the nominal fin-strength efficiency factor, the edge concentration effect, K_e, is

$$K_e = \frac{0.423}{0.326} = 1.300$$

SN-2: The multiple-step test requires a somewhat more involved calculation, and the method has already been explained in the data reduction of the strut rupture tests, Section 8.2, Reference 8. Essentially, this method consists of making a series of assumptions for the effective fin-strength efficiency factor, and then determining the value that would produce a total life fraction of unity for the test. This was accomplished by first assuming K_e = 1.0, which ammounts to using ν_{eff} = 0.423. This leads to the following results:

At 650 psi, $\sigma_1 = \frac{(650)(0.333)}{0.423} = 11{,}250$ psi

time to rupture at this stress = τ_1 = 35 hr

at 800 psi, $\tau_2 = \frac{(800)(7.333)}{0.423} = 13{,}850$ psi

time to rupture at this stress = τ_2 = 12.0 hr

the life fraction for the test is

$$\text{L.F.} = \frac{t_1}{\tau_1} + \frac{t_2}{\tau_2} = \frac{10}{35} + \frac{0.5}{12.0} = 0.286 + 0.041 = 0.327$$

Since this life fraction is less than unity, an effective fin-strength efficiency factor, 0.339 (for which $K_e = 1.25$), was tried

$$\sigma_1 = (11{,}250)\ (1.25) = 14{,}070 \text{ psi}; \ \tau_1 = 10.5 \text{ hr}$$

$$\sigma_2 = (13{,}850)\ (1.25) = 17{,}300 \text{ psi}; \ \tau_2 = 3.5 \text{ hr}$$

$$\text{L.F.} = \frac{10}{10.5} + \frac{0.5}{3.5} = 1.095$$

By plotting these two points on log-log paper, it was found that an edge concentration factor of 1.235 would lead to a unity life fraction. This was verified as follows:

$$\sigma_1 = (11{,}250)\ (1.235) = 13{,}900 \text{ psi}; \ \tau_1 = 11.6 \text{ hr}$$

$$\sigma_2 = (13{,}850)\ (1.235) = 17{,}050 \text{ psi}; \ \tau_1 = 3.7 \text{ hr}$$

$$\text{L.F.} = \frac{10}{11.6} + \frac{0.5}{3.7} = 0.865 + 0.135 = 1.000$$

SN-3: The same process as for SN-2 was employed. The value of K_e was found to be 1.15, as verified below:

$$\sigma_1 = (11{,}250)\ (1.15) = 12{,}930 \text{ psi}; \ \tau_1 = 16.5 \text{ hr}$$

$$\sigma_2 = (13{,}850)\ (1.15) = 15{,}920 \text{ psi}, \ \tau = 5.6 \text{ hr}$$

$$\text{L.F.} = \frac{10}{16.5} + \frac{2.2}{5.6} = 0.607 + 0.393 = 1.000$$

8.5.4 Conclusions

From the three test results it appears that an average edge concentration factor of 1.23 should be used for design purposes:

$$K_e = \frac{1.30 + 1.235 + 1.15}{3} = 1.23$$

By comparison with a beam-on-elastic-foundation analysis for this face sheet and fin configuration, it had been found that edge loads should persist from 0.050 to 0.100 in. from the loaded edge. Since the unsupported gap of 0.050/0.060 in. would share its load on two fin edges, each edge would support loading due to 0.025/0.030 in. of gap. An approximate edge-concentration factor of

$$K_e = \frac{0.100 + 0.030}{0.100} = 1.300$$

would be obtained, which indicates the reasonableness of the test results. It is concluded that the internal doubler is an effective device for controlling edge-concentration effects in this particular range.

9.0 FUTURE ACTION

The main efforts during the next reporting period will continue to be concentrated on fabrication of the full-scale structures R and D components.

9.1 STRUCTURAL ASSEMBLED MODEL DESIGN

Layout and detail design of the water-cooled cowl and pylon will be completed. All assembly drawings required for the SAM are also expected to be complete.

9.2 FULL-SCALE COMPONENTS

Fabrication of all full-scale components (inner shell, nozzle, leading edge, inlet spike, and outer shell) will continue. Completion of the final spike, inner shell, and nozzle assemblies is expected. Completion of the first two leading edge and outer shell assemblies is similarly anticipated. Flow distribution and pressure-drop tests of the existing components will be performed.

9.3 INLET SPIKE ACTUATION SYSTEM

The anticipated completion of testing on the two prototype inlet spike actuation systems during this reporting period was delayed by the occurrence of the journal bearing problem. Completion is now expected during the next reporting period. Frequency response tests will be run on the second prototype system completing the tests scheduled for it. The first prototype system will be reworked, and endurance tests performed, thereby completing all testing presently scheduled for the first prototype system.

9.4 MODEL TESTING

9.4.1 Leading Edge Straight Section

Thermal cycle tests of the leading edge straight sections are expected to be completed using the quartz-lamp, radiant-heating test setup.

9.4.2 Full-Scale Strut

A minimum of one entry, and possibly two, are planned for wind tunnel thermal cycle tests of the struts. The first entry will be with the strut on which testing was started during this reporting period. The second entry will be with a strut which has been modified to have a hard flame-sprayed plating on the leading edge, as well as a fin brazed into the leading edge passage of the strut. In addition, provisions will be made to control flow in the gap between the strut and the support panels, below what is possible with normal assembly tolerances. Hand finished, matched strips will be used around the edges of the strut to accomplish this.

9.4.3 Cooled-Surface Performance Tests

Testing of the two fin configurations planned for evaluation will be completed.

REFERENCES

1. Engineering Staff, Hypersonice Research Engine Project - Phase IIA, Structures and Cooling Development, Third Interim Technical Data Report, Data Item 55-7.03, AiResearch Report No. AP-67-2833, 4 December 1967, CONFIDENTIAL.

2. Smith, Howard E., "The Flow Field and Heat Transfer Downstream of a Rearward Facing Step in Supersonic Flow," Report No. ARL 67-0056, March 1967.

3. Fay, J. A., and F. R. Riddell, "Theory of Stagnation Point Heat Transfer in Dissociated Air," Journal of Aeronautical Sciences, Vol. 25, No. 2, February 1958.

4. Chupp, R. E., et al, "Evaluation of Internal Heat Transfer Coefficients for Impingement Cooled Turbine Airfoils," Paper No. 68-564, AIAA 4th Propulsion Joint Specialists Conference, Cleveland, Ohio, 1968.

5. Engineering Staff, Hypersonic Research Engine Project - Phase IIA, Structures and Cooling Development, Sixth Interim Technical Data Report, Data Item 55-7.06, AiResearch Report No. AP-68-4173, 31 August 1968, pp. 8-13.

6. Taylor, Maynard F., "Correlation of Local Heat Transfer Coefficients for Single Phase Turbulent Flow of Hydrogen in Tubes with Temperature to 23," TN D-4332, 1968, National Aeronautics and Space Administration, Cleveland, Ohio.

7. Engineering Staff, Hypersonic Research Engine Project - Phase IIA, Structures and Cooling Development, First Interim Technical Data Report, Data Item 55-7.01, AiResearch Report No. AP-67-2161, 3 May 1967.

8. Engineering Staff, Hypersonic Research Engine Project - Phase IIA, Structures and Cooling Development, Seventh Interim Technical Data Report, Data Item 55-7.07, AiResearch Report No. AP-68-4482, 27 November 1968.

9. Edney, Barry E., "Effects of Shock Impingement on Heat Transfer Around Blunt Bodies," AIAA Journal, Vol. 6, No. 1, January 1968, pp. 15-21.

10. Hiers, Robert S., and Wm. J. Loubsky, "Effects of Shock-Wave Impingement on the Heat Transfer of a Cylindrical Leading Edge," NASA TN D-3859.

11. Teterin, M. P., "Investigation of a Supersonic Gas Flow and Heat Transfer in the Region of an Incident Shock Wave on a Cylinder," NASA TT F-11795, July 1968.

12. Bushnell, Dennis M., "Effects of Shock Impingement and Other Factors on Leading Edge Heat Transfer," Conference on Hypersonic Aircraft Technology, Ames Research Center, Moffett Field, California, May 16-18, 1967, CONFIDENTIAL.

REFERENCES (Continued)

13. Engineering Staff, Hypersonic Research Engine Project - Phase IIA, Structures and Cooling Development, Second Interim Technical Data Report, Data Item 55-7.02, AiResearch Report No. AP-67-2537, 23 August 1967, CONFIDENTIAL.

14. Kestin, J., "The Effect of Freestream Turbulence on Heat Transfer Rates," Chapter I of Advances in Heat Transfer, Irvine, Thomas F. Jr., and James P. Hartnett, Academic Press 1966.

15. Wecks, Thomas, "Influence of Free-Stream Turbulence on Hypersonic Stagnation Zone Heating," AFFDL-TR-67-195, Air Force System Command, Wright-Patterson Air Force Base, Ohio.

16. Lees, L., "Laminar Heat Transfer Over Blunt-Nosed Bodies at Hypersonic Flight Speed," Jet Propulsion, April 1956.

17. Farmer, Otis A., "Tables of Para-Hydrogen Data in Engineering Units from 36° to 5000°R at Pressure to 5000 psia," Los Alamos Scientific Laboratory Report LA-3669, May 5, 1967.

18. Hendricks, Robert C., Robert W. Graham, Yih Y. Hsu, and Robert Friedman, "Experimental Heat Transfer Results for Cryogenic Hydrogen Flowing in Tubes at Subcritical and Supercritical Pressures to 800 psia," NASA TN D-3095, March 1966.

19. Engineering Staff, Hypersonic Research Engine Project - Phase IIA, Structures and Cooling Development, Fourth Interim Technical Data Report, Data Item No. 55-7.04, AiResearch Report No. AP-68-3250, 1 March 1968, CONFIDENTIAL.